

Photometric variability of massive young stellar objects. I.★

G. D. C. Teixeira^{1,2}, M.S.N. Kumar^{1,3}, L. Smith^{4,3}, P. W. Lucas³, C. Morris³, J. Borissova^{5,6}, M. J. P. F. G. Monteiro^{1,2}, A. Caratti o Garatti⁷, C. Contreras Peña⁸, D. Froebrich⁹, and J.F. Gameiro^{1,2}

¹ Instituto de Astrofísica e Ciências do Espaço, Universidade do Porto, CAUP, Rua das Estrelas, 4150-762 Porto, Portugal

² Departamento de Física e Astronomia, Faculdade de Ciências, Universidade do Porto, Rua do Campo Alegre 687, PT4169-007 Porto, Portugal

³ Centre for Astrophysics Research, University of Hertfordshire, Hatfield, AL10 AB, UK

⁴ Institute of Astronomy, University of Cambridge, Madingley Road, Cambridge, CB3 0HA, UK

⁵ Instituto de Física y Astronomía, Universidad de Valparaíso, Gran Bretaña 1111, Playa Ancha, Valparaíso, Chile

⁶ Millennium Institute of Astrophysics, Vicuña Mackenna 4860, 7820436 Macul, Santiago, Chile

⁷ Dublin Institute for Advanced Studies, Astronomy & Astrophysics Section, 31 Fitzwilliam Place, Dublin 2, Ireland

⁸ Department of Physics and Astronomy, University of Exeter, Stocker Road, Exeter, Devon EX4 4SB, UK

⁹ Centre for Astrophysics and Planetary Science, School of Physical Sciences, University of Kent, Canterbury, CT2 7NH, UK

September 14, 2018

ABSTRACT

The Vista Variables in the Via Lactea (VVV) survey has allowed for an unprecedented number of multi-epoch observations of the southern Galactic plane. In a recent paper, 13 massive young stellar objects (MYSOs) have already been identified within the highly variable ($\Delta K_s > 1$ mag) YSO sample of another published work. This study aims to understand the general nature of variability in MYSOs. Here we present the first systematic study of variability in a large sample of candidate MYSOs. We examined the data for variability of the putative driving sources of all known Spitzer extended green objects (EGOs) (270) and bright 24 μm sources coinciding with the peak of 870 μm detected ATLASGAL clumps (448), a total of 718 targets. Of these, 190 point sources (139 EGOS and 51 non-EGOs) displayed variability ($IQR > 0.05$, $\Delta K_s > 0.15$ mag). 111 and 79 light-curves were classified as periodic and aperiodic respectively. Light-curves have been sub-classified into eruptive, dipper, fader, short-term-variable and long-period-variable-YSO categories. Lomb-Scargle periodogram analysis of periodic light-curves was carried out. 1 - 870 μm spectral energy distributions of all the variable sources were fitted with YSO models to obtain the representative properties of the variable sources. 41% of the variable sources are represented by $> 4 M_\odot$ objects, and only 6% were modelled as $> 8 M_\odot$ objects. The highest-mass objects are mostly non-EGOs, and deeply embedded, as indicated by nearly twice the extinction when compared with EGO sources. By placing them on the HR diagram we show that most of the lower mass, EGO type objects are concentrated on the putative birth-line position, while the luminous non-EGO type objects group around the zero-age-main-sequence track. Some of the most luminous far infrared (FIR) sources in the massive clumps and infrared quiet driving sources of EGOS have been missed out by this study owing to an uniform sample selection method. A high rate of detectable variability in EGO targets (139 out of 153 searched) implies that near-infrared variability in MYSOs is closely linked to the accretion phenomenon and outflow activity.

Key words. techniques: photometric, stars: formation, stars: massive, stars: pre-main sequence, stars: protostars, stars: variables: general

1. Introduction

The paradigm of accretion in young stellar objects (YSO) has shifted from a model of constant mean accretion rate to that favouring short events of intense accretion (Vorobyov & Basu, 2006, 2015; Zhu et al., 2009). This shift is largely to address the issue of the ‘protostellar luminosity problem’ (Kenyon et al., 1990; Kenyon & Hartmann, 1995; Dunham et al., 2014). A variety of models including turbulent or competitive accretion, accretion regulated by core, disk, and feedback, are invoked to understand the deviation from the idealized case of isothermal sphere (Kenyon et al. (1990), McKee & Offner (2010), Myers (2010), Vorobyov & Basu (2008), Dunham & Vorobyov (2012), Dunham et al. (2014) and references therein). However, most of

these models share the variable accretion component, albeit differing at various mass regimes. The accumulated observational evidence appears to favour variable accretion instead of constant mean scenarios (Dunham et al., 2014). Photometric variability of YSOs can be related to their natal environment, accretion physics or a combination of both (Contreras Peña et al. (2017), Kesseli et al. (2016), Meyer et al. (2017) and references therein). Some of the variability can be caused by cold and hot spots formed on the surface of the YSO by infalling material from the disc. Dust clumps in the stellar medium surrounding the YSO can cause variable extinction of star-light as it passes along the observers line of sight (e.g. Herbst & Shevchenko (1999), Eiroa et al. (2002) among others).

The FUors (FU Orionis) and EXors (EX Lupi) examples of high amplitude photometric variability result from variable accretion. Respectively, they last from a few years to a few months. These objects are known to be low-mass YSOs, although similar counterparts in the higher mass range have been found (Kumar et al., 2016; Caratti o Garatti et al., 2017). Kumar et al. (2016)

Send offprint requests to: G. D. C. Teixeira;
email: gteixeira@astro.up.pt

* Tables 2, A.1, and A.2 are only available in electronic form at the CDS via anonymous ftp to cdsarc.u-strasbg.fr (130.79.125.5) or via <http://cdsweb.u-strasbg.fr/cgi-bin/qcat?J/A+A/>.

uses highly variable light curves (LCs) of massive young stellar objects (MYSOs) candidates from the Vista Variables in the Via Lactea (VVV) survey (Minniti et al., 2010), arguing that they were signposts of ongoing episodic accretion. Photometric and spectroscopic variability in a $20 M_{\odot}$ MYSO was used by Caratti o Garatti et al. (2017) to conclude that disk-mediated accretion bursts are a common mechanism across stellar masses. ALMA observations were used by Hunter et al. (2017) as evidence that sudden accretion is responsible for the growth of a massive protostar. These findings suggest that episodic accretion maybe a common mechanism in star formation, independent of mass. Computational models predict luminous flares in MYSOs, which are morphologically similar to FUors and EXors (Meyer et al., 2017).

The findings in Kumar et al. (2016) raise the question of the overall nature of variability in massive YSOs. In this paper, we attempt to examine the variability phenomena in known extended green objects (EGOs) (Cyanowski et al., 2008) and IR sources, deeply embedded in clumps identified by the APEX Telescope Large Area Survey of the Galaxy (ATLASGAL) (Schuller et al., 2009). They represent unbiased large samples of point-like massive young stellar candidates, therefore, allowing us to use the point source photometry to examine variability. We surmise that the RMS and UCHII regions represent an important MYSO sample, however, it requires larger aperture photometry of extended objects to examine variability, which we postpone to a different study.

Employing point source photometry requires that the targets are point like in MIPS, have associated high mass star forming signposts, and finally they are also point-like in the K_s band. The selection of such targets is described in Section 2. In Sect. 3 we describe the results obtained and discuss their implications in Sect. 4.

2. Target sample, data, and methods

Identification of point-like MYSO targets is based on the Spitzer GLIMPSE and MIPS surveys (Carey et al., 2009), the ATLASGAL survey (Schuller et al., 2009), and the VVV survey (Minniti et al., 2010). These different surveys are highly complementary, covering much of the same area but at different wavelengths (from $\sim 1.2 - 870 \mu\text{m}$). We searched for: a) driving sources of EGOs (Cyanowski et al., 2008; Chen et al., 2013a,b) and b) luminous MIPS $24 \mu\text{m}$ point sources embedded in ATLASGAL clumps. The two samples are expected to roughly represent two early evolutionary phases of massive stars; the EGOs, with an active phase of mass ejection, and non-EGOs which are likely yet to begin outflow activity.

2.1. MYSO sample

2.1.1. EGO sample

EGOs are objects with extended emission in the Spitzer $4.5 \mu\text{m}$ band (IRAC 2). This band is of particular significance since it contains both H_2 , and CO lines, which can be excited by shocks when outflows and jets interact with the interstellar medium (ISM). This is particularly the case when the extended emission in the $4.5 \mu\text{m}$ band is in excess with respect to emission in the other IRAC bands.

They were first catalogued by Cyanowski et al. (2008), and later the catalogue was extended by Chen et al. (2013a,b). EGOs are thought to represent the H_2 flows driven by MYSOs (Cyanowski et al., 2008) or MYSO outflow cavities (Takami et

al., 2012). A total of 270 unique EGO targets have been catalogued so far. By original classification (Cyanowski et al., 2008) these targets have a MIPS $24 \mu\text{m}$ detection, usually representing the driving source of the outflow. In order to find the near-infrared counterpart of these driving sources we searched for $2 \mu\text{m}$ sources in the VVV catalogue with a search radius of $1.0''$ and $0.5''$ from the known EGO positions. We find 187 and 153 driving sources. We allowed for sources classified as both point-like and extended to be selected, even though, 80% of the detected sources were point-like. Young stellar objects with disk and outflow activity are often surrounded by circumstellar nebulae in the near-infrared, leading to a classification as extended. These objects were kept in the sample list. Additionally, three colour composites, shown in Fig. 2, were used to visually examine whether the identified point sources are good representations of an outflow driving source. This examination led us to retain the 153 sources which clearly represent $2 \mu\text{m}$ counterparts of the $24 \mu\text{m}$ source, hence the putative driving source of the EGO target.

2.1.2. Non-EGO sample

Kumar et al. (2016) identified a sample of highly variable VVV objects and found MYSO counterparts in ATLASGAL clumps (Contreras et al., 2013). Here an inverse approach is used. Using ATLASGAL, Contreras et al. (2013) and Urquhart et al. (2014) built the Compact Source Catalogue (CSC) which identified ~ 10000 dense clumps. The mass, density, and distance to these clumps are provided by Urquhart et al. (2018) and they are believed to represent active sites of high-mass star formation. Assuming that ATLASGAL clumps host MYSOs, we searched for MIPSgal point-like sources that matched with ATLASGAL CSC sources within a radius of $5''$. This ensured that we matched red point-like sources in $24 \mu\text{m}$ band with the peak emission in the $870 \mu\text{m}$ observations of ATLASGAL. 873 point sources were found with this search. When there were multiple matches we chose the object with the closest centroid distance. The MIPS FWHM is equal to $6''$, therefore, a further search of the 873 targets with a matching radius of $5''$ was performed with the VVV catalogue, allowing us to find 574 K_s -band targets. These 574 targets display more than one K_s band source within the $5''$ radius. In the next step, the point source closest to the MIPS peak was searched for, by constraining the search radius to $1.0''$, only for the 574 targets. This retrieved a list of 2171 sources from the VVV source catalogue. Out of these, any source which had less than ten non-saturated epochs (over the full five-year period) was removed. This led us to find 367 single detections and 147 multiple detections in the centroid search with $r \leq 1''$. The multiple detection targets were examined visually considering the source magnitude, colour and centroid distance, based on which 66 of the 147 sources were rejected, retaining 81 sources. These 448 ($367 + 81$) sources are, therefore, the K_s -band point sources representing the MYSO candidate at the peak of an ATLASGAL clump with a spectral energy distribution (SED) that can be assembled from at least $2 \mu\text{m}$ unto $870 \mu\text{m}$.

The final MYSO sample we produced to study the variability is, therefore, composed of 153 EGO and 448 non-EGO sources, resulting in 601 targets. We note that 66 of the 153 EGO targets also lie within the ATLASGAL clumps, the non-EGO sources being exclusively those that coincide with the peak of ATLASGAL clumps.

2.2. VVV survey data

The VISTA Variables in the Via Lactea (VVV) survey has obtained photometric observations in the near-infrared (NIR) passbands ($0.9\text{--}2.5\ \mu\text{m}$), covering multiple epochs, spread over five years (from 2010 to 2014) and covering a $520\ deg^2$ area of the inner Galactic plane (see Fig. 1) (Minniti et al., 2010). The survey data is made publicly available through the Cambridge Survey Astronomical Unit (CASU), which is the photometry obtained on the final combined ‘tile’ images. A tile image incorporates multiple ‘pawprint’ that are single exposures on sky. The pawprint data (available to the VVV team and also made public at the VISTA Science Archive in Edinburgh), is the basic product of the observations which often holds better photometric and seeing information, as they are better calibrated and tend to have sharper image profiles than the tile data. In this work we have exploited this full potential by using the pawprint photometry.

2.3. Processing of the pawprint photometry

The pawprint photometry and photometric classification used are standard pipeline products from the Cambridge Astronomical Survey Unit (CASU), as detailed in Lewis et al. (2010). Matching and combining detections between multiple pawprints were made following the approach detailed by Smith et al. (2018). Sources are classified according to their morphology and flagged as 1, 0, -1, -2, -3, -7, -9, respectively as; a galaxy, noise, stellar, probably stellar, probable galaxy, bad pixel within $2''$ aperture, and saturated.

The pawprint observing pattern of dithers and overlaps, implies that each source might have between two and six image frames for the same observing epoch, they can also be detected only once along certain edges of the survey. Since these observations are close in time, we chose to bin them together and compute the median magnitude of all observations in intervals of half a day. This binning prevents the detection of variations with timescales smaller than half a day, but reduces the level of scatter in short-periods. The gain in photometric sensitivity will thus be a factor of the number of observations binned, and scales according to \sqrt{n} where n is the number of binned observations. The typical error in the photometry will be $K_{err} \leq 0.05$ mag which allows for the detection of low-level variability. Following the reasoning explained in Smith et al. (2018) we employ the aper-Mag2 ($r \sim 0.71''$) as the K_s magnitude for all analysis.

For each source we assembled a database that contains: a unique identification, median co-ordinates in the ICRS, median magnitude (over half a day) in the K-band, the median absolute deviation (MAD), the standard deviation, the inter-quartile range (IQR), the number of pawprints in which the source was observed, the number of total observed epochs, the modal class, the number of epochs classified with each flag, the K-band magnitude, the quality classifier of the photometry, and the modified Julian date (MJD) of the observation.

The median of the co-ordinates and magnitude, and the modal class were computed for all pawprint observations. The MAD and IQR were computed for each source as they are robust statistical indicators to measure the amplitude and dispersion of the variability (Hampel , 1974; Upton & Cook , 1996; Sokolovsky et al., 2017). These parameters are less sensitive to outliers than the standard deviation. A high value of the MAD or IQR can be a good indicator of the inherent variability of the source. The IQR measures the amplitude of the difference between the third and first quartiles (Q3 and Q1) of a distribution,

in this case the distribution of magnitudes

$$IQR = Q3 - Q1. \quad (1)$$

The MAD is the median of the absolute differences between each data point and the median, as shown by the following equation:

$$MAD = \text{median}(|K_i - \text{median}(K)|) \quad (2)$$

in which, K_i is an observation and K represents all the observations.

2.4. Light curves and their reliability

The light-curves (LCs) of 448 non-EGO and 153 EGO targets were produced in the following way by querying the database assembled above. First, we queried a set of co-ordinates and search radius on the database. Secondly, we built a list with all observations that matched the query. Thirdly, we excluded all saturated observations (modal class = -9). Fourthly, we produced a LC for each target using the difference from median ($K_{median} - K_{mag,i}$).

In the top panel of Fig. 2 we show an example of a LC. To ascertain that the photometry of the target at a given time epoch is not affected by poor observing conditions, flat field errors, improper photometry, or poor seeing, we performed a few tests.

2.4.1. Identifying the variable source

Stellar sources within two annuli defined by $r=1''$ and $r=60''$ from the target were selected. Typically 100-200 sources were found by this selection. For each such source S_i , the magnitude deviation ($\Delta S_{i_{mj}}$) from its median value ($\widetilde{S}_{i_{mj}}$) over all epochs was computed. The median value $\widetilde{\Delta S}_{i_{mj}}$ for all sources in the annulus, is a representation of the photometric deviation (if any) of the individual epoch over the time-line. for each source, at each epoch, the offset $\Delta S_{i_{mj}}$ was added to $\widetilde{S}_{i_{mj}}$ to produce the corrected light curve. The MAD of the deviations for all selected sources, $MAD(\Delta S_{i_{mj}})$, is used as an approximation of the 1σ photometric error of a $1'$ field around the target for a given epoch. And is shown as the error bars in Fig. 2.

2.4.2. Influence of magnitude on variability

Next we assessed the influence of using any and all, or, only sources with magnitudes comparable to that of the target inside the annuli for computing the 1σ error. For this purpose we filtered the sources within a magnitude range ± 1 mag to that of the target, which decreased the number of sources by a factor of approximately ten. Figure 3 illustrates the results of this test. It can be seen that the difference in 1σ error by using the two comparison samples is $K_s \sim 0.0018 - 0.0031$ mag, which is 1-2 orders of magnitude below the typical 1σ errors in the target fields.

2.4.3. Control field test

The targets of study are found in the midst of star forming regions, often deeply embedded in dark clouds, leading to reduced and non-uniform source distribution. Also YSOs (in general) are known to be variable objects, so, many sources in a given field may be variable. To address the influence of these effects, we used a control field region randomly selected to be $5'$ away from the target field. For each control field the steps explained in the two subsections above were executed. We find that the control field variability was very similar to the $MAD(\Delta S_{i_{mj}})$ computed above.

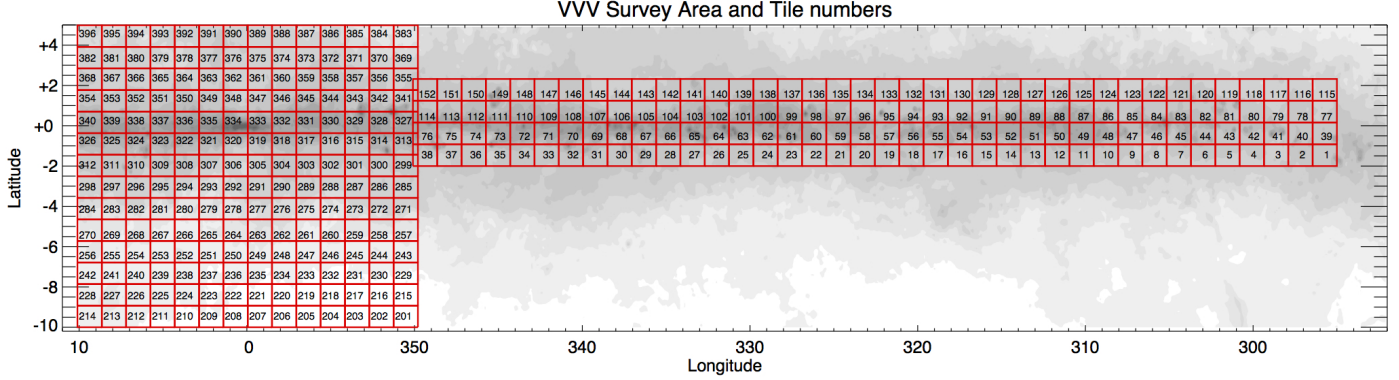


Fig. 1: VVV survey area.

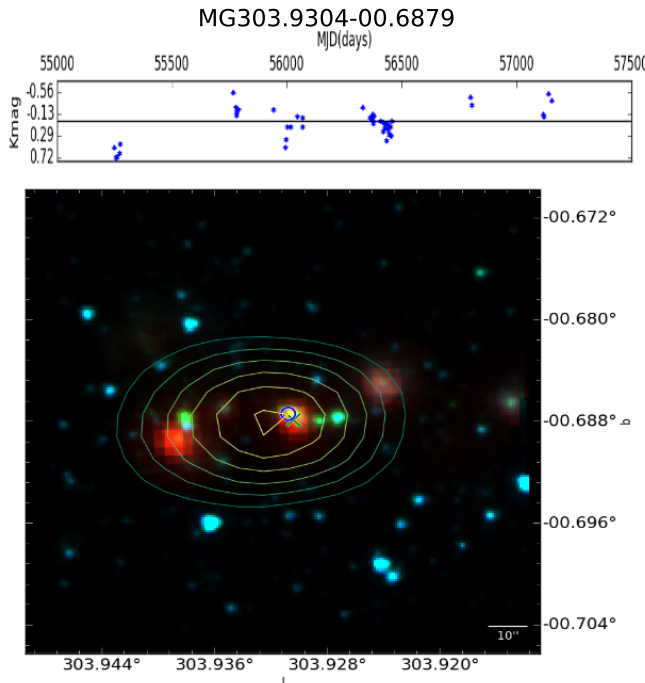


Fig. 2: LC of an eruptive event. Top panel shows the LC of the source, the error bars represent $\text{MAD}(\Delta S_{i_{\text{mag}}})$, the bottom plot shows the RGB image of the source using the Spitzer IRAC 3.6 μm , IRAC 4.0 μm , and the 24 μm MIPS band as blue, green and red, respectively. The VVV source is indicated by the blue circle and the green cross represents the MIPS co-ordinates. The contours of the RGB are in the interval of [Peak- 5σ , Peak] from the ATLASGAL observation at 850 μm .

2.5. Periodograms, false alarm probability, and their aliases

Once the LCs are assembled, we computed the Lomb Scargle periodogram, identify the max power frequency component, and use it to produce a phase-folded LC. Scargle (1982) defined the false alarm probability (FAP) as a measurement of the probability of a signal without any periodic component to have a peak amplitude. The predictive power of the FAP decreases in the presence of correlated noise, non-gaussian errors, and, highly non-sinusoidal variability. The 90%, 95%, and 99% FAP levels have been computed for periodograms of each target.

A given periodicity can, by a compound effect of binning, observational window, and noise, produce harmonics of itself,

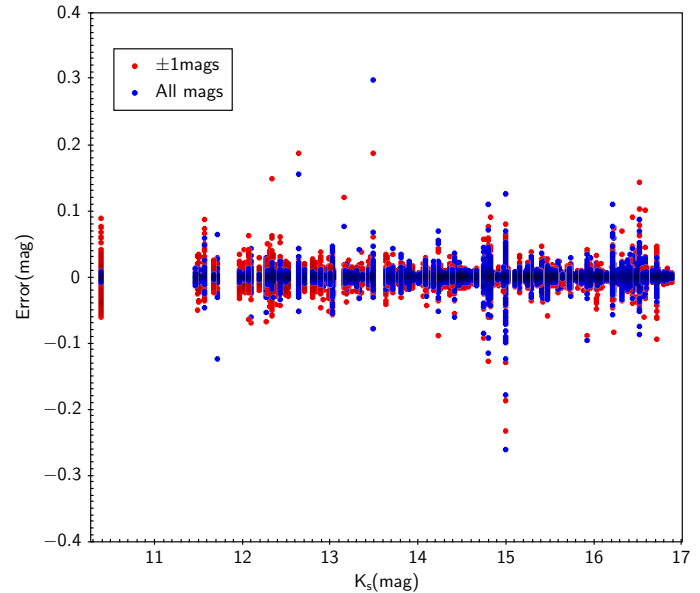


Fig. 3: Systematic errors as a function of the magnitude of each target. The red points represents the case where we only consider the stellar sources with ± 1 mag around our targets. The blue points represent the case in which we consider all stellar sources in the vicinity of our targets.

which appear in the periodograms as additional peaks, or aliases (VanderPlas, 2017). In an effort to verify if the peaks determined were in fact real signals or their aliases, an additional verification step was added. The highest peak of the periodograms and the following 10 highest peaks were identified. Aliases were searched by examining: a) multiples in the frequency range; b) multiples in the period range; and c) solving the following equation:

$$f_i = f_t + n * f_w \quad (3)$$

where f_i is the frequency of the alias, f_t is the true frequency, n is an integer, and f_w is a frequency window, using the windows of 1 year (0.0027 day^{-1}), one day (1 day^{-1}), and a sidereal day (1.0027 day^{-1}), as these are the most common aliases for Earth-based telescopes (VanderPlas, 2017).

2.6. SED analysis

The target samples are generally considered to represent MYSOs based on signposts of high mass star formation and survey shal-

Table 1: Filters and apertures used for building the SEDs.

Filter	Wavelength (μm)	Aperture ($''$)
J	1.235	3
H	1.662	3
K_s	2.159	3
IRAC1	3.6	4
IRAC2	4.5	4
IRAC3	5.8	4
IRAC4	8.0	4
MIPS24	24	6
PACS70	70	5.6
PACS160	160	10.7
SPIRE250	250	17
SPIRE350	350	24
SPIRE500	500	35
AGAL870	870	19.2

lowness. To better understand the nature of the sources studied here in detail for variability, we have analysed their $1.2 \mu\text{m}$ - $870 \mu\text{m}$ spectral energy distributions (SEDs).

The Python version of the SED fitting tool (Robitaille et al., 2007) was used to model SEDs of the target sources. The photometric bands, filter, and apertures used to construct the SEDs can be found on Table 1. The photometric data used to construct the SEDs was obtained from querying the public online archives of 2MASS, SPITZER, ATLASGAL, and Herschel (Huchra et al., 2012; Carey et al., 2009; Schuller et al., 2009; Pilbratt et al., 2010). Our SED fitting follows the method detailed in Grave & Kumar (2009). An uniform photometric error of 10% was assumed. Longer wavelength data were usually set as upper limits, because their large beams include emission from multiple sources, sometimes small clusters, even those that are well resolved at $24 \mu\text{m}$ and below. Data at wavelengths shorter than $24 \mu\text{m}$ are set as data points. However, for the EGO sample, the $4.5 \mu\text{m}$ IRAC band data was set as upper limit by default, as their main characteristic is to have excess emission in that band.

We used a range of extinction of $\text{Av} = 0\text{-}50$ mag for all targets. Distances are available (Urquhart et al., 2018) for 105 targets, non-EGO and EGOs, they were used with an uncertainty of ± 1 kpc while fitting. For the remaining 102 targets we allowed a full plausible range of $d=1\text{-}13$ kpc.

For each target all the models which have a $\chi^2 - \chi^2_{\text{best}} < 3$ were used, and the parameters of the source were computed by performing a weighted mean, weighted by the inverse χ^2 as described in Grave & Kumar (2009). The observational data used to construct the SEDs is listed in the Table A.1 .

3. Results

The LCs of 601 (448 non-EGO + 153 EGO) were visually examined and compared with the source IQR, while considering the deliberation made in Sect. 2.4. We consistently find that an $IQR > 0.05$ is associated with visually $>20\%$ of the data-points in the light-curve that are above the 1σ error of the field, as shown by the error bars for each source.

This selection criteria resulted in 51 (of the 448) non-EGO and 139 (of the 153) EGO targets to be classified as variable sources. They are listed in Table 2, along with the LC classification. In Fig. 4 we display some of the clear LCs of both periodic and aperiodic nature. For each source (see Fig. 5), the LC, periodogram, phase-folded LC, and a three colour composite image of the target is made available.

3.1. Light curve classification

Light curves can be classified based on their behaviour and, often, such classification represents a close connection with certain physical processes. A classification scheme similar to the one used in Contreras Peña et al. (2017) was followed here, and LCs were divided into : a) long period variables (LPV-ysos); b) short timescale variables (STVs); c) dippers and faders; d) eruptive. In defining periodic variables, Contreras Peña et al. (2017) only included periods of the highest power, while we include all significant periods. Four LCs for which we have only a short time coverage were considered to be unclassified.

Long period variables (LPV-ysos) are defined in Contreras Peña et al. (2017) as sources with periodic photometric variability and periods larger than $P > 100$ days. LPV-ysos have periods larger than the stellar rotation or inner disc orbits of young stellar objects, which are typically $P < 15$ days. Figure 5 shows the example of two LPV-ysos, source G309.91+0.32 and G343.50-0.47, which have periods of ~ 545 days, and ~ 1156 days. The RGB image of source G309.91+0.32 reveals distinct extended green emission, a signpost of the presence of an outflow, its periodogram shows a prominent signal well above the 99% FAP level. The source has a median brightness of $K_s = 13.65$ mag in the VVV and the amplitude between the brightest and dimmest point of its LC is ~ 0.81 mag. The other prototypical LPV-ysos selected, G343.50-0.47, and is part of a complex of three MIPS bright sources. It is a source with $K_s=15.38$ mag, the amplitude of its variability is close to ~ 0.86 mag and, the periodogram of the source shows a distinct peak well above the 99% FAP level. There are no aliases in the periodograms of either of these sources.

Short timescale variables are objects with short timescales of periodic variability ($P < 100$ days), or without an apparent periodicity. Periods larger than the stellar rotation or inner disc orbits, $15 < P < 100$ days can be explained by phenomena such as obscuration from circumbinary disc or by variable accretion (Contreras Peña et al., 2017; Bouvier et al., 2003). Sources MG352.2452-00.0636 and G351.78-0.54 are typical examples of STVs, shown in Fig. 6, with typical periods of approximately 29 and 18 days, respectively. Both sources match well ($r < 2''$) with the $870 \mu\text{m}$ emission peak, additionally MG352.2452-00.0636 coincides with an IRDC filament, and G351.78-0.54 is close ($r < 2''$) to the VLA1a source studied by Zapata et al. (2008) as part of a compact cluster of MYSOs. G351.78-0.54 also coincides with an highly variable maser studied by Goedhart et al. (2014).

Faders and dippers are two classes of LCs with aperiodic photometric variability. Dippers are characterized by long-lasting (lasting months to years) dimming events followed by a return to normal brightness, while the same terminology is found in works of the YSOVAR team (Morales-Calderón et al., 2011) they use it to classify phenomena on shorter timescales (hours to days). Faders show light-curves that slowly decline over time, or a period of continuous brightness followed by a sudden decrease sustained over a year. Dippers are often associated with increased extinction from surrounding material. Faders can be caused by either a return to a quiescent accreting phase or a long lasting increase in extinction. It should be noted that both dippers and faders share common LC morphologies and can be easily mistaken for one another. A snapshot of a dipper event not returning to normal brightness can likely be mistaken as a fader. Source MG328.0494-00.0487 (Fig. 7) is the prototypical example of a fader event. It matches the peak emission of the ATLASGAL observations, and is an extended object in the

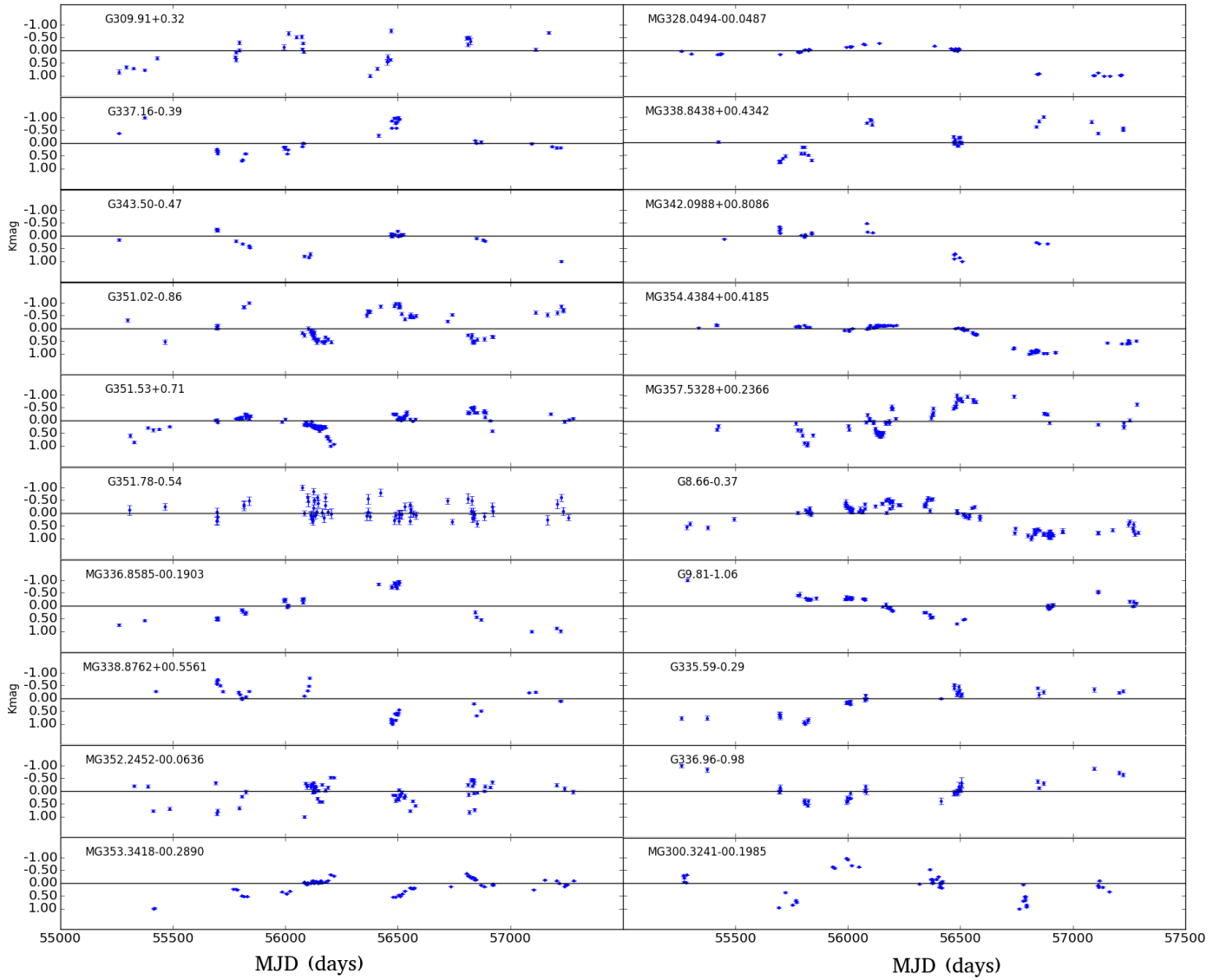


Fig. 4: Some of the clearer LCs, periodic (left column) and aperiodic (right column). Each figure shows the LC of the source, error bars represent $\text{MAD}(\Delta S_{imjd})$. The vertical axis represents the variability from the median normalized by $\max(|K_i - \text{median}(K)|)$.

Table 2: Source co-ordinates, photometric data and variability

Source	RA (deg)	DEC (deg)	K_s (mag)	MAD (mag)	IQR (mag)	ΔK_s (mag)	Class	Period (day)
MG303.9304-00.6879	195.10156	-63.54177	15.21	0.15	0.33	1.28	Erup	NA
MG328.0494-00.0487	238.7064	-53.7280	12.28	0.149	0.278	1.83	Fad	NA
MG352.2452-00.0636	261.5178	-35.5005	15.95	0.079	0.166	0.53	STV	29.4
MG354.4384+00.4185	262.5086	-33.4088	14.66	0.091	0.523	0.89	Dip	NA
G309.91+0.32	207.7246	-61.7394	13.65	0.204	0.383	0.81	LPV-yso	545.9
G335.59-0.29	247.7437	-48.7308	13.16	0.097	0.348	0.61	low-Erup	NA
G351.78-0.54	261.6775	-36.1536	14.46	0.06	0.12	0.38	STV	18.3
G343.50-0.47	255.3267	-42.8267	15.38	0.10	0.18	0.86	LPV-yso	1156.3

For full table check the online data.

8 μm *Spitzer* band, it has a close-by companion. There is no clear peak in its periodogram and the LC shows some periodic variability until around MJD 56500, at which point there is a drop in brightness of close to $\Delta K \sim 1.4$ mag. The morphology of Dipper events is typified by source MG354.4384+00.4185 which is plotted in Fig. 8. There is no clear peak in its periodogram, and its light curve could be considered as non-variable,

except for an abrupt drop in brightness of $\Delta K \sim 0.8$ until the target recovers more than half its brightness about 750 days later.

Eruptive LCs are also aperiodic, but they are characterized by outbursts and increases in brightness, typically over periods of months or years but, in some cases, lasting a few weeks. Objects with increases in their luminosity, likely from ongoing accretion events, will produce such LCs. FUors or EXors are

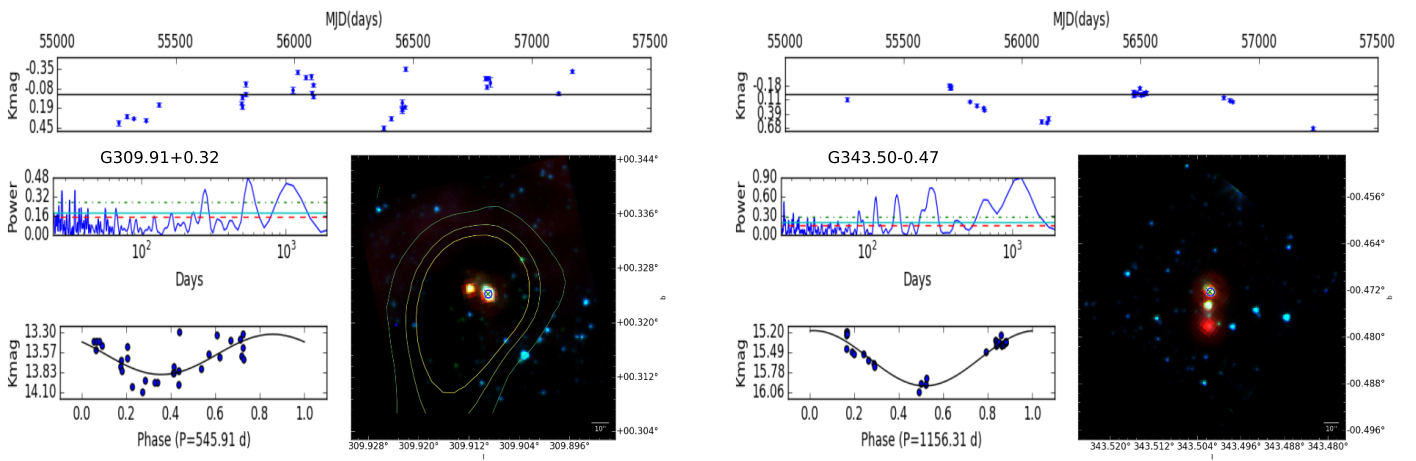


Fig. 5: Prototypical LPV-ysos sources: Top panel for each figure shows the LC of the source, error bars represent $\text{MAD}(\Delta S_{i_{mj}})$, the left middle panel shows the corresponding periodogram in logarithmic scale (also plotted are the 99%, 95%, and 90% false probability levels, respectively: the green dot-dashed line, the cyan full line, and the red dashed line), the bottom left panel shows the phase-folded light curve of the source using the best period fitted (also shows the corresponding value in days), the bottom right plot shows the RGB image of the source using the Spitzer IRAC 3.6 μm , IRAC 4.0 μm , and the 24 μm MIPS band as blue, green and red, respectively. The VVV source is indicated by the blue circle and the green cross represents the MIPS co-ordinates. The contours of the RGB are in the interval of [Peak- 5σ , Peak] from the ATLASGAL observation at 850 μm .

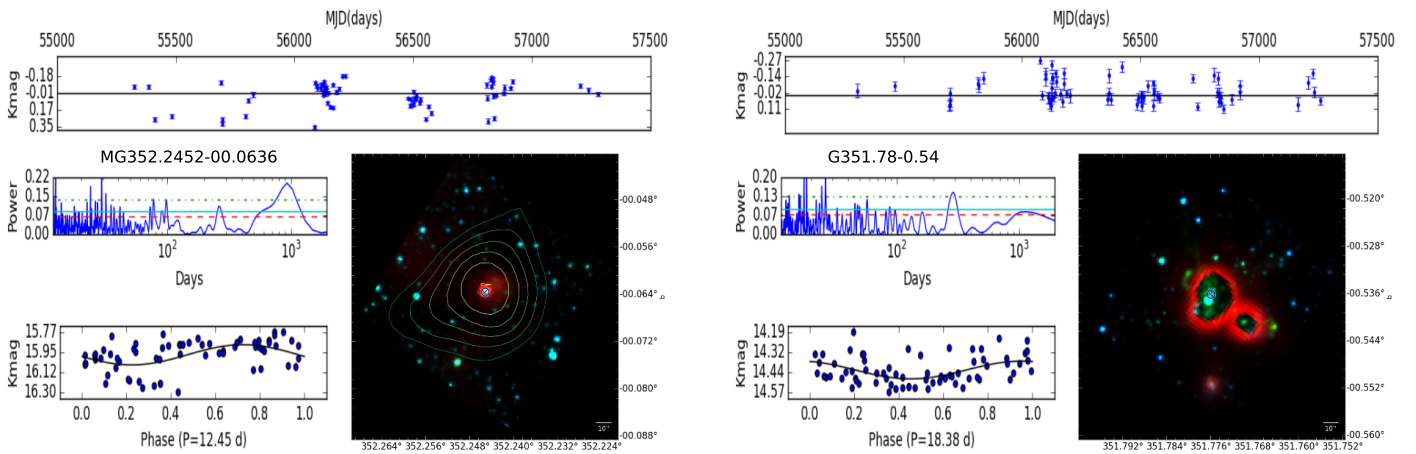


Fig. 6: Prototypical STV sources: Top panel for each figure shows the LC of the source, error bars represent $\text{MAD}(\Delta S_{i_{mj}})$, the left middle panel shows the corresponding periodogram in logarithmic scale (also plotted are the 99%, 95%, and 90% false probability levels, respectively: the green dot-dashed line, the cyan full line, and the red dashed line), the bottom left panel shows the phase-folded light curve of the source using the best period fitted (also shows the corresponding value in days), the bottom right plot shows the RGB image of the source using the Spitzer IRAC 3.6 μm , IRAC 4.0 μm , and the 24 μm MIPS band as blue, green and red, respectively. The VVV source is indicated by the blue circle and the green cross represents the MIPS co-ordinates. The contours of the RGB are in the interval of [Peak- $5 \times \sigma$, Peak] from the ATLASGAL observation at 850 μm .

classic examples showing eruptive morphologies. Similarly to Medina et al. (2018) we employ a subdivision of the eruptive class, ‘low amplitude eruptives’ for sources with $\Delta K < 1.0$ mag. This distinction is made to emphasize that such variations are much less extreme than those in FUors and EXors in the optical wavelengths, and more similar to common short term variability in their amplitude. Nevertheless, for certain disk geometries and high extinction it is possible for a FUor or EXor-like eruption to appear as low-amplitude variability in the NIR. A low-amplitude eruptive LC can either correspond to a low-amplitude variable source or to a high-amplitude source with a geometry + extinction combination such that it appears as low-amplitude in

the K_s band. Overall, there are 26 low-amplitude eruptives and 15 normal eruptives in our samples. While this identification is presented in Table 2, for the analysis they were not considered as separate classes.

One source that features an ongoing eruptive event is MG303.9304-00.6879, plotted in Fig. 2, showing multiple stages of increased brightness over the entire time-line, with two large amplitude brightness changes over years. Figure 9 shows an example of low-amplitude eruptive LC. This source, G335.59-0.29, displays C-shaped green emission, characteristic of jet emission. The main feature of this LC is its sustained increase in brightness over time, with a total amplitude of $\Delta K \sim 0.68$

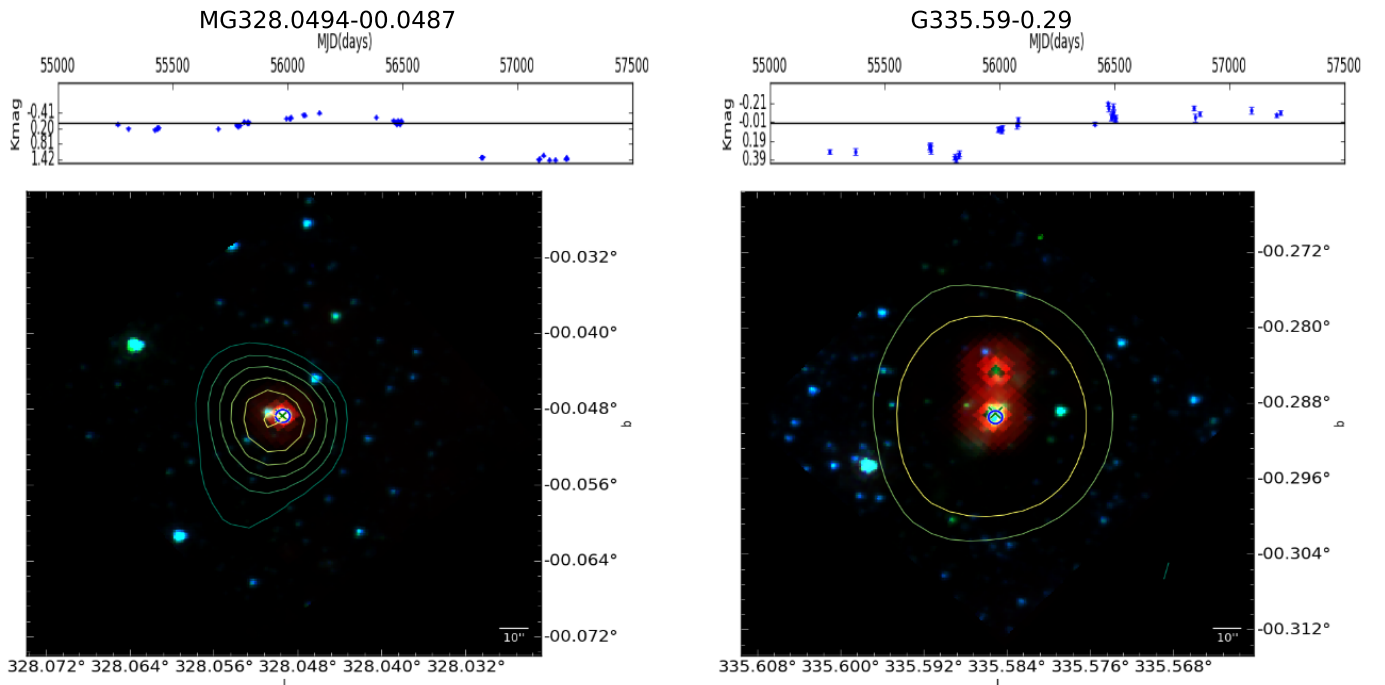


Fig. 7: Typical Fader event. Colours and symbols are the same as in Fig. 5.

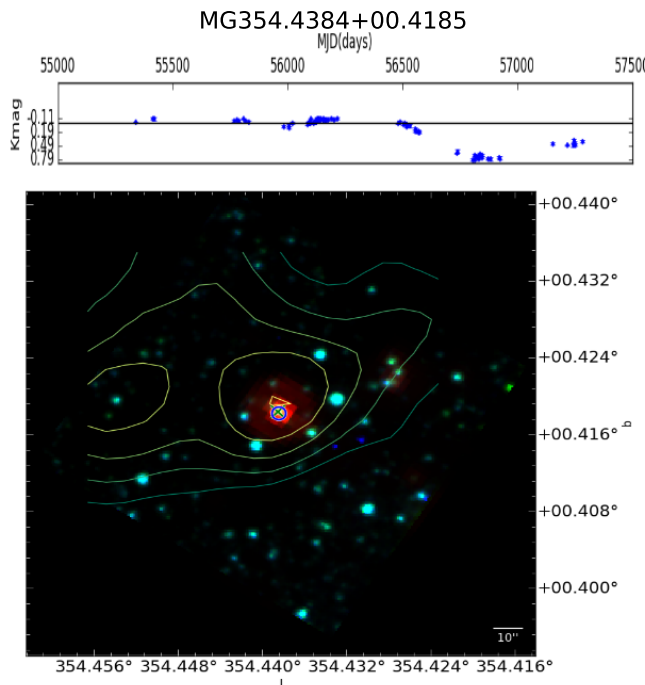


Fig. 8: LC of a dipper event. Colours and symbols are the same as in Fig. 5.

mag. Overall, the variable sources can be split into the periodic category, composed of LPV-ysos and STVs, or the aperiodic category, including faders, dippers, and eruptive sources. Their detailed distributions represented by the different MYSO samples can be found in Table 3. Analysis of periodogram aliases (see Sect. 2.4) indicates that 1 and 15 members of the non-EGO +

Fig. 9: LC of the example of a low-amplitude eruptive event. Colours and symbols are the same as in Fig. 5.

Table 3: Observed parameters of LC classes, for both EGO and non-EGO samples.

LC classification	EGO	non-EGO	Total
Periodic	90 (~ 65%)	21 (~ 41%)	111
Aperiodic	49 (~ 35%)	30 (~ 59%)	79
LPV-ysos	53 (~ 38%)	9 (~ 18%)	62
STV	37 (~ 27%)	12 (~ 23%)	49
Dipper	15 (~ 11%)	5 (~ 10%)	20
Fader	13 (~ 9%)	5 (~ 10%)	18
Eruptive	21 (~ 15%)	20 (~ 39%)	41

EGO samples, respectively, could be classified differently (see also Sect. 4).

The sources MG300.3241-00.1985, MG322.4833+00.6447, MG342.3189+00.5876 have also been studied as highly variable objects (Contreras Peña et al., 2017; Kumar et al., 2016). Of these, MG300.3241-00.1985 was studied spectroscopically by Contreras Peña et al. (2017) and classified as an eruptive MNor, an object with a mixture of characteristics from FUors and EXors. We note that other $\Delta K > 1$ mag sources listed here were not found in Contreras Peña et al. (2017) because they were not highly variable in the 2010-2012 period.

3.2. Variable source SEDs

The goal of SED fitting was to test if the variable targets indeed represent MYSOs. The SEDs of the variable sources were fitted by YSO models (Robitaille et al., 2006) (see Sect. 2.6) allowing us to constrain the properties of these objects. The results of this fitting procedure can be found in table A.2. This table contains the full sample of variables with 190 entries. However, as mentioned in Sect. 2.6 only 105 targets have known distances, where the SEDs can be reasonably constrained. We note that in those cases where distances are not available, fitting with the

full range of 1-13 kpc has resulted in some model fits that outputs sub-stellar masses. This result is likely to be a consequence of unknown distance rather than the true nature of the source because the indicators of high-mass star formation used in the original selection are more reliable. In Fig. 10, the data and model fits can be visualized for the example targets with different LC classes mentioned in the previous section. The masses of these example targets range from 1.84 to 10.30 M_{\odot} , with luminosities between 57 and 6918 L_{\odot} , representing evolutionary ages between 10^4 to 10^6 yrs. Table 4 summarizes the SED results by listing various properties of the sources grouped in mass ranges roughly separating the low, intermediate, and high-mass sources. It can be seen that about $\sim 35\%$ of the targets are modelled in the $4-8 M_{\odot}$ range and only 6% representing $\geq 8 M_{\odot}$ objects. A large fraction ($\sim 60\%$) are fitted with YSO models representing sources with $M < 4 M_{\odot}$.

The $4-8 M_{\odot}$ sources display $\dot{M}_{env} \sim 10^{-4} M_{\odot} yr^{-1}$, $\dot{M}_{Disk} \sim 10^{-6} M_{\odot} yr^{-1}$ and a few hundred solar luminosities. The number of EGO and non-EGO sources fitted as low, intermediate, and high-mass stars are 87, 45, 10 and 25, 21, 1 respectively. It is worth noting that all but one of the sources fitted by models $\geq 8 M_{\odot}$ are EGO objects. These SEDs are well-fitted by MYSO models similar to those represented in Grave & Kumar (2009). Four of the 11 objects ($\geq 8 M_{\odot}$) are included in the 6.7 GHz class II methanol maser surveys and they show emission. These four also show class I methanol maser emission.

4. Discussion

The results show that 139 of 156 (91%) EGO sample presents variability in contrast to 51 of the 433 (12%) non-EGO targets, implying that variability is strongly correlated with the outflow activity in MYSOs. Table 3 summarizes the variability statistics. More than half (64%) of the variable EGOs are classified as periodic contrasting more than half (59%) of the non-EGO sample that are classified as aperiodic. Table 5 allows us to discern the differences between EGO and non-EGO samples, and sources classified as periodic or otherwise. It can be seen from Fig. 11 and Table 5, that the amplitude range of variation in non-EGOs is roughly twice as much as that of EGOs. Of the modelled parameters, the circumstellar extinction ($A_{V,circum}$) for non-EGO targets clearly stand out as twice the median value for EGOs. Also, it appears that non-EGO variable sources may simply be more luminous objects located in slightly farther away targets. Together, the ΔK_s , Av and L comparison indicate that the non-EGO variable sources are relatively more embedded objects when compared to EGOs.

The results of the search for aliases among the ten frequencies with greater power, found aliases for the highest peak of the periodogram in five non-EGO targets ($\sim 9\%$), and 22 ($\sim 15\%$) EGO targets. Of these, only 1 ($\sim 2\%$) of the non-EGO targets would change their classification from LPV-ys to STV, while, for the EGO sample 15 ($\sim 10\%$) of the targets could change from LPV-YSO to STV or vice-versa. Therefore, these aliases would not change any periodic to aperiodic source, as period length is not the only condition defining a periodic source (LC morphology is also one of the main factors).

It can be seen from Fig. 12 that the envelope accretion rate (see also Table 5) for non-EGO sources is an order of magnitude smaller than that for the EGO sources. The same effect can be noticed for aperiodic sources (bottom panel). We note that the non-EGOs are dominated by aperiodic sources, that should be indicative of the differences observed in the top and bottom panels of Fig. 12. Aperiodic LCs, represented by eruptive, dip-

pers and fader classes, are thought to trace objects with low level of quiescent accretion, that will undergo short periods of intense accretion. The lower level of accretion found in these objects can therefore be explained by this behaviour.

We compared the SED fitted model properties with the amplitude of variation and did not find any correlations to understand the variability as a function of mass, accretion rate, luminosity or temperature. Figure 13 shows an HR diagram, by plotting the luminosity versus temperature of all variable sources derived from the SED fitting. The zero-age-main-sequence (ZAMS) curve (Siess et al., 2000) is shown by a solid curve. The seven dashed curves display the pre-main-sequence tracks (also from Siess et al. (2000), for solar metallicity) for objects of $1-7 M_{\odot}$ in steps of $1 M_{\odot}$. EGOs are concentrated closer to the putative birth-line position of the massive stars and are also largely lower mass objects ($< 4 M_{\odot}$). The precursor to a high mass star is considered to be a lower mass object which continues to accrete material for more than half of its life until it contracts on the main sequence. In view of that conjecture, it is not surprising that a majority of the EGO driving sources are modelled by young low to intermediate mass stars. Furthermore, the HR diagram, with the associated PMS tracks, validates the fitted masses.

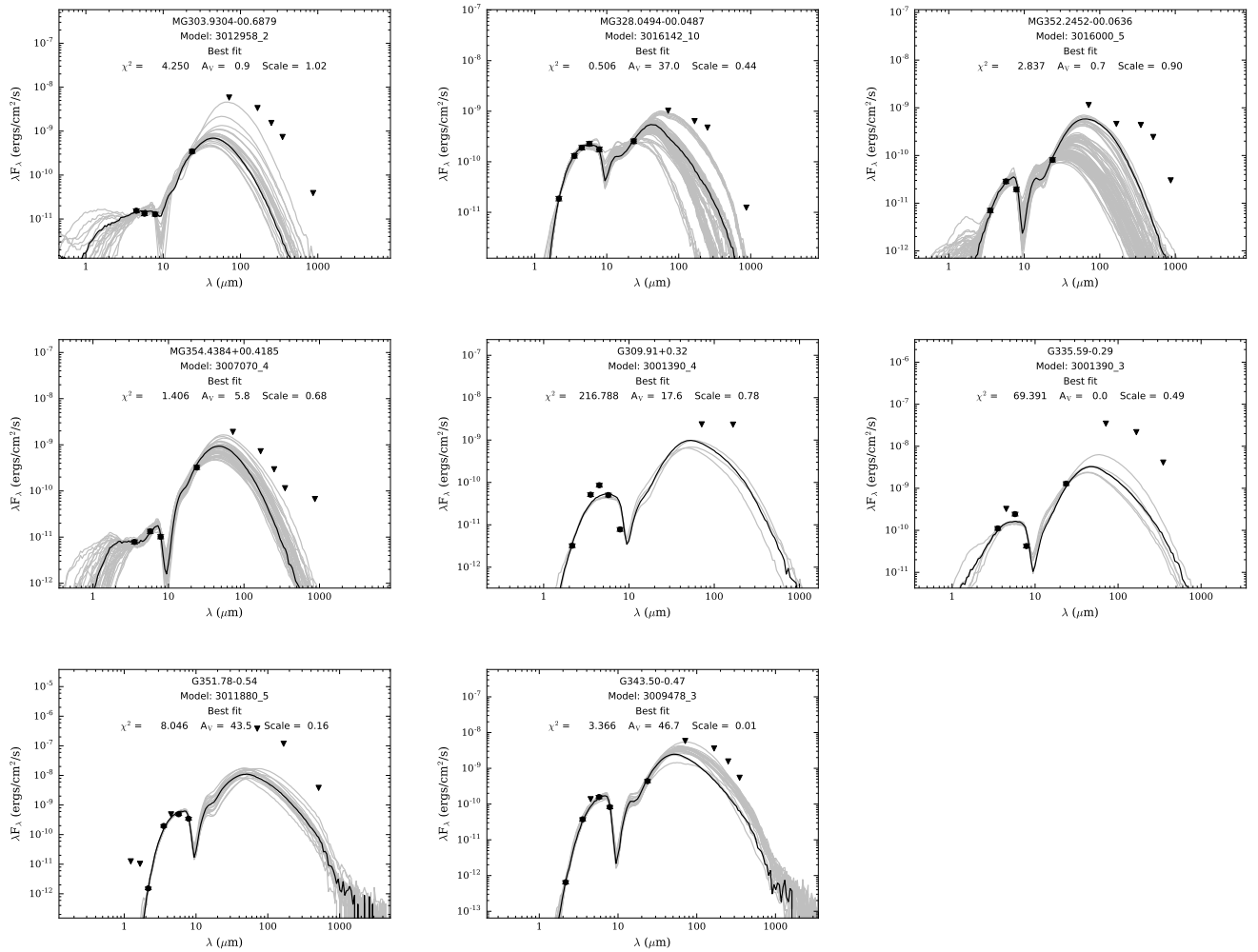
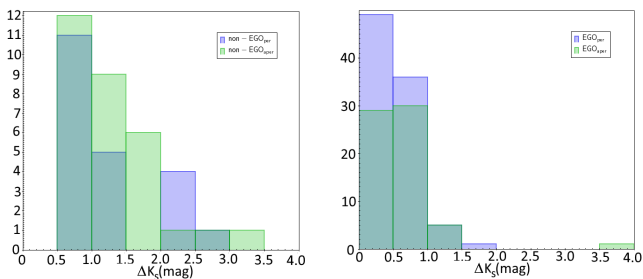
Most parameters resulting from SED fitting are model dependent, with known correlations within the model grid between the age, mass and accretion rates (Robitaille et al., 2006). However, the observed data is scaled to match the luminosity and temperature of the selected models from the grid, therefore, these are relatively more reliable fitted parameters. Unlike the lower mass stars, the luminosity and temperature differences prominently distinguish the sparsely populated massive stellar models in the grid. These two parameters are used for comparison in this analysis, to ensure that the inferences made are reasonably free of biases in the grid models.

There is an apparent concentration of non-EGO objects, probably with slightly more higher mass objects on the ZAMS. It was previously noted that the non-EGO targets are significantly more embedded objects displaying larger ΔK_s compared to EGOs. The objects located closer to the ZAMS may therefore be candidate sources to test the hypothesis of bloated and pulsating young massive stars. Hosokawa et al. (2010) argue that high-mass stars are bloated objects. Such objects are also thought to be pulsationally unstable, or at least go through a period of significant pulsations as they settle down on the ZAMS (Inayoshi et al., 2013). Contreras Peña et al. (2017) indicates that eruptive variable behaviour is more common or recurs more frequently at earlier stages of stellar PMS. The analysis in this work show that $\sim 70\%$ eruptive variables are concentrated on the birthline and the ZAMS in nearly half proportion. Protostellar envelopes are a prominent feature of objects located on the birthline, therefore suggesting that most eruptive MYSOs are indeed the result of envelope accretion. High-mass protostellar objects ingesting a burst of accreting matter enter a ‘bloated phase’ before re-adjustment and contraction (Hosokawa et al., 2010). This could be the case for those eruptive sources located on the ZAMS.

In Table 6, all the variable sources (32 targets) with known 6.7 GHz class II methanol maser detection are listed, along with, the simultaneous detection of class I methanol maser. Those sources with only class I methanol maser detections are not listed. The detection of class II methanol maser is considered as a strong sign-post of high-mass star formation, especially massive outflow activity (de Villiers et al., 2015). Of the 32 sources, only two are non-EGOs, therefore, reinstating the association of class II methanol masers with MYSO outflow activity. Goedhart et al.

Table 4: SED results by mass bin.

M (M _⊙) Range	Sources (%) Ratio	L (L _⊙) Range	L (L _⊙) Median	\dot{M}_{env} (M _⊙ yr ⁻¹) Range	\dot{M}_{env} (M _⊙ yr ⁻¹) Median	\dot{M}_{disk} (M _⊙ yr ⁻¹) Range	\dot{M}_{disk} (M _⊙ yr ⁻¹) Median	A _{Vcircum} Range	A _{Vcircum} Median
$M < 4$	~ 59	[4.0E-1,9.0E2]	5.0E1	[0,4E-4]	1.3E-5	[-8E-3,4E-5]	2E-7	[6E-1,6E5]	74
$4 \leq M < 6$	~ 21	[8.8E1,1.2E3]	2.9E2	[0,4E-4]	7.8E-5	[-4E-2,9E-6]	6E-7	[2E0,2E4]	56
$6 \leq M < 8$	~ 14	[2.9E2,5.1E3]	9.3E2	[0,6E-4]	2.0E-4	[-2E-1,3E-5]	2E-6	[5E0,1E5]	66
$8 \leq M$	~ 6	[1.3E3,3.7E4]	3.0E3	[1E-4,4E-3]	2.8E-4	[-1E0,4E-6]	-2E-3	[4E1,4E5]	228

Fig. 10: Grid of SEDs for our prototypical sources. The dark line corresponds to the best fit model. The grey lines correspond to other $\chi^2 - \chi^2_{best} < 3$ models.Fig. 11: Histogram of ΔK divided by sample and periodicity. EGO and non-EGO sources are shown, respectively, on the right and left plots.

(2014) have studied variability of methanol masers, and two of the infrared variable sources presented here, G351.78-0.54 and G298.26+0.74, were analysed in that study and G351.78-0.54 is considered as an highly variable maser, while G298.26+0.74 does not present maser variability above instrumental noise.

Our selection criteria for non-EGO sources, 24 μ m MIPS sources matching ATLASGAL CSC objects ($r < 5''$) might lead us to miss some of the most important sources in the clumps. Since the most luminous source inside each clump can be offset by more than $r < 5''$ we have missed many of the MYSOs in these regions. The criteria used ensures that the targets are good MYSO candidates but, the most luminous FIR sources and their counterparts will be examined in a future work.

Table 5: Summary of the median fit parameters, for both EGO and non-EGO samples divided by periodicity.

Parameter	EGO	non-EGO	Periodic	Aperiodic
ΔK_s (mag)	0.52	1.02	0.58	0.69
Period (days)	312	416	126	-
M (M_\odot)	3.2	3.8	3.2	3.6
M ($M_\odot \text{ yr}^{-1}$)	4E-5	6E-6	4E-5	2E-5
\dot{M}_{disk} ($M_\odot \text{ yr}^{-1}$)	3E-7	7E-7	3E-7	6E-7
L (L_\odot)	125	212	125	190
Age (Myr)	5.0	5.6	5.0	5.0
T (K)	4841	7795	4857	5990
$A_{V_{\text{circum}}}$	61	125	71	54

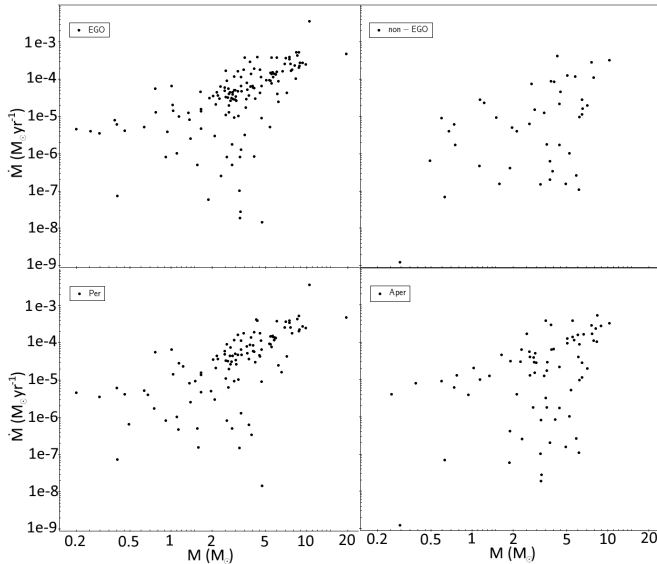


Fig. 12: Mass versus envelope-accretion rate for the fitted SEDs of EGO and non-EGO sources, in logarithmic scale. EGO, non-EGO, periodic, and aperiodic, are plotted at the top left, top right, bottom left, and bottom right, respectively.

5. Summary

This study has investigated the nature of near-infrared variability in MYSOs, focusing on the driving sources of EGOs and luminous $24 \mu\text{m}$ point sources coinciding within $5''$ of the massive star forming clumps mapped at $870 \mu\text{m}$ by ATLASGAL. The search led us to examine the K_s -band light-curves of 718 point sources.

- 190 sources (139 EGOs and 51 non-EGOs) were found to be variable with an $\text{IQR} > 0.05$ and $\Delta K_s > 0.15$. 111 and 79 of these objects are classified as periodic + aperiodic, respectively.
- The $2\mu\text{m}$ - $870\mu\text{m}$ spectral energy distribution of the variable point sources were assembled and fitted with YSO models. 47 and 6 sources were modelled as $\geq 4 M_\odot$ and $\geq 8 M_\odot$, respectively.
- On an HR diagram, most lower mass EGO sources concentrate along a putative birth-line.
- A high rate of detectable variability in EGO targets (139 out of 153 searched) implies that near-infrared variability in MYSOs is closely linked to the accretion phenomenon and outflow activity.

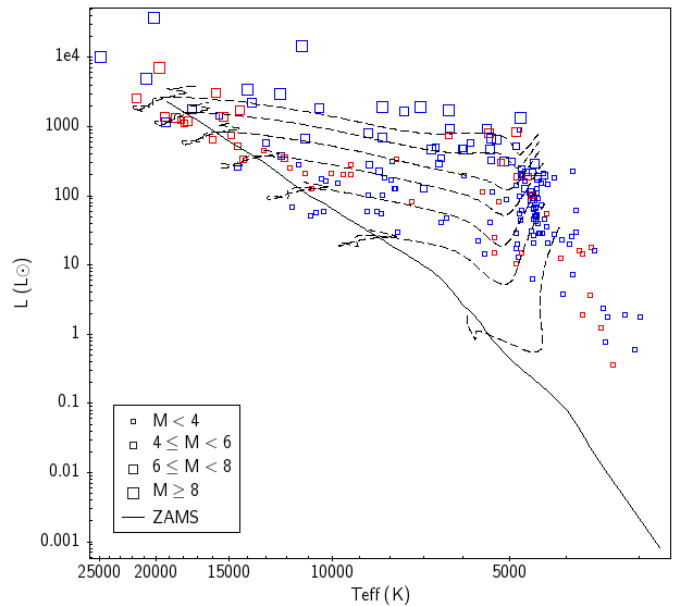


Fig. 13: HR diagram for our sources. Symbol size corresponds to $M < 4$, $4 \leq M < 6$, $6 \leq M < 8$, $M \geq 8 M_\odot$, from smaller to larger, respectively. The dashed lines (from bottom to top) are the PMS tracks for 1, 2, 3, 4, 5, 6, and 7 M_\odot , the filled line is the ZAMS. Blue and red symbols are, respectively, EGOs and non-EGOs.

Further to the discovery of a dozen high-amplitude variable MYSOs (Kumar et al., 2016), this is the first large scale systematic study of near-infrared variability in MYSOs. The variable sources identified in this work are excellent targets with which to undertake follow-up studies to understand the circumstellar environment of MYSOs in detail.

Acknowledgements. G.D.C.T. is supported by an FCT/Portugal PhD grant PD/BD/113478/2015. MSNK acknowledges the support from Fundação para a Ciência e Tecnologia (FCT) through Investigador FCT contracts IF/00956/2015/CP1273/CT0002, and the H2020 Marie-Curie Intra-European Fellowship project GESTATE (661249). Support for JB is provided by the Ministry of Economy, Development, and Tourism's Millennium Science Initiative through grant IC120009, awarded to The Millennium Institute of Astrophysics, MAS. A.C.G. has received funding from the European Research Council (ERC) under the European Unions Horizon 2020 research and innovation programme (grant agreement No. 743029). PWL acknowledges the support of consolidated grants (ST/R000905/1 and ST/M001008/1) funded by the UK Science and Technology Facilities Research Council. CCP acknowledges support from the Leverhulme Trust. JFG is supported by Fundação para a Ciência e a Tecnologia (FCT) through national funds (UID/FIS/04434/2013) and by FEDER through COMPETE2020 (POCI-01-0145-FEDER-007672).

References

- Audard, M., Ábrahám, P., Dunham, M. M., et al. 2014, Protostars and Planets VI, 387
 Bally, J., Aguirre, J., Battersby, C., et al. 2010, ApJ, 721, 137-163
 Bernasconi, P. A., & Maeder, A. 1996, A&A, 307, 829
 Bouvier, J., Grankin, K. N., Alencar, S. H. P., et al. 2003, A&A, 409, 169
 Broos, P. S., Getman, K. V., Povich, M. S., et al. 2013, ApJS, 209, 32
 Caratti o Garatti, A., Stecklum, B., Linz, H., Garcia Lopez, R., & Sanna, A. 2015, A&A, 573, A82
 Caratti o Garatti, A., Stecklum, B., Garcia Lopez, R., et al. 2017, Nature Physics, 13, 276
 Carey, S. J., Noriega-Crespo, A., Mizuno, D. R., et al. 2009, PASP, 121, 76
 Caswell, J. L., Fuller, G. A., Green, J. A., et al. 2010, MNRAS, 404, 1029
 Chambers, E. T., Yusef-Zadeh, F., & Ott, J. 2014, A&A, 563, A68
 Chen, X., Gan, C.-G., Ellingsen, S. P., et al. 2013, ApJS, 206, 9
 Chen, X., Gan, C.-G., Ellingsen, S. P., et al. 2013, ApJS, 206, 22

Table 6: EGO and non-EGO MYSO candidates with nearby methanol masers.

Source	K_{mag} (mag)	IQR (mag)	Distance (kpc)	Class	ClassII Maser	ClassI Maser
MG003.5016-00.2020	16.07	0.23	5.0	Erup	Y	
MG006.9222-00.2512	14.38	0.26	3.0	Erup	Y	Y
MG332.3652+00.6046	14.17	0.09	2.7	Fad	Y	Y
MG333.0294-00.0149	15.24	0.18	4.0	Dip	Y	N
MG339.2939+00.1387	15.63	0.41	4.8	STV	Y	
MG339.5843-00.1282	13.16	0.16	2.6	Dip	Y	Y
MG345.5764-00.2252	15.33	0.3	7.9	Erup	Y	
MG352.6040-00.2253	15.38	0.22	7.6	Erup	Y	
MG358.4604-00.3929	16.03	0.16	5.0	LPV-yso	Y	Y
G9.62+0.20	14.38	0.11	5.2	STV	Y	Y
G6.19-0.36	14.52	0.09	5.1	STV	Y	Y
G5.62-0.08	15.43	0.07	5.1	LPV-yso	Y	Y
G359.44-0.10	14.99	0.13		LPV-yso	Y	Y
G358.84-0.74	13.82	0.12	6.8	LPV-yso	Y	Y
G358.46-0.39(b)	15.45	0.16	2.9	STV	Y	Y
G358.39-0.48	13.93	0.19	2.4	Erup	Y	Y
G358.26-2.06	12.26	0.08	3.0	Fad	Y	
G355.54-0.10	14.08	0.15	3.0	LPV-yso	Y	Y
G355.18-0.42	14.98	0.08	1.2	Erup	Y	Y
G353.46+0.56	13.18	0.1	11.2	LPV-yso	Y	Y
G352.63-1.07	14.56	0.14	0.9	STV	Y	Y
G352.58-0.18	15.62	0.09	5.1	LPV-yso	Y	
G352.13-0.94	12.79	0.1	2.3	LPV-yso	Y	Y
G351.78-0.54	14.46	0.12	0.7	STV	Y	Y
G351.69+0.17	14.91	0.05	12.1	STV	Y	
G351.38-0.18	15.8	0.07	5.6	STV	Y	N
G351.16+0.69	10.4	0.15	1.8	STV	Y	Y
G350.52-0.35	15.02	0.17	3.1	Erup	Y	N
G350.36-0.07	14.31	0.09	11.2	Fad	Y	
G2.54+0.20	12.71	0.09	4.0	LPV-yso	Y	N
G2.14+0.01	13.03	0.03	11.2	Non-var	Y	
G0.09-0.66	13.87	0.08	8.2	STV	Y	Y

- Contreras Peña, C. E. 2015, Ph.D. Thesis
- Contreras Peña, C., Lucas, P. W., Minniti, D., et al. 2017, MNRAS, 465, 3011
- Contreras Peña, C., Lucas, P. W., Kurtev, R., et al. 2017, MNRAS, 465, 3039
- Contreras, Y., Schuller, F., Urquhart, J. S., et al. 2013, A&A, 549, A45
- Csengeri, T., Leurini, S., Wyrowski, F., et al. 2016, A&A, 586, A149
- Cyganowski, C. J., Whitney, B. A., Holden, E., et al. 2008, AJ, 136, 2391-2412
- de Villiers, H. M., Chrysostomou, A., Thompson, M. A., et al. 2015, MNRAS, 449, 119
- Dunham, M. M., & Vorobyov, E. I. 2012, ApJ, 747, 52
- Dunham, M. M., Stutz, A. M., Allen, L. E., et al. 2014, Protostars and Planets VI, 195
- Eiroa, C., Oudmaijer, R. D., Davies, J. K., et al. 2002, A&A, 384, 1038
- Goedhart, S., Maswanganaye, J. P., Gaylard, M. J., & van der Walt, D. J. 2014, MNRAS, 437, 1808
- Grave, J. M. C., & Kumar, M. S. N. 2009, A&A, 498, 147
- Gutermuth, R. A., & Heyer, M. 2015, AJ, 149, 64
- Hampel, F. R. 1974 The influence curve and its role in robust estimation, Journal of the American Statistical Association, 69 (346), pp. 383-393
- Hartmann, L., Kenyon, S. J., & Calvet, N. 1993, ApJ, 407, 219
- Hayashi, C. 1966, ARA&A, 4, 171
- Herbst, W., & Shevchenko, V. S. 1999, AJ, 118, 1043
- Heyer, M., Gutermuth, R., Urquhart, J. S., et al. 2016, A&A, 588, A29
- Hosokawa, T., Yorke, H. W., & Omukai, K. 2010, ApJ, 721, 478
- Huchra, J. P., Macri, L. M., Masters, K. L., et al. 2012, ApJS, 199, 26
- Hunter, T. R., Brogan, C. L., MacLeod, G., et al. 2017, ApJ, 837, L29
- Inayoshi, K., Hosokawa, T., & Omukai, K. 2013, MNRAS, 431, 3036
- Kenyon, S. J., Hartmann, L. W., Strom, K. M., & Strom, S. E. 1990, AJ, 99, 869
- Kenyon, S. J., & Hartmann, L. 1995, ApJS, 101, 117
- Kesseli, A. Y., Petkova, M. A., Wood, K., et al. 2016, ApJ, 828, 42
- K”onig, C., Urquhart, J. S., Csengeri, T., et al. 2017, A&A, 599, A139
- Kumar, M. S. N., & Grave, J. M. C. 2007, A&A, 472, 155
- Kumar, M. S. N., Contreras Peña, C., Lucas, P. W., & Thompson, M. A. 2016, ApJ, 833, 24
- Larson, R. B. 1969, MNRAS, 145, 271
- Lewis, J. R., Irwin, M., & Bunclark, P. 2010, Astronomical Data Analysis Software and Systems XIX, 434, 91
- Li, G.-X., Urquhart, J. S., Leurini, S., et al. 2016, A&A, 591, A5
- Makin, S. V., & Froebrich, D. 2018, ApJS, 234, 8
- McKee, C. F., & Offner, S. S. R. 2010, ApJ, 716, 167
- Medina, N., Borisssova, J., Bayo, A., et al. 2018, arXiv:1806.04061
- Meyer, D. M.-A., Vorobyov, E. I., Kuiper, R., & Kley, W. 2017, MNRAS, 464, L90
- Meyer, D. M.-A., Vorobyov, E. I., Kuiper, R., & Kley, W. 2017, arXiv:1710.02320
- Minniti, D., Lucas, P. W., Emerson, J. P., et al. 2010, New A, 15, 433
- Morales-Calderón, M., Stauffer, J. R., Hillenbrand, L. A., et al. 2011, ApJ, 733, 50
- Myers, P. C. 2010, ApJ, 714, 1280
- Ochsenbein, F., Bauer, P., & Marcout, J. 2000, A&AS, 143, 23
- Pilbratt, G. L., Riedinger, J. R., Passvogel, T., et al. 2010, A&A, 518, L1
- Robitaille, T. P., Whitney, B. A., Indebetouw, R., Wood, K., & Denzmore, P. 2006, ApJS, 167, 256
- Robitaille, T. P., Whitney, B. A., Indebetouw, R., & Wood, K. 2007, ApJS, 169, 328
- Robitaille, T. P., Meade, M. R., Babler, B. L., et al. 2008, AJ, 136, 2413
- Scargle, J. D. 1982, ApJ, 263, 835
- Siess, L., Dufour, E., & Forestini, M. 2000, A&A, 358, 593
- Schuller, F., Menten, K. M., Contreras, Y., et al. 2009, A&A, 504, 415
- Shu, F. H. 1977, ApJ, 214, 488
- Smith, L. C., Lucas, P. W., Kurtev, R., et al. 2018, MNRAS, 474, 1826
- Sokolovsky, K. V., Gavras, P., Karampelas, A., et al. 2017, MNRAS, 464, 274
- Takami, M., Chen, H.-H., Karr, J. L., et al. 2012, ApJ, 748, 8
- Upton, G.; Cook, I. 1996, Understanding Statistics, Oxford University Press. p. 55. ISBN 0-19-914391-9.
- Urquhart, J. S., Moore, T. J. T., Schuller, F., et al. 2013, MNRAS, 431, 1752
- Urquhart, J. S., Moore, T. J. T., Csengeri, T., et al. 2014, MNRAS, 443, 1555
- Urquhart, J. S., Csengeri, T., Wyrowski, F., et al. 2014, A&A, 568, A41
- Urquhart, J. S., K”onig, C., Giannetti, A., et al. 2018, MNRAS, 473, 1059
- VanderPlas, J. T. 2017, arXiv:1703.09824

- Vorobyov, E. I., & Basu, S. 2006, ApJ, 650, 956
Vorobyov, E. I., & Basu, S. 2008, ApJ, 676, L139
Vorobyov, E. I., & Basu, S. 2015, ApJ, 805, 115
Wenger, M., Ochsenbein, F., Egret, D., et al. 2000, A&AS, 143, 9
Wienen, M., Wyrowski, F., Menten, K. M., et al. 2015, A&A, 579, A91
Zapata, L. A., Leurini, S., Menten, K. M., et al. 2008, AJ, 136, 1455
Zhu, Z., Hartmann, L., & Gammie, C. 2009, ApJ, 694, 1045

SOURCE	χ^2	Av mag	M M_\odot	\dot{M} $\log(M_\odot \text{yr}^{-1})$	\dot{M}_{disk} $\log(M_\odot)$	\dot{M}_{disk} $\log(M_\odot \text{yr}^{-1})$	$\log(L_\odot)$	Age $\log(\text{yr})$
MG303.9304-00.6879	11.69 ± 3.10	2.7 ± 4.6	10.3 ± 2.1	-3.5 ± -3.35	-0.86 ± -0.75	-5.33 ± -4.89	3.84 ± 3.78	5.0 ± 0.4
MG328.0494-00.0487	9.53 ± 5.06	38.23 ± 5.49	5.58 ± 0.94	-5.89 ± -5.28	-1.61 ± -1.40	-6.25 ± -5.46	2.91 ± 2.73	5.94 ± 0.42
MG352.2452-00.0636	7.97 ± 2.81	26.17 ± 16.92	1.84 ± 1.32	-4.53 ± -4.37	-1.60 ± -1.40	-5.76 ± -5.36	1.76 ± 2.10	4.21 ± 0.71
MG354.4384+00.4185	6.33 ± 3.51	14.70 ± 14.42	3.65 ± 1.03	-4.15 ± -4.33	-1.40 ± -1.23	-6.13 ± -5.77	2.06 ± 1.70	4.63 ± 0.38
G309.91+0.32	38.03 ± 2.33	0.00 ± 0.02	5.39 ± 0.78	-3.84 ± -3.57	-1.55 ± -1.29	-6.60 ± -6.26	2.36 ± 2.00	4.78 ± 0.35
G335.59-0.29	33.02 ± 2.66	0.07 ± 0.16	8.53 ± 0.66	-3.34 ± -3.07	-0.88 ± -0.66	-5.66 ± -5.61	3.15 ± 2.76	4.53 ± 0.33
G351.78-0.54	15.36 ± 3.21	38.3 ± 8.8	8.8 ± 0.9	-3.28 ± -3.35	-1.08 ± -0.76	-5.88 ± -5.60	3.47 ± 3.16	4.9 ± 0.3
G343.50-0.47	9.15 ± 3.97	34.8 ± 11.6	6.6 ± 0.4	-3.46 ± -3.72	-1.06 ± -0.98	-5.81 ± -5.42	2.61 ± 2.15	4.9 ± 0.4

Table 7. Best fit parameters for the SEDs of example targets.

Appendix A: Tables

Table A.1. Input data to build the SEDs.

Source	J (mJy)	H (mJy)	K _s (mJy)	[3.6] (mJy)	[4.5] (mJy)	[5.8] (mJy)	[8.0] (mJy)	[24] (mJy)	70 (mJy)	160 (mJy)	250 (mJy)	350 (mJy)	500 (mJy)	870 (mJy)
MG002.5577-00.7510														
MG003.5016-00.2020														
MG006.2185-00.5837	7.18	121.61	224.36	367.37	551.90	3801.94	29697.80	28396.90	26346	53000	45976	11381.30	22095	4330
MG006.9222-00.2512	0.86	7.18	20.80	90.98	232.43	329.81	882.17	12654.10	38301.50	53000	45976	8180	4330	
MG300.3241-00.1985														
MG303.9304-00.6879														
MG305.5101+00.3661	1.82	9.52	22.56	38.40	42.64	162.77	2739.57	138174	185408	128313	85812	11380	128313	6680
MG306.1352+00.1330														
MG306.5029+00.0731	0.79	7.53	42.01	83.36	115.11	147.32	522.71	2430.10	6373.91	13913	2290	2290	2290	5290
MG313.2760-00.7111														
MG317.4777-00.3504	1.71	32.79	66.09	144.51	182.58	707.45	427.45	4786.08	9590.67	15964	2110	2110	2110	2110
MG317.5959+00.0527	1.26	26.24	72.34	148.42	198.18	701.04	1180.58	32078.80	45655	18946	1210	1210	1210	1210
MG322.4833+00.6447														
MG326.7241+00.3552														
MG326.9250-00.5141														
MG328.0494-00.0487	1.54	13.48	155.94	285.59	435.61	464.15	2018.76	24265.20	35206.80	39668	3590	3590	3590	3660
MG328.6141-00.4657														
MG331.5722-00.2290	26.30	236.46	565.65	813.39	827.68	1396.53	22.20	209.66	22135.10	26652	3310	3310	3310	4110
MG331.8302+00.0360														
MG332.1534+00.0069														
MG332.1990+00.5957														
MG332.3652+00.6046	2.13	32.22	93.19	178.77	198.73	1093.67	13.84	11.19	76936	43824	26921	9120	9120	3080
MG332.6662+00.0271														
MG333.0294-00.0149														
MG333.2025+00.2940														
MG335.2667-00.0151														
MG335.6100-00.7866														
MG335.61172-00.2001														
MG336.8585-00.1903	1.08	2.35	8.55	14.92	29.81	20.89	9.23	292.04	27811.20	41602.20	25085	5120	5120	3440
MG337.9402-00.5325	2.95	1.37	6.80	26.80	64.47	69.74	9.06	2.97	305.47	12080.60	21664.80	28060	15920	15920
MG338.6328+00.0265														
MG338.8438+00.4342														
MG338.8762+00.5561														
MG339.2939+00.1387														
MG339.4040-00.4134	3.63	13.90	47.62	98.97	189.44	951.68	6469.26	14827.40	10345	111306	54780	16130	16130	10830
MG339.5843-00.1282	6.69	1.75	6.90	101.05	144.51	124.01	4038.26	121413	266369	223023	10345	12081	12081	1680
MG342.0988+00.8086														
MG342.3189+00.5876														
MG343.3567-00.4032														
MG343.4049-00.4007														
MG345.0737-00.1953	1.39	11.71	16.21	22.18	20.98	8.27	153.58	928.84	9710.23	14944	15671	6669	1880	22130
MG345.2198-00.1367														

(To be continued)

Table A.1 (continued)

Source	J	H	K _s	[3.6] (mJy)	[4.5] (mJy)	[5.8] (mJy)	[8.0] (mJy)	[24] (mJy)	70 (mJy)	160 (mJy)	250 (mJy)	350 (mJy)	500 (mJy)	870 (mJy)		
MG345.5764-00.2252				4.99	9.69	13.19	9.69	18.08	2030.97	10244.90	30095			4300		
MG347.0800-00.3962				20.18	44.44	33.32	13.66	3413.21	87651.20	113690				4920		
MG347.7561+00.2323				11.08	22.05	37.73	36.36	71.83	2794.66		35983	26694	6030	18940		
MG351.8098+00.6433				61.23	213.67	451.13	397.25	662.58	10945.60	45516.50	81681	44269	26694	2790		
MG351.8655-00.2246				3.18	6.04	9.03	6.78	317.35	6178.35	7583.99	19341			2630		
MG352.0746-00.3874				1.12	3.84	5.69		90.56	6307.34	15580.70				19410		
MG352.2452-00.0636				8.36	31.96	54.99	51.27	642.38	27139.10	25412.50	50847	41630	8720	16150		
MG352.6040-00.2253				1.58	6	13.12	9	310.34	12433.80	31817.30	54283	63917	28484	33570		
MG353.3418-00.2890				3.88	9.34	30.41	25.56	26.83	2732.81	9306.65	16015.40	36109	24237	13391	4680	
MG354.4384+00.4185															1800	
MG354.6995+00.5229															7550	
MG356.5212+00.2141															28970	
MG357.5328+00.2366																
MG358.0590-00.4698																
MG358.4604-00.3929																
G9.83-1.05				1.43	1.80	1.12	12.30	19.50	25.30	22.70	220.10					
G9.81-1.06							6.10	25.90	18.50	15.20					9159	
G9.62+0.20							84.30	322.90	675.20	1083.40						
G8.73-0.37				1.27	3.05	3.14	4.20	14.50	20.60	14.40	707.40	26093.90	21879.10			
G8.72-0.36				0.51	1.17	3	11.90	27.90	25.50	13.70	934.70	17224.10	26429.70			
G8.70-0.37				3.01	8.09	10.04	8.80	28.90	46.20	38.60	478.10	9620.31	42757			
G8.66-0.37				0.45	1.74	8.96	155.20	486.80	784.20	775.90	4595.60	53153.30	61003.30	37794		
G8.27+0.51				2.14	3.24	3.74	12.70	42.70	80.80	75.30	640	25575.10	47433.20	38677	1320	
G6.19-0.36				28.53	60.13	23.63	44.40	139.10	159.50	96.60	7064.80	573327	657804	470913	27050	
G5.88-1				0.35	1.30	2.76	9.70	20.70	23	12.60	426.20	18341.40	24488.90	21423	5300	
G5.62-0.08				2.75	3.69	0.45	1.90	8.20	10.90	1.20	48.40			43526		
G4.89-0.13				1.70	1.79	2.69	11.70	36.30	45	29.70	870.60	27668.30	47441.80	40298		
G4.83+0.23				0.71	3.27	12.10	226.80	523.40	770.32	897.10		435407	360055	200859	10600	
G4.63-0.67				3.14	8.97	0.26	10.80	20.40	22.40	18.20	140.10	415.46	10826.50	17460	4180	
G359.44-0.10				2.17	2.68	1.43	64.60	250	370.30	229.10		7361.54	1064810		118900	
G358.84-0.74							16.70	29.50	39.20	51.90	1353.60	36006	88604.40	43699	9410	
G358.46-0.39(b)							0.44	5.40	16.50	23.90	5.50	142.50	127315	400983	332122	236659
G358.39-0.48							1.79	163.70	432.60	872.70	1570.50	1366660	853627	433860	104546	28970
G358.26-2.06				0.83	2.84	22.26	136	298.20	346.60	269						
G357.52+0.20							0.81	45.80	109.90	184.90	198.70	15066	36280.70	42341	35965	24403
G356.37+0.57							21.20	83.70	92	48.40	2918.90	119546	142002	94839	54368	5290
G355.75-0.87				9.61	7.73	5.48	12.30	21.90	29.30	27.30	54.70	383.61	3613.48	5072	9498	
G355.75+0.65								29	35.10	20.10						
G355.54-0.10				0.74	4.13	7.34	78.90	176.60	298.70	409.70		298411	218012	102269	52536	5420
G355.41+0.10							0.93	19.80	60.80	87.40	58.10	344.70	55819.70	76051		
G355.24+0.37												684.90	27503.40	41150.10		
G355.19-0.08				1.40	1.85	0.74	23.50	37.20	47.60	33.60	44					
G355.18-0.42				1.75	2.46	3.07	22.40	114.60	171.70	145.60	1781.40	57761.10	203153	210207	116253	79554

(To be continued)

Table A.1 (continued)

Source	J	H	K _s	[3.6] (mJy)	[4.5] (mJy)	[5.8] (mJy)	[8.0] (mJy)	[24] (mJy)	70 (mJy)	160 (mJy)	250 (mJy)	350 (mJy)	500 (mJy)	870 (mJy)
G354.78+0.83			0.85	22.60	35.40	43.80	51.40	220.40	3511.06	10507.40	14413			
G354.71+0.29	0.99	2.88	6.21	10	19.90	31.10	36.80							15290
G353.58+0.66	0.08	0.15	2.45	36.40	92.20	125.20	925.50	12030.50	77682.70	76820	41035	23248	11470	
G353.46+0.56	0.30	1.10	7.05	78.30	213.10	205.30	155.70	318940	380847					11050
G353.40-0.07	0.56	0.88	1.61	17.10	50.50	58.50	58.70	82.30		2612.60				
G352.63-1.07	0.10	1.52	1	1268.20	3762.40	7861.60	8920.50		249	1281730				
G352.61-0.23	0.14	0.27	0.77	26.20	49.40	56.70	101.20			12433.80	31817.30	54283	63917	23433
G352.60-0.19	2.03	2.81	3.68	14.10	31.50	32.70	27.20			30949.50	53028.60			41328
G352.58-0.18	0.25	0.98	2.54	15.20	32.30	80.30	155.80			232010	194616	115440		
G352.52+0.77				9.70	20	27.90	26.80	159.10		1541.10	22437.80	22098.60		
G352.52+0.76	0.06	0.41	0.46	30.20	51.30	51.80	42.10			1191020	916238	672597	239960	23830
G352.32-0.44	0.35	1.16	1.16	625.40	1770.80	3265.40	3339.70							
G352.13-0.94	0.32	2.52	13.80	113	365.70	468.60	452.60			266311	259550	150534		
G351.80-0.45			0.17	14.90	35.40	33	15.40			19075.90				
G351.78-0.54	5.14	5.70	6.44	232.40	721.20	936.80	910.50			9008490	6513640			
G351.76-0.54				7.80	37.70	54.10	99.60							
G351.69+0.17	1.02	2.29	0.72	39.10	62.40	111.50	151.60	2583.60		75212.60	85038.50	61160		
G351.54-0.57			0.29	29	53.50	87.70	100.70	190.90						
G351.53+0.71	0.12	0.56	1.59	18	47	77.20	90.30	262.70		2529.02				
G351.53+0.70				17.10	86.70	169.90	172.70	1065.10		11067.90				
G351.38-0.18				16.70	51.30	103.90	152.60	3520.70		49573.10	72878.40	54369	23906	2580
G351.27+1.04	0.23	0.42	1.45	6.80	32.90	73.90	53.30			1149.33				
G351.16+0.69	5.32	49.56	200.78	1433.80	4101.60	4883.70	4673.20							
G351.05-0.39				11.60	24.30	36.90	27.30	49.40		10777.90	16824	12397		
G351.02-0.86				84.50	193.10	278.70	297.60	2641.40		37877.20	51539.60	45848		
G350.75+0.68	0.15	1.76	7.27	38.30	67.20	74	73	3456.20		26490.20	21461.40	13507	8797	
G350.52-0.35	0.53	1.23	4.19	92.20	235.40	509.10	642	2062.60		48195.30				
G350.41-0.07				4.90	11.30	12.20	6.80	31.80		2044.49	21969.60	35733	28924	
G350.36-0.07				9.30	24	18.80	4.70	987.20		56118.30	61175.50	37212	18065	2190
G350.33+0.10	0.76	2.38	8.07	68.90	181.90	488.10	1370.10			832396	739052	420158	161725	
G350.02-0.52				6.80	17.60	29.50	17.80							
G349.64-1.09			0.16	114	340.30	704	923			142999	193490	167701	77680	
G349.63-1.10(b)	4.14	3.94	3.68	17.50	34.30	45.10	43.80							
G349.63-1.10(a)	0.87	2.91	13.17	41.30	75.80	79.70	60.60							
G349.62-1.11	1.71	1.77	1.76	22.20	65.70	107.60	132.10			2752.99	7217.72			
G349.62-0.20				5.30	10.20	4.10	6.90	97.10		15017.30	24005.10	19841	11182	2020
G348.58-0.92	3.36	3.89	6.10	75.90	216.80	246	154.20	5098.80		191476	214113	210360	9563	28970
G348.17+0.46				14.30	44.40	92	145.90	2432.50		61994.70	111104			12300
G347.08-0.40	0.86	4.80	12.59	51.20	100.70	101.80	51.80	2286.40		87651.20	113690			4920
G344.58-0.02				58	205.80	320	430.10	12302.60		815212	505481	224157	84320	7310
G344.21-0.62	0.26	2.49	16.75	111.50	272.80	358	320	1046.70		18201.30	50127.20			
G343.78-0.24	0.09	0.52	1.58	23.30	50.30	39.70	15.40	2315.20		52517.10	76811.70			
G343.72-0.18(a)	0.79	1.74	11.74	33.60	60.20	55.30	32.60	905.60		17776.40	36648.60	70987		6770

(To be continued)

Table A.1 (continued)

Source	J	H	K _s	[3.6] (mJy)	[4.5] (mJy)	[5.8] (mJy)	[8.0] (mJy)	[24] (mJy)	70 (mJy)	160 (mJy)	250 (mJy)	350 (mJy)	500 (mJy)	870 (mJy)
G343.53-0.51(a)				13.10	62.40	88	75	621.60	11352.90	35043.10	82844			19859
G343.50-0.47	0.17	0.67	3.85	44.40	204.90	301.20	216.70	3482.40	138502	199245	130416	63516		
G343.50+0.03	3.28	4.46	2.23	12.70	27.40	9.50	31.80	168.60	12338.80	71037.80	73215			
G343.42-0.33	0.09	0.59	4	36.80	74.60	122.40	141.90	298.70	2021.24	5060.20				
G343.40-0.40	0.21	1.71	5.67	17.30	34.50	47.60	40.20	94.40	928.84	9710.23				2260
G343.19-0.08(a)	0.52	4.41	17.80	68.40	146	169.10	193.90	3732.10	34193.70	52532.90	52951	32225	26279	6800
G343.12-0.06	0.10	0.60	1.72	196.20	875.60	1254.90	796.60	19300.20						
G342.15+0.51	0.74	0.73	1.51	6.60	12.40	15.70	16.40	70.50	1420.09					
G341.99-0.10			0.78	48.80	162	192.80	89.10	230.04	39826.60	58830.50	43078	20185	11807	2870
G341.73-0.97	1.37	1.54	0.39	73.30	213.20	295.70	230.90	1184.90	10332.70	30776.80	36353	22838	16479	
G341.24-0.27				20.80	57.60	60.60	38	1189	62165.40	173692	168839	94719		
G341.23-0.27	13.33	11.75	7.92	6.70	14.20	18.80	13.60	70.30						
G341.20-0.26	0.45	1.62	7.52	23.30	32.30	33.80	15.50	49.40	820.63					
G340.75-1	0.27	1.10	2.99	101.30	239	336.40	552.60	17376	525318	379176				
G339.95-0.54				41.70	140.30	188.40	231.60	7877	399088	435963	285295			
G337.30-0.87	0.10	0.27	9.74	228.30	536.90	1136.50	2237.20	5589	74537.20	117284	93897	46990		
G337.16-0.39	0.17	1.38	8.31	27.10	64.60	64.10	42	708.60	26979.10	74832.60	76629			
G336.96-0.98			0.18	21.80	66.60	62.10	39.20	612.70	7675.35	23705.50	33553			
G336.87+0.29	0.11	1.20	3.62	132.10	483.80	466.70	111.30	10230	820905	1197480				
G335.59-0.29			0.17	38	298.10	481.70	266.40	2380.30	128964	238070	164135	70651		19760
G335.43-0.24			0.52	8.80	23.40	24.10	8.70	201	17743.50	30110.80	23843	12333		1100
G334.25+0.07			3.84	31	101.90	171.80	218.70	2344.90	38882	83179.20	80936	43128	23568	
G334.04+0.35	1.56	1.98		44.70	215	336.70	354.90	2689.80	341385	452377	314833	46753	28034	11760
G332.94-0.69			1.90	1.03	14.50	47.40	42.50	8.40	240.20	40389.30	44024.20			4850
G332.91-0.55	1.13	2.40	5.74	63.20	182.20	178.60	180.90	3104.60	82921.10	127274	118693	76167		9360
G332.81-0.70	0.46		0.25	7.90	20.50	27.20	41.10	38.10						
G332.59+0.04(b)				3.40	8.80	4.80	6	22.40						
G332.59+0.04(a)				7.10	22	24.30	19.20	203.90	16003.50			29333	9986	1950
G332.58+0.15				20.70	51	34.60	21.10	782.40	27759.50	76661.80	114352	55331		
G332.56-0.15			0.74	5.58	149.50	420.90	1029.50	1898.50	8610.40	230815	399075			
G332.47-0.52	0.62	2.61	1.43	102.20	237.50	368.70	382.80	2216.90						
G332.36+0.60	0.12	0.42	1.79	8.10	20.40	26.90	23.70	68.30						
G332.33-0.12	0.42	0.96		9.80	29.20	24.10	14.90	551.90	11479.70	23365.30	52437	65571		
G332.28-0.07				110.80	498.70	880.50	1431.70	8092.80	3720.80	262815	480505	210021		
G331.71+0.60	0.89	2.61	6.01	122.50	315.30	421.90	395.80							
G331.71+0.58	1.81	6.78	8.84	10.70	26.50	16.60	10.60	245.50	97866.60	79785				
G331.62+0.53			0.16	47.60	117.20	233.20	444.20	2955.70						
G329.61+0.11	1.24	2.32	3.07	110.80	498.70	880.50	1431.70	8092.80	146103	128545	93253	45750		
G329.47+0.52	1.10	2.91	0.36	10.30	28.30	33.70	6.50	1167.90	19074	55495.40	49307			12230
G329.16-0.29	0.89	1.58	1.60	4.30	11.80	16	11.80	106.50	14013.10	58085	68623			4660
G329.07-0.31(b)	0.26	1.01	2.10	57.50	322.80	795.30	1054.10	6590.20	189204	271610				21390
G329.07-0.31(a)	0.79	2.81	8.15	79.80	277.90	423.40	424.40	4192.30	48243.90	42766.10				
G328.55+0.27	0.61	2.18	85.10	268.80	368.40	318.40	4483.80	91578.90	108836	73712	33341			4100

(To be continued)

Table A.1 (continued)

Source	J	H	K _s	[3.6] (mJy)	[4.5] (mJy)	[5.8] (mJy)	[8.0] (mJy)	[24] (mJy)	70 (mJy)	160 (mJy)	250 (mJy)	350 (mJy)	500 (mJy)	870 (mJy)
G328.14-0.43	0.81	3.89	1.59	64.90	146.90	127.80	23.80	2567.30	156612	153688	98685	43607	7740	
G327.89+0.15				10.90	38.60	57.90	43.40	215	26982.10	114346			18650	
G327.40+0.44	0.47	1.45	7.32	235.60	876.70	1964.70	2829.90	11960	1355290	1458480	931407	405404	164013	
G327.39+0.20	0.11	1.79	5.27	67.50	196.50	259.90	242.40	3322	160711	318233	238756		11510	
G327.30-0.58				24.50	158.80	341.80	364.90	2589.10						
G327.12+0.51	0.39	1.45	15.95	365.30	964.50	2544.50	4347.80	19185.40	1235030	699293	378517	148699		
G326.86-0.67	1.68	2.10	0.77	13	35.80	62.80	13.60	130.90	53020	153152				
G326.80+0.51				3.70	10.20	5.80	6.70	10	5629.10	25416	15808		1850	
G326.79+0.38	0.08	1.77	5.79	171	305	348.50	289.10	3762.90	185328	195318	144049			
G326.78-0.24	1.36	4.73	27.36	207.50	614.10	1085.60	1415.10	9509.50	220717	270607	221148	94074	41749	11380
G326.65+0.75	1.83	2.13	2.62	40.50	196.80	300.30	218.20	2110.80	56757.40	138162	129254	71528		14420
G326.61+0.80(c)	0.81	4.41	24.95	92.70	162.40	174.20	150.10	1816.60	75746.90	148005	138633			
G326.61+0.80(a)				20.20	72.90	115.60	181.70	2248.10	17708.30					
G326.57+0.20	0.78	1.27	1.30	4.40	17.90	25.30	16.80	273.40	37308.40	71863.20	56154	30573		2550
G326.41+0.93	0.25	0.76	2.37	75.70	323.60	468.20	333.40	2551.90	26244.60	266730				
G326.31+0.90	1.20	2.25	4.32	13.50	27.20	36	45.30	68.20	3146.64	9805.79				
G326.27-0.49	0.23	2.07	8.53	147.40	494.50	921.60	784.50	3139.60	80752.10	110188	103871	51766		
G324.19+0.41	0.78	1.15	1.11	25.90	32.20	53	53.70	207	6383.07	61591			9580	
G324.11+0.44	0.14	0.69	4.47	58.90	185.20	207.40	171.30	1537.60	31313.30	56805	58135	31873	26089	6720
G321.94-0.01				18.90	98.30	190.80	173.50	4416.10	262577	497694	382409	204002		
G317.88-0.25	0.12	0.83	3.11	11.40	22.10	19.40	19	17.50	4560.06					
G317.87-0.15	0.75	0.96	5.18	6.40	13.10	10.50	8	192.80						
G311.51-0.45	0.99	6.05	3.12	397.10	776	1183.60	1507.70	10139.10	135574	206411	169100	85755	38615	
G309.91+0.32	0.13	2.25	2.32	61.10	129.40	96.70	20.50	581	55899.60	128136				
G305.89+0.02	0.48	1.99	3.49	36.70	120.40	166.40	158.50	3639	275832	407079	286688	130168		11530
G305.82-0.11	0.36	1.08	2.47	15.60	57.50	64.60	50	1062.20	62390.10	153978	184650	86395	47327	8580
G305.62-0.34	3.86	8.96	10.83	15.40	27.10	27.20	19	1082.80	93516.80	103582	64909	27575	11432	1610
G305.57-0.34	1.21	1.42	0.22	20.30	35.90	25	13.30	343.90	17240.10	38088.40	35193	21266		1660
G305.52+0.76	1.05	0.86	1.39	20.70	48.70	55.80	22.80	645.60	20379.90	58633.40	58722	33322		5530
G305.48-0.10	0.39	1.52	11.80	107.80	275.40	358.50	304.10	5052.20	216991	226933	164303	78750		9030
G304.89+0.64	0.92	3.78	1.98	45.70	102.90	165.80	175.10	7645.70	187379	159050	95644	45167	21200	5530
G298.90+0.36	6.80	10.34	12.27	71.70	125.70	160.10	162	3293.10	37075.20	38671.10	23151	25449	12633	
G298.26+0.74	0.21	1.16	24.93	317.10	605.60	648.80	536.30	18226.20		208740	71223	29343		7660
G2.54+0.20	0.07	0.19	5.51	180	365.60	320.70	172	2761.20		62062.30				
G2.14+0.01	0.39	1.81	4.71	21.50	65.80	196.50	310.10	307960	291775	159452	70365	26188		5740
G0.09-0.66			1.88	20.50	76.90	67	19.50	325.30	115667	314354		69898		

Table A.2. Results of the weighted averaging of the fit SEDs.

SOURCE	χ^2	σ_{χ^2}	Av	σ_{Av}	M	σ_M	M	$\log(M_{\odot} \text{yr}^{-1})$	σ_M	M_{disk}	$\log(M_{\odot})$	$\sigma_{M_{disk}}$	\dot{M}_{disk}	$\log(\dot{M}_{\odot} \text{yr}^{-1})$	$\sigma_{\dot{M}_{disk}}$	L	σ_L	Age	σ_{Age}
MG358.0590-00.4698	6.98	3.21	12.18	16.83	2.14	1.83	-5.40	-5.67	-1.58	-5.63	-5.35	1.91	2.13	4.62	0.95				
MG356.5212+00.2141	10.40	2.95	42.94	11.85	3.20	1.69	-6.83	-6.41	-3.54	-8.75	2.31	2.35	5.98	0.27					
MG354.4384+00.4185	7.45	3.72	8.38	9.13	7.87	0.91	-3.96	-4.24	-1.00	-0.74	-5.30	-4.86	2.93	2.58	4.31	0.40			
MG352.6040-00.2253	8.75	4.29	39.18	8.79	7.60	0.75	-3.55	-3.70	-1.02	-0.76	-5.57	-5.26	2.91	2.43	4.53	0.45			
MG352.2452-00.0636	10.11	2.99	19.40	18.02	5.74	1.85	-3.93	-3.77	-1.08	-0.92	-	-	2.87	2.84	4.27	0.78			
MG351.8098+00.6433	10.70	3.01	47.02	6.49	1.89	1.11	-7.23	-6.61	-1.76	-1.87	-6.88	-6.73	1.61	1.84	6.45	0.43			
MG347.7561+00.2323	8.34	3.14	44.67	8.74	6.53	0.76	-4.78	-3.77	-1.48	-1.46	-6.15	-5.79	3.15	2.76	6.31	0.38			
MG345.5764-00.2252	12.24	2.98	38.91	7.03	4.40	0.53	-5.76	-4.63	-1.40	-1.42	-6.24	-5.62	2.53	2.06	6.42	0.36			
MG345.4049-00.4007	8.12	3.22	43.87	10.90	3.19	1.04	-6.99	-6.39	-1.37	-1.37	-6.15	-5.72	2.10	2.45	6.13	0.49			
MG343.3567-00.4032	7.19	3.43	29.62	18.85	2.65	2.31	-5.21	-4.93	-1.64	-1.64	-4.95	-4.85	2.44	2.49	4.68	1.61			
MG342.3189+00.5876	14.89	3.54	36.44	13.72	1.50	1.46	-5.03	-5.23	-1.46	-1.39	-5.21	-5.18	2.05	2.41	3.92	1.04			
MG339.5843-00.1282	7.95	4.27	19.49	9.74	5.03	1.30	-4.03	-3.91	-1.23	-0.99	-6.16	-5.82	2.34	2.15	4.66	0.44			
MG339.4040-00.4134	7.38	3.39	41.03	11.66	2.89	2.00	-4.82	-4.85	-1.41	-1.25	-5.16	-4.92	2.52	2.75	4.24	1.12			
MG339.2939+00.1387	4.68	2.59	19.03	11.42	4.25	1.45	-3.38	-3.46	-1.98	-1.39	-6.60	-5.59	2.27	2.24	4.63	0.49			
MG338.8762+00.5561	8.49	3.07	42.83	12.32	4.49	0.93	-4.33	-3.78	-1.53	-1.40	-5.97	-5.24	2.55	2.19	5.95	0.91			
MG338.8438+00.4342	13.24	2.88	32.91	14.51	7.08	2.80	-4.70	-4.54	-0.84	-0.90	-4.61	-4.29	3.49	3.58	5.03	1.30			
MG337.9402-00.5325	10.45	3.44	20.44	8.10	3.75	1.62	-6.20	-6.04	-1.75	-1.50	-5.75	-5.38	2.31	2.18	5.74	1.10			
MG336.8585-00.1903	16.51	5.28	7.85	4.46	2.75	1.00	-4.13	-3.88	-1.26	-1.26	-6.12	-5.67	1.91	1.56	5.56	1.28			
MG335.6172-00.2001	19.97	3.46	18.22	6.90	5.87	1.50	-	-	-1.45	-1.53	-6.37	-5.75	3.09	3.22	6.61	0.19			
MG335.6100-00.7866	3.83	2.75	30.28	13.84	4.42	2.17	-4.66	-4.77	-1.42	-1.14	-5.05	-4.68	2.49	2.30	4.16	0.99			
MG335.2667-00.0151	10.55	2.89	40.15	14.44	3.94	2.03	-6.47	-6.09	-1.53	-1.74	-5.66	-5.51	2.66	2.67	5.88	1.24			
MG333.2025+00.2940	31.24	3.34	5.26	10.71	4.03	1.03	-4.06	-4.18	-1.86	-1.85	-7.30	-6.95	2.01	1.64	4.92	0.36			
MG333.0294-00.0149	17.35	2.93	22.88	14.51	5.02	1.06	-3.90	-3.86	-1.26	-1.09	-6.31	-5.96	2.28	1.94	4.80	0.36			
MG332.6662+00.0271	8.80	4.05	43.34	9.80	3.40	0.74	-4.90	-4.22	-1.63	-1.50	-6.42	-5.79	2.11	1.93	6.35	0.77			
MG332.3652+00.6046	11.46	5.02	27.31	12.65	2.27	2.09	-4.52	-4.30	-1.44	-1.30	-5.16	-4.97	2.15	2.28	3.90	0.96			
MG332.1990+00.5957	11.72	3.11	5.92	5.79	1.91	0.84	-6.38	-5.87	-2.13	-1.87	-7.60	-7.08	1.02	1.03	5.96	0.34			
MG332.1534+00.0069	3.94	2.74	20.62	12.65	1.15	0.86	-4.54	-4.39	-2.33	-1.87	-7.17	-6.23	1.10	1.24	4.95	0.49			
MG331.8302+00.0360	8.61	4.14	37.35	12.55	3.81	1.02	-4.05	-3.71	-1.65	-1.47	-6.16	-5.67	2.40	2.43	5.89	1.25			
MG331.5722-00.2290	5.70	3.31	38.81	4.88	7.59	0.99	-	-	-1.35	-1.33	-5.85	-5.56	3.41	3.13	6.34	0.18			
MG328.6141-00.4657	8.45	2.76	44.71	9.40	1.59	0.90	-6.80	-6.54	-1.87	-1.78	-6.75	-6.51	1.17	1.48	6.02	0.49			
MG328.0494-00.0487	10.79	4.66	35.69	5.97	6.20	0.81	-5.01	-4.36	-1.52	-1.31	-6.12	-5.34	3.07	2.61	5.88	0.41			
MG326.7241+00.3552	8.40	3.61	25.18	18.68	1.13	1.22	-6.33	-6.35	-2.08	-1.95	-6.48	-6.55	1.40	1.61	4.78	1.59			
MG322.4833+00.6447	7.79	4.18	43.27	8.71	1.97	0.99	-5.30	-4.76	-1.85	-1.65	-7.27	-6.86	1.17	1.10	5.67	0.39			
MG317.5959+00.0527	15.75	4.56	31.64	10.72	4.97	1.34	-	-	-1.80	-1.73	-7.12	-6.94	2.81	2.75	6.50	0.28			
MG317.4777-00.3504	12.50	4.48	32.43	11.45	6.44	1.95	-4.55	-4.42	-0.98	-0.88	-	-	3.24	3.07	4.80	1.21			
MG313.2760-00.7111	6.20	3.11	32.70	14.23	0.90	-4.63	-4.53	-1.54	-1.45	-5.35	-5.20	1.74	2.01	3.74	0.53				
MG306.5029+00.0731	11.45	4.04	30.19	7.75	3.75	1.11	-6.69	-6.32	-1.94	-1.76	-6.39	-5.77	2.32	2.64	6.26	0.76			
MG305.5101+00.3661	7.49	3.06	40.01	16.52	3.54	1.74	-5.75	-5.27	-1.58	-1.52	-5.64	-5.27	2.33	2.19	5.65	1.34			
MG303.9304-00.6879	11.69	3.10	2.72	4.57	10.29	2.05	-3.49	-3.35	-0.86	-0.75	-5.33	-4.88	3.84	3.78	5.01	0.42			
MG300.3241-00.1985	17.08	5.65	25.43	6.92	5.88	1.28	-6.58	-5.75	-1.35	-1.31	-6.01	-5.30	3.05	3.16	6.16	0.49			
MG006.9222-00.2512	13.50	3.20	49.50	1.55	6.15	1.49	-6.96	-6.32	-1.37	-1.54	-5.84	-5.00	3.12	2.98	6.31	0.52			
G8.27+0.51	20.85	5.72	0.62	0.73	1.16	0.23	-4.49	-4.60	-2.30	-2.12	-5.82	-5.57	1.50	0.84	3.65	0.21			
G354.78+0.83	5.82	3.63	26.15	9.37	4.66	0.68	-5.04	-4.80	-1.47	-1.39	-6.22	-5.81	2.35	2.07	5.61	0.60			
G354.71+0.29	13.33	3.52	4.85	5.21	7.56	2.38	-3.59	-3.17	-1.05	-0.85	-	-	3.22	3.31	4.59	0.67			
G353.58+0.66	9.88	4.65	37.77	6.28	0.91	1.25	-6.09	-6.28	-2.44	-2.03	-7.79	-7.44	1.56	2.02	5.32	0.61			
G352.60-0.19	9.03	2.43	14.89	9.81	6.67	1.40	-3.78	-3.36	-1.18	-0.95	-5.66	-5.13	2.85	2.67	5.03	0.95			

(To be continued)

Table A.2 (continued)

SOURCE	χ^2	σ_{χ^2}	Av	σ_{Av}	M	σ_M	\dot{M}	$\sigma_{\dot{M}}$	M_{disk}	$\sigma_{M_{disk}}$	\dot{M}_{disk}	$\log(M_{\odot} \text{yr}^{-1})$	$\sigma_{\dot{M}_{disk}}$	L	σ_L	Age	σ_{Age}
G352.32-0.44	4.38	2.50	2.54	2.08	8.55	0.91	-3.36	-4.11	-2.15	-1.34	-7.15	-6.28	3.69	3.06	5.21	0.12	
G350.41-0.07	14.21	2.91	39.58	12.41	2.67	1.05	-4.70	-4.37	-1.80	-1.63	-6.91	-6.51	1.49	1.04	5.33	0.26	
G350.33+0.10	16.04	3.93	10.38	6.32	19.56	4.65	-3.31	-2.95	-1.13	-0.79	-	-	4.57	4.33	4.36	0.73	
G350.02-0.52	4.97	2.31	22.62	12.00	6.87	2.24	-3.59	-3.56	-1.18	-0.90	-	-	2.97	3.00	4.66	0.38	
G349.64-1.09	3.63	2.73	16.73	7.73	8.30	1.86	-3.99	-4.03	-0.95	-0.84	-	-	3.13	2.89	3.82	0.44	
G349.62-0.20	6.70	3.27	12.60	7.98	2.92	1.41	-5.03	-4.55	-2.30	-1.97	-7.65	-7.12	2.01	1.94	5.77	0.87	
G344.21-0.62	17.19	2.97	28.98	6.62	4.16	0.79	-4.52	-4.33	-1.22	-1.04	-6.67	-6.41	2.11	1.75	5.61	0.60	
G343.78-0.24	4.76	2.92	1.55	4.43	3.91	0.83	-4.12	-4.63	-1.93	-1.50	-7.20	-6.58	1.87	1.89	5.26	0.20	
G343.53-0.51(a)	9.01	2.94	20.92	17.04	1.03	0.94	-4.85	-4.78	-1.78	-1.59	-5.58	-5.32	1.40	1.58	3.72	0.67	
G343.50+0.03	6.73	3.49	6.73	4.20	2.09	0.53	-5.52	-5.03	-1.55	-1.53	-7.46	-7.13	1.11	1.07	5.81	0.43	
G343.42-0.33	13.29	4.41	34.89	5.75	3.24	0.56	-7.72	-7.34	-2.17	-2.01	-7.59	-7.10	1.77	1.24	6.35	0.39	
G343.19-0.08(a)	14.53	4.56	16.87	8.03	2.66	1.06	-4.40	-4.24	-1.44	-1.31	-5.94	-5.70	1.84	1.81	4.69	0.47	
G342.15+0.51	18.15	3.75	7.74	3.33	5.44	0.65	-4.67	-4.37	-1.63	-1.68	-6.54	-5.95	2.53	2.53	5.43	0.51	
G341.73-0.97	12.27	2.73	34.65	20.10	3.51	1.92	-5.50	-5.46	-1.80	-1.72	-5.62	-5.22	2.26	2.11	5.15	1.25	
G340.75-1.00	14.63	4.56	36.03	9.71	6.16	0.98	-4.06	-4.10	-1.16	-0.94	-5.88	-5.50	2.66	2.55	4.52	0.64	
G336.87+0.29	12.60	3.35	38.96	13.03	6.17	0.94	-4.61	-4.46	-1.07	-0.99	-6.01	-5.83	2.68	2.40	5.14	0.44	
G335.59-0.29	33.02	2.66	0.07	0.16	8.53	0.66	-3.34	-3.07	-0.88	-0.66	-5.66	-5.61	3.15	2.76	4.53	0.33	
G334.25+0.07	38.21	3.56	13.63	12.14	7.44	0.42	-3.24	-3.19	-0.55	-0.69	-5.46	-5.52	2.78	2.26	5.15	1.25	
G334.04+0.35	9.88	4.22	11.94	11.52	3.00	1.22	-4.47	-4.31	-1.27	-1.12	-5.30	-5.12	2.17	1.92	3.80	0.50	
G332.9-0.55	5.54	2.63	2.09	4.51	2.72	1.15	-4.43	-4.18	-2.03	-1.77	-7.48	-6.94	1.63	1.39	5.28	0.40	
G332.59+0.04(b)	5.84	3.67	33.01	5.48	4.12	0.33	-6.08	-4.78	-1.64	-1.54	-6.28	-5.75	2.41	2.10	6.78	0.25	
G332.47-0.52	9.85	2.88	22.13	11.90	6.83	1.48	-3.21	-3.21	-1.03	-0.87	-	-	3.05	3.10	4.07	0.81	
G332.33-0.12	14.25	3.42	25.82	8.78	2.63	1.01	-4.49	-4.17	-1.45	-1.34	-6.52	-6.52	1.61	1.33	5.40	0.71	
G332.28-0.07	8.25	3.10	15.49	11.58	3.85	1.09	-4.20	-4.07	-1.49	-1.23	-6.40	-6.01	2.04	1.66	4.79	0.36	
G331.71+0.58	15.59	3.39	7.64	7.48	7.36	0.59	-3.63	-3.44	-0.54	-0.56	-5.49	-5.29	2.77	2.22	6.67	0.41	
G331.62+0.53	4.87	3.70	15.93	12.23	3.48	1.31	-3.41	-3.29	-1.01	-0.94	-4.98	-4.86	2.32	2.09	3.75	0.49	
G329.47+0.52	8.72	3.93	0.00	0.00	6.14	0.94	-4.16	-4.16	-0.98	-0.79	-6.95	-6.73	2.07	1.67	4.79	0.20	
G329.16-0.29	11.76	4.66	0.95	1.19	2.53	1.23	-3.77	-3.68	-1.50	-1.45	-6.71	-6.46	1.67	1.46	4.93	0.45	
G328.55+0.27	12.09	4.34	14.66	11.68	6.09	1.21	-3.77	-3.51	-1.19	-0.91	-	-	2.65	2.31	4.16	0.52	
G326.80+0.51	5.68	3.27	25.36	11.00	1.56	0.59	-6.30	-5.65	-2.13	-1.83	-7.65	-7.22	0.80	1.06	5.90	0.32	
G326.78-0.24	13.87	4.46	21.18	5.51	5.67	1.32	-3.84	-3.59	-1.10	-0.96	-	-	2.72	2.34	3.85	0.60	
G326.65+0.75	85.82	5.93	0.75	0.97	1.57	0.95	-4.61	-4.64	-1.51	-1.44	-5.75	-5.71	1.67	1.44	3.75	0.51	
G326.57+0.20	20.91	6.23	1.22	1.11	4.32	1.51	-3.41	-3.37	-1.09	-1.01	-5.43	-4.97	2.27	2.10	4.61	0.35	
G326.41+0.93	16.41	3.14	14.72	14.47	1.67	1.58	-4.81	-4.85	-1.61	-1.48	-5.25	-5.09	1.99	1.99	2.22	0.85	
G326.31+0.90	8.95	4.07	27.21	4.79	2.58	0.88	-6.09	-5.25	-1.89	-1.72	-6.86	-6.67	1.24	1.24	5.82	0.36	
G326.27-0.49	11.61	4.00	19.88	5.46	2.04	1.69	-4.46	-4.23	-1.55	-1.51	-4.33	-4.33	2.07	1.94	6.20	0.43	
G324.19+0.41	12.56	2.69	8.41	6.53	3.58	0.72	-4.42	-4.25	-1.44	-1.49	-6.69	-6.52	1.77	1.77	5.24	0.25	
G324.11+0.44	10.90	3.41	41.90	8.39	6.07	0.83	-4.39	-3.98	-1.35	-1.15	-5.98	-5.47	2.83	2.47	5.49	0.43	
G321.94-0.01	7.83	2.98	21.70	14.56	4.11	1.43	-3.72	-3.43	-1.16	-1.05	-5.46	-5.10	2.30	2.06	4.16	0.46	
G317.88-0.25	8.26	4.17	29.00	3.80	2.34	0.62	-6.59	-6.14	-1.93	-1.83	-7.38	-6.93	1.15	1.15	5.47	0.68	
G311.51-0.45	7.30	3.04	28.01	13.90	7.12	0.85	-4.37	-3.94	-1.43	-1.03	-	-	3.25	2.83	5.47	0.68	
G309.91+0.32	38.03	2.33	0.00	0.02	5.39	0.78	-3.84	-3.57	-1.55	-1.29	-6.60	-6.26	2.36	2.00	4.78	0.35	
G305.52+0.76	23.91	3.37	30.16	9.06	2.97	1.06	-4.29	-4.26	-1.67	-1.39	-6.96	-6.61	1.71	1.37	5.04	0.34	
MG347.0800-0.3962	3.55	2.71	24.43	12.82	6.87	1.84	-4.72	-4.31	-1.50	-1.11	-6.21	-5.74	3.27	3.27	5.60	0.49	
MG338.6328+0.0265	6.60	4.30	39.30	9.85	4.89	.87	-6.81	-6.22	-1.62	-1.47	-6.57	-5.83	2.71	2.58	6.20	0.41	
MG357.5328+0.2366	7.15	3.05	44.32	12.94	1.48	1.48	-5.98	-5.53	-1.74	-1.47	-6.04	-5.40	2.87	2.65	5.78	0.80	
MG352.0746-0.3874	3.62	2.71	29.75	14.35	9.01	4.57	-4.79	-4.57	-1.76	-1.60	-6.25	-5.84	1.45	1.90	4.27	0.75	
MG326.9250-0.5141	7.28	4.32	33.97	14.97	.50	.37	-5.25	-5.10	-1.94	-1.86	-5.44	-5.24	1.17	1.36	3.32	.31	

(To be continued)

Table A.2 (continued)

SOURCE	χ^2	σ_{χ^2}	Av	σ_{Av}	M	σ_M	\dot{M}	$\sigma_{\dot{M}}$	M_{disk}	$\sigma_{M_{disk}}$	\dot{M}_{disk}	$\log(M_{\odot} \text{yr}^{-1})$	$\sigma_{\dot{M}_{disk}}$	L	σ_L	Age	σ_{Age}
MG002.5577-00.7510	10.33	3.91	24.10	17.55	1.09	-5.76	-5.80	-1.91	-1.55	-6.32	-5.91	1.15	1.85	4.36	1		
MG345.2198-00.1367	6.45	3.67	40.61	8.65	2.03	.86	-7.12	-6.76	-1.78	-1.69	-6.63	1.50	1.86	6.30	.48		
MG351.8655-00.2246	8.30	4.31	20.83	13.17	1.56	.80	-4.68	-4.61	-1.79	-1.53	-6.85	1.30	1.09	4.96	.46		
MG345.0737-00.1953	13.01	3.67	34.08	3.81	3.92	1.40	-	-	-1.75	-1.83	-5.28	5.16	2.76	2.84	6.49	.24	
MG358.4604-00.3929	10.15	2.39	26.39	20.27	2.49	1.80	-4.23	-4.04	-1.66	-1.24	-6.47	5.69	1.82	2.03	4.94	.39	
MG342.0988+00.8086	5.58	3.37	18.97	14.94	.30	.28	-5.46	-5.65	-2.20	-2.11	-6.23	6.14	.64	.94	3.54	.49	
G327.39+0.20	17.80	4.76	39.33	7.84	.98	.31	-3.43	-3.83	-1.08	-.89	-6.04	-5.73	2.67	2.29	4.79	.32	
G327.12+0.51	15.60	4.10	39.15	7.08	5.50	1.50	-3.43	-3.21	-1.06	-1.02	-5.21	-5.01	2.68	2.52	4.08	.69	
G343.72-0.18(a)	20.07	3.75	33.11	7.44	3.02	1.06	-4.57	-4.64	-1.78	-1.47	-7.09	-6.72	1.70	1.24	5.08	.35	
G351.27+1.04	15.29	2.79	31.88	14.11	.58	.70	-5.63	-6.13	-2.04	-1.92	-6.40	-6.56	1.07	1.32	3.43	1.02	
G340.75-1	17.74	3.77	45.39	6.48	6.72	.57	-4.08	-4.27	-1.32	-.91	-6.83	-6.61	2.63	1.88	4.55	.53	
G317.87-0.15	8.91	4	22.67	9.89	1.21	.76	-4.86	-4.77	-2.46	-2.05	-7.54	-7.06	1.01	.76	5.08	.48	
G350.52-0.35	8.05	49.77	6.37	-	-	-	-1.84	-	-6.61	-	-6.61	-	3.07	-	6.22		
G358.26-2.06	6.48	3.30	33.41	13.66	5.65	1.01	-3.94	-3.76	-1.17	-1.05	-6.21	-5.91	2.46	1.98	5.10	.71	
G355.54-0.10	9.05	3.39	43.93	7.15	4.53	1.38	-4.37	-4.14	-1.31	-1.03	-5.83	-5.34	2.44	2.45	5.25	1.20	
G327.89+0.15	12.66	4.70	35.64	11.39	2.31	.97	-4.19	-4.15	-1.45	-1.28	-6.52	-6.15	1.49	1.49	5.03	.66	
G350.75+0.68	11.78	3.94	22.44	10.61	3.58	1.10	-4.53	-4.71	-1.51	-1.36	-6.46	-6.08	1.96	1.54	4.78	.37	
G336.96-0.98	9.85	3.69	29.96	11.21	2.93	1.06	-4.29	-4.19	-1.52	-1.34	-6.74	-6.42	1.72	1.39	5.04	.33	
G343.50-0.47	9.15	3.97	34.75	11.57	6.61	.45	-3.46	-3.73	-1.06	-.98	-5.81	-5.42	2.61	2.15	4.86	.37	
G351.05-0.39	19.11	3.75	45.35	9.80	2.54	.33	-4.95	-4.52	-1.76	-1.83	-7.04	-6.63	1.47	.86	6.37	.57	
G9.81-1.06	6.69	2.95	32.41	11.28	1.92	1.10	-4.51	-4.35	-1.68	-1.52	-6.66	-6.22	1.46	1.49	5.04	.62	
G359.40-0.07	8.86	4.31	46.73	4.88	.23	-	-	-	-1.56	-1.58	-7.54	-7.25	1.75	1.12	6.76	.23	
G355.75+0.65	10.17	2.52	34.22	11.29	2.71	1.49	-4.36	-4.18	-1.68	-1.47	-6.30	-5.52	1.83	2.21	5.18	.35	
G305.89+0.02	8.81	4.03	40.57	10.45	4.52	1.27	-3.75	-3.53	-1.18	-1.18	-5.94	-5.53	2.24	1.88	4.47	.40	
G326.79+0.38	12.06	5.23	37.82	13.98	6.31	.69	-3.85	-3.84	-1.15	-1.15	-5.95	-5.69	2.61	2.35	5.09	.44	
G359.44-0.10	6.65	3.41	33.87	11.40	7.46	.71	-3.41	-3.50	-8.99	-6.99	-5.68	-5.38	2.80	2.32	4.70	.34	
G343.12-0.06	12.81	4.78	36.67	7.92	8.40	.63	-3.28	-3.31	-7.5	-5.59	-5.56	-5.38	3.29	2.70	4.86	.22	
G332.81-0.70	17.41	4.11	42.45	9.30	5.49	1.20	-3.85	-4.01	-1.07	-.97	-5.98	-5.75	2.39	2.03	4.71	.39	
G305.48-0.10	10.12	4.01	37.29	11.32	5.79	.97	-3.85	-3.78	-1.10	-1.02	-5.91	-5.76	2.51	2.47	4.76	.47	
G8.66-0.37	15.85	4.28	36.45	13	3.56	2.33	-4.76	-4.43	-1.35	-1.27	-5.14	-4.97	2.50	2.45	4.61	1.19	
G327.30-0.58	7.56	4.43	23.87	12.46	1.01	1.40	-4.18	-3.53	-1.65	-1.83	-4.94	-5.05	1.78	1.94	3.51	.34	
G347.08-0.40	21.55	3.88	19.12	6.94	3.85	1.06	-4.15	-3.99	-1.76	-1.33	-6.76	-6.20	2.02	1.67	4.84	.33	
G343.40-0.40	25.42	4.77	48.97	1.36	2.66	.32	-	-	-2.56	-2.29	-7.55	-7.11	1.71	1.44	6.82	.10	
G329.07-0.31(a)	13.40	3.85	27.38	11.93	2.66	2.04	-4.89	-4.74	-1.25	-1.25	-5.14	-5.10	2.30	2.38	4.09	.95	
G351.78-0.54	15.36	3.21	38.34	8.78	.87	-	-3.28	-3.35	-1.08	-.77	-5.87	-5.60	3.47	3.16	4.93	.34	
G358.84-0.74	9.61	3.97	26.60	11.40	2.17	1.03	-4.35	-4.07	-1.89	-1.57	-7.02	-6.45	1.46	1.17	4.94	.52	
G352.52+0.77	13.34	4.29	47.06	3.77	1.66	.86	-4.86	-5.09	-1.43	-1.74	-6.49	-6.47	1.44	1.44	5.13	.46	
G355.24+0.37	10.42	3.91	10.50	6.39	1.65	1.08	-4.33	-4.24	-1.40	-1.33	-6.12	-5.87	1.45	1.29	4.59	.57	
G298.26+0.74	14.89	4.45	32.15	12.77	7.63	.52	-3.77	-3.84	-7.6	-.61	-5.89	-5.71	2.83	2.35	4.61	.34	
G339.95-0.54	10.08	4.59	43.96	6.81	6.01	.98	-3.81	-3.66	-1.08	-.98	-6.16	-5.97	2.47	1.93	4.48	.43	
G8.70-0.37	11.93	4.21	43.27	8.14	1.03	.73	-4.69	-4.81	-1.33	-1.45	-5.63	-5.66	1.30	.78	4.28	.52	
G351.16+0.69	6.88	3.54	31.25	14.08	9.28	1.44	-3.56	-3.36	-1.05	-7.8	-1.31	3.54	3.06	4.97	.61		
G326.61+0.80(a)	9.99	3.97	45.58	4.34	2.82	1.83	-5.11	-5.11	-1.69	-1.66	-5.56	-5.22	2.35	2.39	4.85	1.11	
G9.62+0.20	6.72	3.39	31.15	16.32	9.80	6.37	-3.60	-3.41	-7.3	-4.49	-5.56	4.15	4.56	4.53	.97		
G352.13-0.94	6.52	3.11	32.36	11.60	5.60	1.68	-3.81	-3.72	-1.28	-1.05	-5.63	-5.20	2.54	2.34	4.83	.95	
G8.72-0.36	29.02	3.93	32.60	4.06	2.96	.96	-4.54	-4.39	-1.85	-1.55	-7.08	-6.56	1.67	1.35	5.15	.33	
G298.90+0.36	9.49	4.61	39.88	8.17	3.76	1.13	-4.43	-4.44	-1.55	-1.42	-6.07	-5.75	2.01	1.60	4.83	.51	
G6.19-0.36	21.18	3.54	32.36	9.48	5.93	.83	-3.88	-3.93	-1.03	-.91	-6.09	-5.87	2.03	2.03	4.72	.52	

(To be continued)

Table A.2 (continued)

SOURCE	χ^2	σ_{χ^2}	Av	σ_{Av}	M	σ_M	\dot{M}	$\sigma_{\dot{M}}$	M_{disk}	$\sigma_{M_{disk}}$	\dot{M}_{disk}	$\sigma_{\dot{M}_{disk}}$	L	σ_L	Age	σ_{Age}	
			mag	mag			log(M $_{\odot}$ yr $^{-1}$)		log(M $_{\odot}$)		log(M $_{\odot}$ yr $^{-1}$)		log(L $_{\odot}$)		log(yr)		
G304.89+0.64	13.35	4.45	36.36	9.27	5.39	1.13	-3.83	-3.69	-1.06	-89	-6.36	-6.16	2.34	1.91	4.63	.33	
G349.63-1.10(a)	7.29	2.76	21.68	11.13	2.85	1.18	-4.35	-4.06	-1.48	-1.18	-6.49	-5.83	1.75	1.97	5.18	.54	
G351.02-0.86																	
G5.88-1	46.83	3.22	45.60	6.56	.94	.70	-5.40	-5.32	-2.54	-2.46	-8.67	-8.61	.57	.26	5.46	.50	
G4.83+0.23	51.97	4.07	27.15	6.25	4.02	1.08	-4.22	-4.13	-1.71	-1.40	-6.80	-6.37	2.05	1.75	4.91	.37	
G351.38-0.18	13.47	3.25	42.61	8.09	7.78	.86	-3.74	-3.85	-1.20	-1.20	-5.46	-5.16	2.97	2.65	4.43	.66	
G337.16-0.39	8.24	4.11	45.04	5.34	3.12	.96	-4.33	-4.55	-1.48	-1.23	-6.22	-5.81	1.99	1.91	4.47	.51	
G327.40+0.44	9.07	5.23	26.46	3.45	4.67	.45	-7.83	-7.39	-1.63	-1.46	-7.21	-7.12	2.59	2.15	6.57	.41	
G356.37+0.57	20.13	5.13	44	9.20	6.02	3.06	-3.42	-3.13	-1.04	-1.04	-4.49	-4.42	3.27	3.56	4.33	1.24	
G329.07-0.31(b)	12.77	3.92	32.56	5.64	3.24	.54	-7.55	-7.26	-2.09	-1.97	-7.60	-7.09	1.74	1.20	6.34	.39	
G352.58-0.18	8.46	4.64	42.56	10.73	.64	.52	-5.28	-5.62	-2.07	-2.11	-5.28	-5.49	1.48	1.99	3.27	.29	
G344.58-0.02	11.55	3.23	40.80	11.07	5.49	1.96	-4.11	-4.26	-1.13	-1.13	-8.66	-5.42	5.05	2.76	2.91	4.54	
G326.61+0.80(c)	132.72	3.89	28.39	8.60	4.12	.97	-4.25	-4.42	-2.05	-1.94	-7.18	-6.79	1.95	1.64	5.12	.16	
G305.82-0.11	26.05	3.37	.85	1.85	3.82	1.98	-3.53	-3.53	-1.16	-1.16	-9.98	-5.57	5.08	2.17	2.18	4.67	
G351.53+0.70	21.94	5.16	45.66	5.57	3.89	.99	-3.86	-4.14	-1.33	-1.33	-6.66	-6.29	1.87	1.30	5.15	.16	
G351.53+0.71	9.97	4.42	33.31	15.56	.55	.24	-5.31	-5.48	-1.90	-1.98	-5.20	-5.19	1.30	.78	3.22	.16	
G329.61+0.11	21.67	3.66	47.15	4.35	3.28	1.30	-5.89	-5.14	-1.83	-1.81	-7.42	-7.47	2.39	2.79	6.66	.35	
G349.62-1.11	66.89	2.69	47.78	3.70	1.35	.70	-4.90	-5.37	-1.31	-1.59	-5.74	-5.77	1.46	1.06	4.44	.34	
G332.58+0.15	12.30	2.86	32	15.34	1.39	1.34	-5.59	-5.68	-2.10	-2	-5.73	-5.49	1.67	1.85	4.31	1.61	
G305.62-0.34	16.06	3.31	33.51	7.75	4.41	.87	-5.10	-4.59	-1.50	-1.27	-6.42	-5.86	2.34	1.98	5.98	.61	
G332.59+0.04(a)	11.42	4.18	2.25	2.47	2.75	1.08	-4.58	-4.74	-1.74	-1.43	-7.33	-6.90	1.69	1.51	5.06	.35	
G331.71+0.60	59.75	27.03	11.73	2.93	.15	-	-	-	-2.15	-2.36	-7.53	-7.60	1.84	1.02	6.81	.13	
G4.89-0.13	26.83	3.40	36.40	3.12	2.57	.84	-5.20	-4.97	-1.66	-1.53	-7.39	-7.39	1.77	1.30	.92	5.55	
G351.76-0.54	9.77	3.78	45.65	4.22	1.66	1.28	-5.33	-4.77	-2.05	-2.05	-6.63	-7.68	1.31	1.31	1.68	.56	
G8.73-0.37	6.33	3.35	37.88	11.64	2.92	3.01	-3.93	-3.40	-1.37	-1.07	-1.07	-1.05	2.95	3.95	4.21	.86	
G348.58-0.92	9.67	3.72	21.69	8.08	2.59	1.56	-4.04	-3.88	-1.40	-1.19	-6.54	-6.15	2.10	2.72	4.73	.49	
G2.14+0.01	10.87	3.98	39.56	8.53	8.41	10.46	-2.44	-	-	-1.18	-1.10	-6.15	-5.86	2.48	2.14	4.69	.46
G9.83-1.05	88.72	8.53	10.46	-	-	-	-	-	-	-	-	-	3.48	-	3.30	-	
G355.18-0.42	64.84	6.99	44.66	2.15	2.82	2.37	-5.75	-5.71	-1.30	-1.44	-4.81	-4.77	2.43	2.32	4.99	1.77	
G341.24-0.27	3.75	25.13	13.07	3.42	1.81	-3.74	-3.67	-1.60	-1.37	-5.71	-5.32	2.06	1.81	4.27	6.60		
G348.17+0.46	13.48	3.93	27.99	14.05	.77	.45	-4.21	-3.96	-1.73	-1.51	-5.63	-5.45	1.31	1.14	3.41	.35	
G353.46+0.56	8.27	3.94	39.32	9.01	2.50	1.15	-4.30	-4.24	-1.72	-1.42	-6.01	-5.45	1.84	1.84	4.49	.57	
G355.75-0.87	6.34	3.60	37.22	9.31	5.30	.81	-4.03	-3.93	-1.44	-1.26	-6.55	-6.16	2.34	2.02	4.91	.53	
G332.94-0.69	36.02	4	46.12	3.28	3.30	1.12	-4.32	-4.54	-1.76	-1.54	-6.84	-6.43	1.80	1.31	5	.40	
G349.63-1.10(b)	5.23	3.35	34.97	10.45	2.21	.96	-4.43	-4.24	-1.71	-1.54	-6.92	-6.55	1.43	1.10	5.18	.50	
G341.23-0.27	6.36	3.46	31.30	10.28	1.37	.57	-4.33	-4.03	-1.63	-1.78	-7.10	-6.53	1.25	1.21	5.13	.26	
G358.39-0.48	3.39	2.60	13.61	14.18	8.12	4.64	-3.63	-3.44	-1.44	-1.26	-6.55	-6.16	2.34	2.02	4.91	.77	
G351.54-0.57	8.62	3.15	19.42	9.33	2.52	.92	-4.48	-4.11	-1.64	-1.58	-6.35	-5.90	1.55	1.37	5.66	1.13	
G341.99-0.10	17.65	3.01	33.03	15.07	4.66	.98	-4.18	-4.32	-1.31	-1.15	-6.40	-6.12	2.21	1.89	4.86	.38	
G352.52+0.76	6.86	3.33	9.03	9.25	2.87	.95	-4.54	-4.65	-1.73	-1.52	-6.71	-6.19	1.76	1.40	4.90	.42	
G332.36+0.60	7.73	2.87	19.22	20.27	2.85	1.99	-4.41	-4.14	-1.41	-1.35	-5.37	-5.05	2.19	2.29	4.24	1.07	
G352.63-1.07	4.69	2.62	19.66	13.72	8.82	2.80	-3.65	-3.37	-1.84	-1.64	-6.35	-5.90	1.55	1.37	5.66	1.13	
G4.63-0.67	6.37	5.15	41.28	11.34	2.82	.59	-6.30	-6.89	-2.60	-3.29	-7.31	-6.81	1.27	1.08	5.63	.54	
G351.69+0.17	7.90	3.04	13.05	12.57	3.27	1.50	-4.19	-4.03	-1.74	-1.49	-6.47	-6.10	1.89	1.69	4.75	.47	
G357.52+0.20	9.20	3.91	45.34	6.08	4.01	.83	-	-	-1.27	-1.36	-5.46	-5.34	2.63	2.50	6.41	.24	
G351.80-0.45	11.01	2.08	13.14	11.58	2.41	.97	-4.35	-4.29	-1.62	-1.38	-6.56	-6.92	1.58	1.32	5.08	.30	
G352.61-0.23	6.90	3.01	25.06	9.39	3.13	1	-4.99	-4.45	-1.51	-1.26	-6.97	-6.32	2.02	2.51	5.74	.63	
G355.19-0.08	9.88	3.31	32.97	8.42	3.22	.57	-6.09	-5.65	-1.67	-1.42	-6.98	-6.70	1.54	1.24	6.04	.39	

(To be continued)

Table A.2 (continued)

SOURCE	χ^2	σ_{χ^2}	Av	σ_{Av}	M	σ_M	\dot{M}	$\log(\dot{M} \text{ yr}^{-1})$	$\sigma_{\dot{M}}$	M_{disk}	$\log(M_{disk})$	\dot{M}_{disk}	$\log(\dot{M}_{disk} \text{ yr}^{-1})$	$\sigma_{M_{disk}}$	L	σ_L	Age	σ_{Age}
G335.43-0.24	21.99	3.02	31.88	15.15	3.11	2.56	-3.79	-3.63	-1.20	-1.10	-5.19	-5.16	-2.38	2.44	3.91	.92		
G2.54+0.20	15.18	3.02	15.37	10.89	5.43	1.07	-4.04	-3.96	-1.30	-1.07	-6.30	-5.91	2.34	2	5.04	.35		
G355.41+0.10	3	2.60	16.69	16.25	7.47	6.19	-3.46	-3.28	-.99	-.88	-.38	3.71	4.39	3.86	.51			
G332.56-0.15	6.32	5.15	41.34	11.19	2.82	.58	-6.30	-6.90	-2.60	-3.29	-7.32	-6.82	1.27	1.08	5.64	.53		
G305.57-0.34	8.42	3.01	6.67	7.82	2.80	1.09	-4.50	-4.46	-1.64	-1.34	-6.95	-6.54	1.70	1.51	5.03	.38		
G328.14-0.43	4.24	1.21	1.35	1.54	3.60	.49	-4.10	-3.77	-1.76	-2.31	-7.79	-8.31	1.68	-.79	5.25	.18		
G337.30-0.87	4.44	2.59	3.43	3.27	3.66	1.26	-4.28	-3.83	-1.52	-1.39	-7.30	-7.16	1.91	1.65	5.14	.28		
G341.20-0.26	4.41	2.56	2.24	3.11	1.10	.76	-5.99	-6.02	-2.01	-1.97	-7.70	-7.26	.82	.68	5.47	.20		
G0.09-0.66	3.43	2.72	7.81	6.04	2.14	.96	-4.68	-4.58	-1.96	-1.73	-7.29	-6.86	1.45	1.23	5.20	.36		
G350.36-0.07	5.41	2.52	4.90	7.16	2.64	1.32	-4.25	-4.28	-1.35	-1.24	-6.66	-6.25	1.81	1.65	4.68	.30		
G5.62-0.08	3.63	2.82	10.69	12.65	.76	.46	-4.26	-4.18	-2.57	-2.14	-2.17	.85	2.11	4.86	.35			
G326.86-0.67	3.40	2.69	9.67	7.09	1.15	.72	-.5	-4.71	-2.14	-1.73	-7.24	-7.03	1.06	1.05	5.07	.36		
G358.46-0.39(b)	4	2.74	9.41	11.43	1.37	.83	-5.08	-4.58	-2.19	-2.01	-7.47	-7.35	1.14	.94	5.03	.35		

Appendix B: Figures

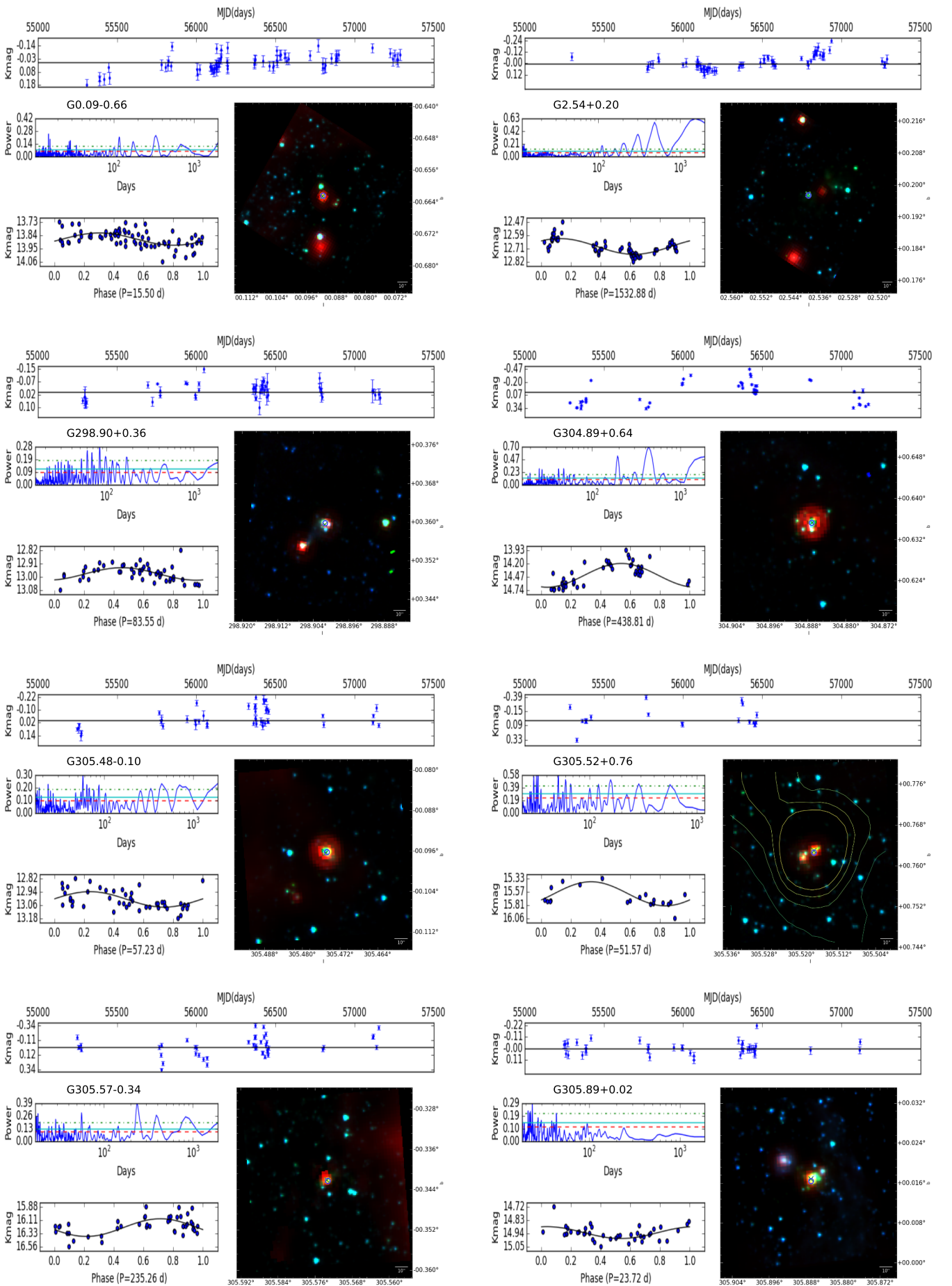


Fig. B.1: LC of the source, with error bars representing $\text{MAD}(\Delta S_{i_{\text{mid}}})$, periodograms (also plotted are the 99%, 95%, and 90% false probability levels, respectively: the green dot-dashed line, the cyan full line, and the red dashed line), the phase-folded LC using the best period fitted, the RGB image of the source using the Spitzer IRAC $3.6 \mu\text{m}$, IRAC $4.0 \mu\text{m}$, and the $24 \mu\text{m}$ MIPS band as blue, green and red, respectively. The VVV source is marked by the blue circle and the green cross represents the MIPS co-ordinates. The contours of the RGB are in the interval of [Peak- 5σ , Peak] from the ATLASGAL observation at $850 \mu\text{m}$.

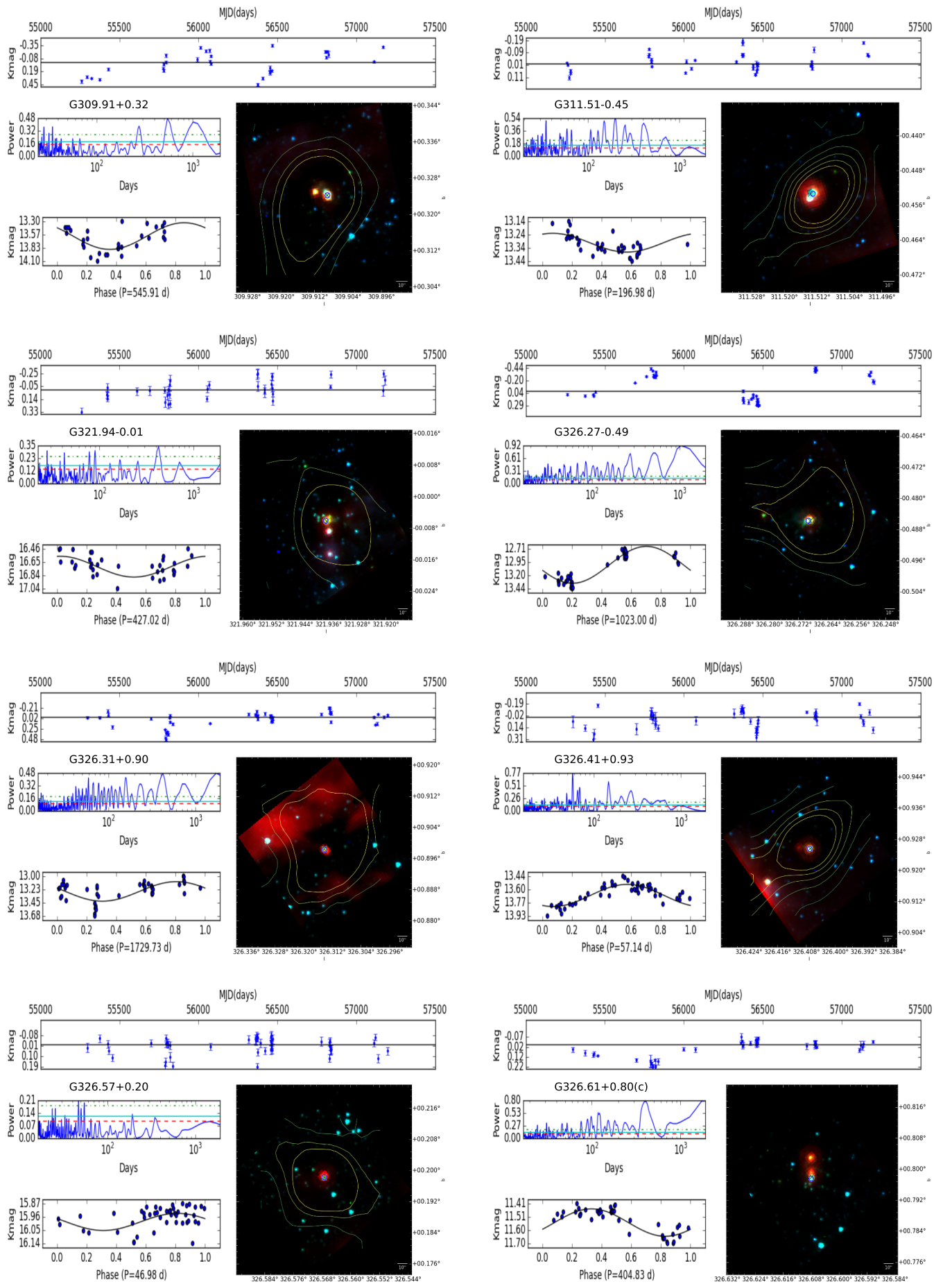


Fig. B.2: Continuation of Fig. B.1.

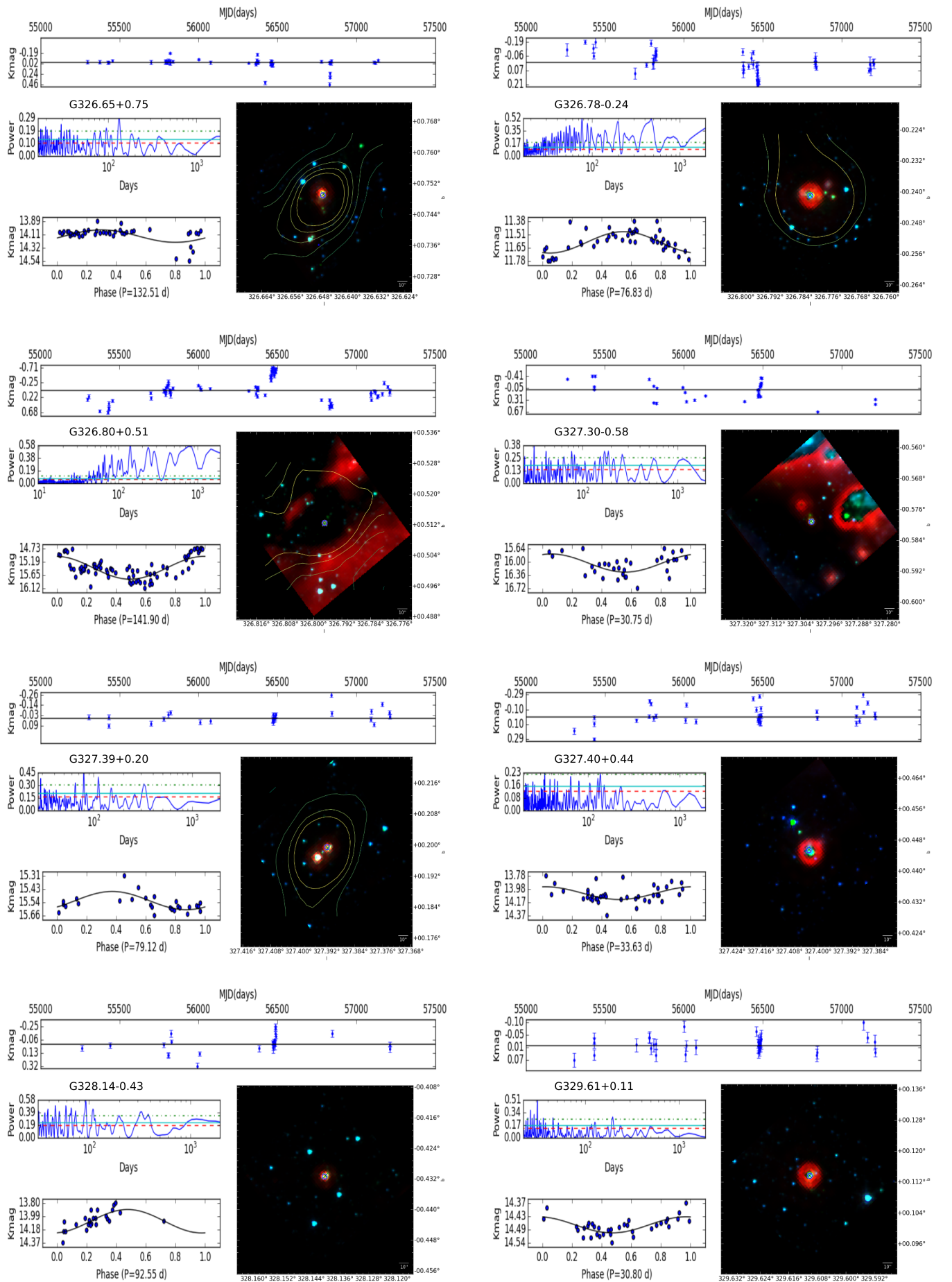


Fig. B.3: Continuation of Fig. B.1.

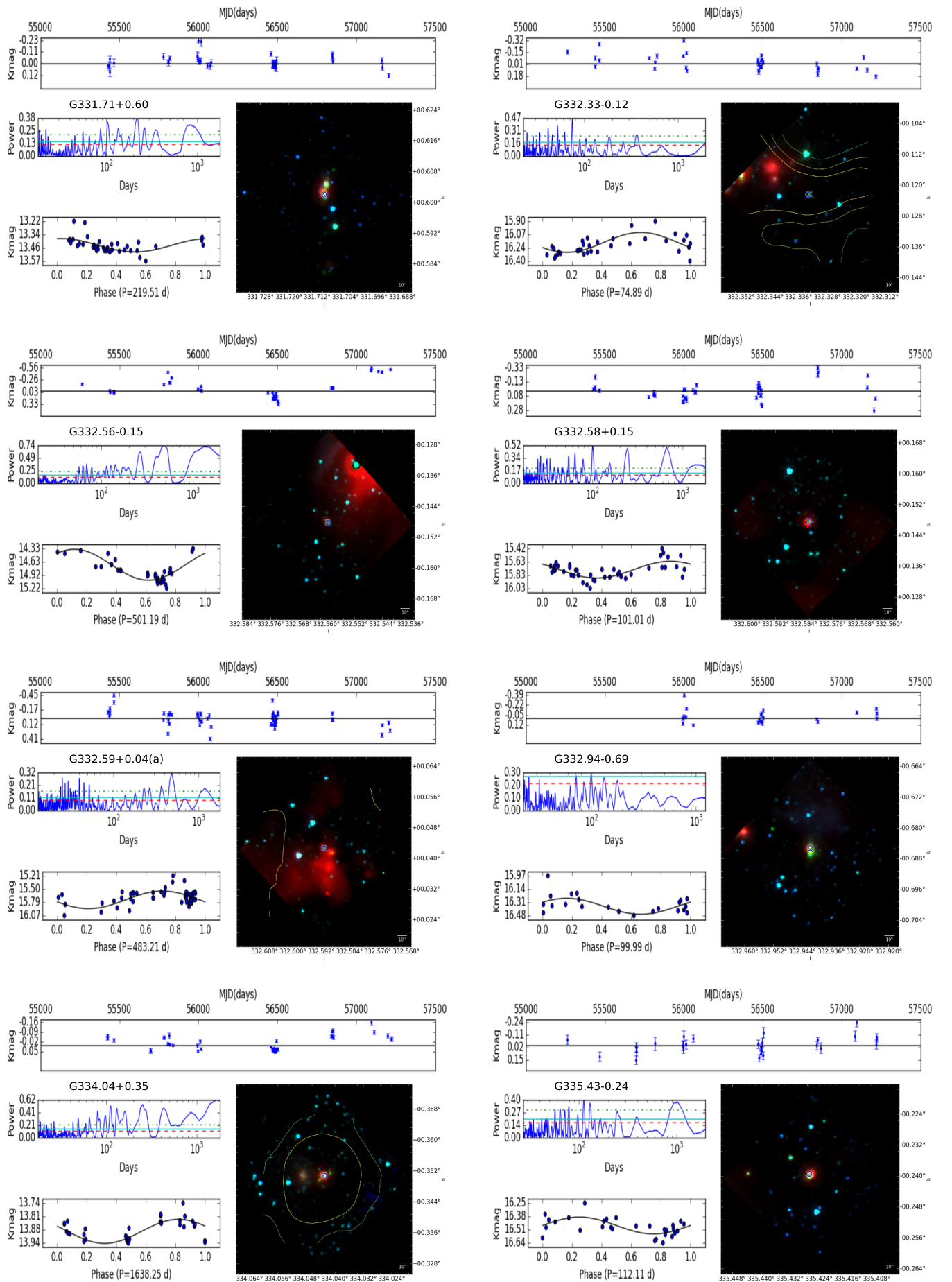


Fig. B.4: Continuation of Fig. B.1.

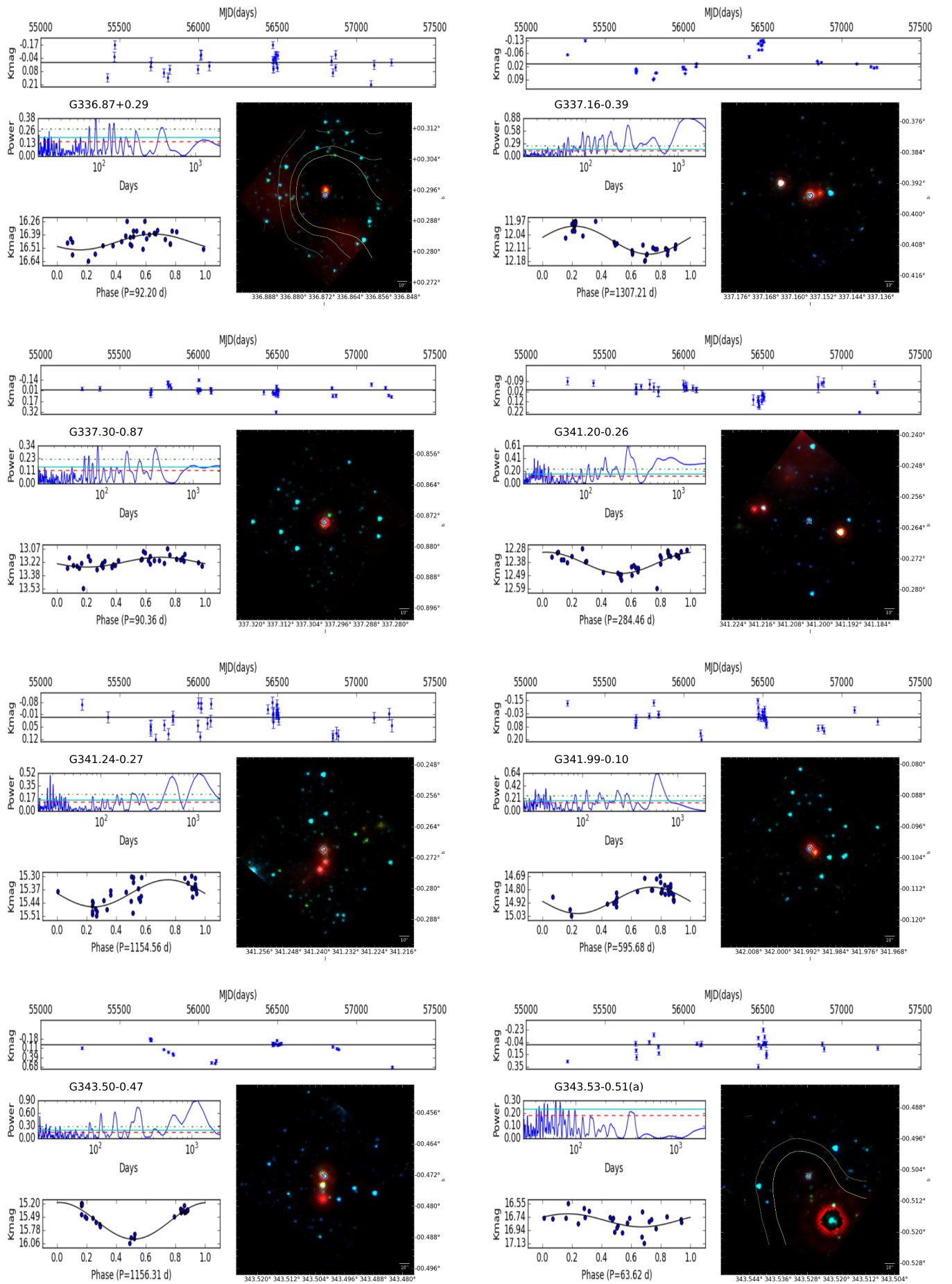


Fig. B.5: Continuation of Fig. B.1.

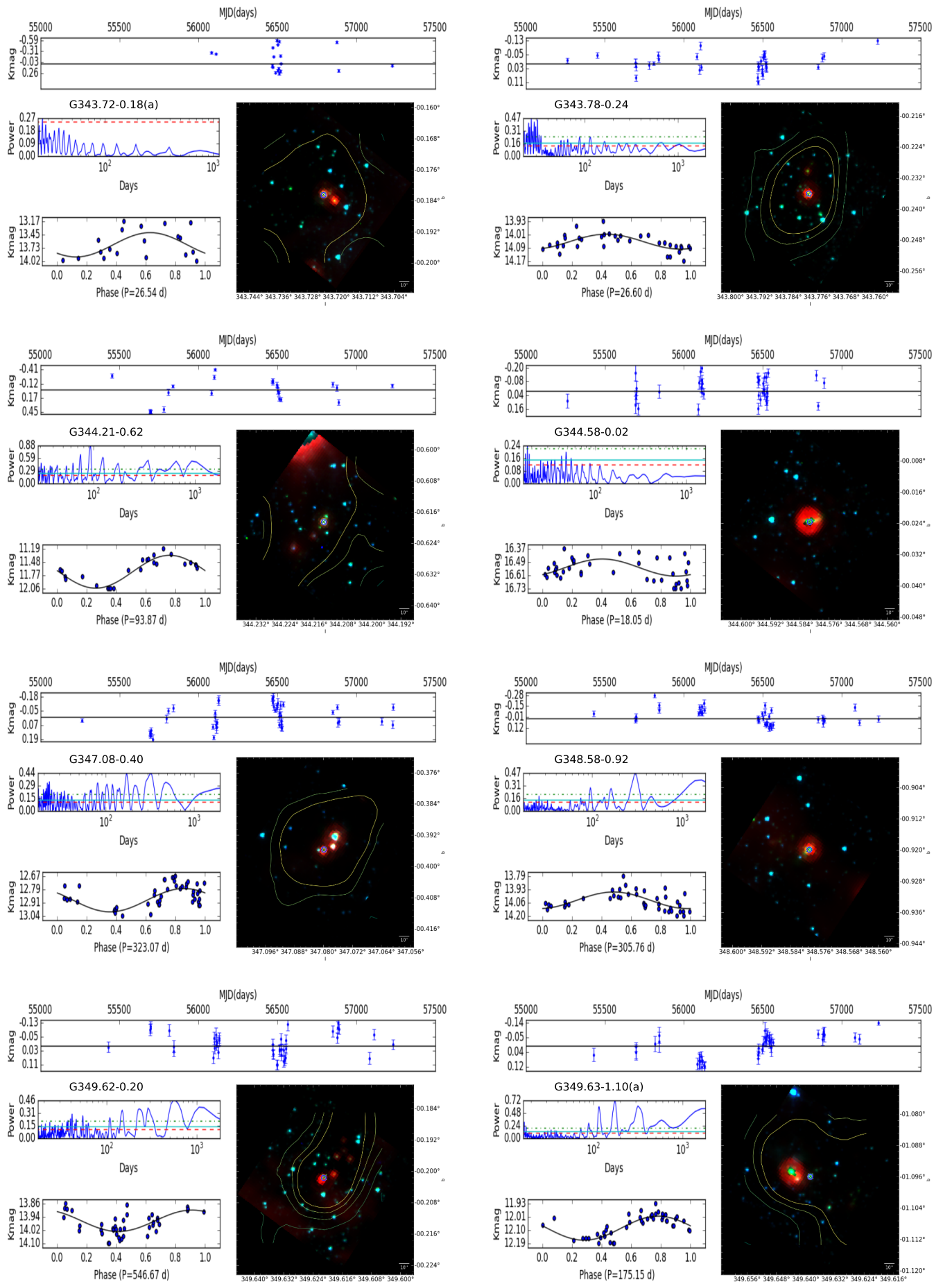


Fig. B.6: Continuation of Fig. B.1.

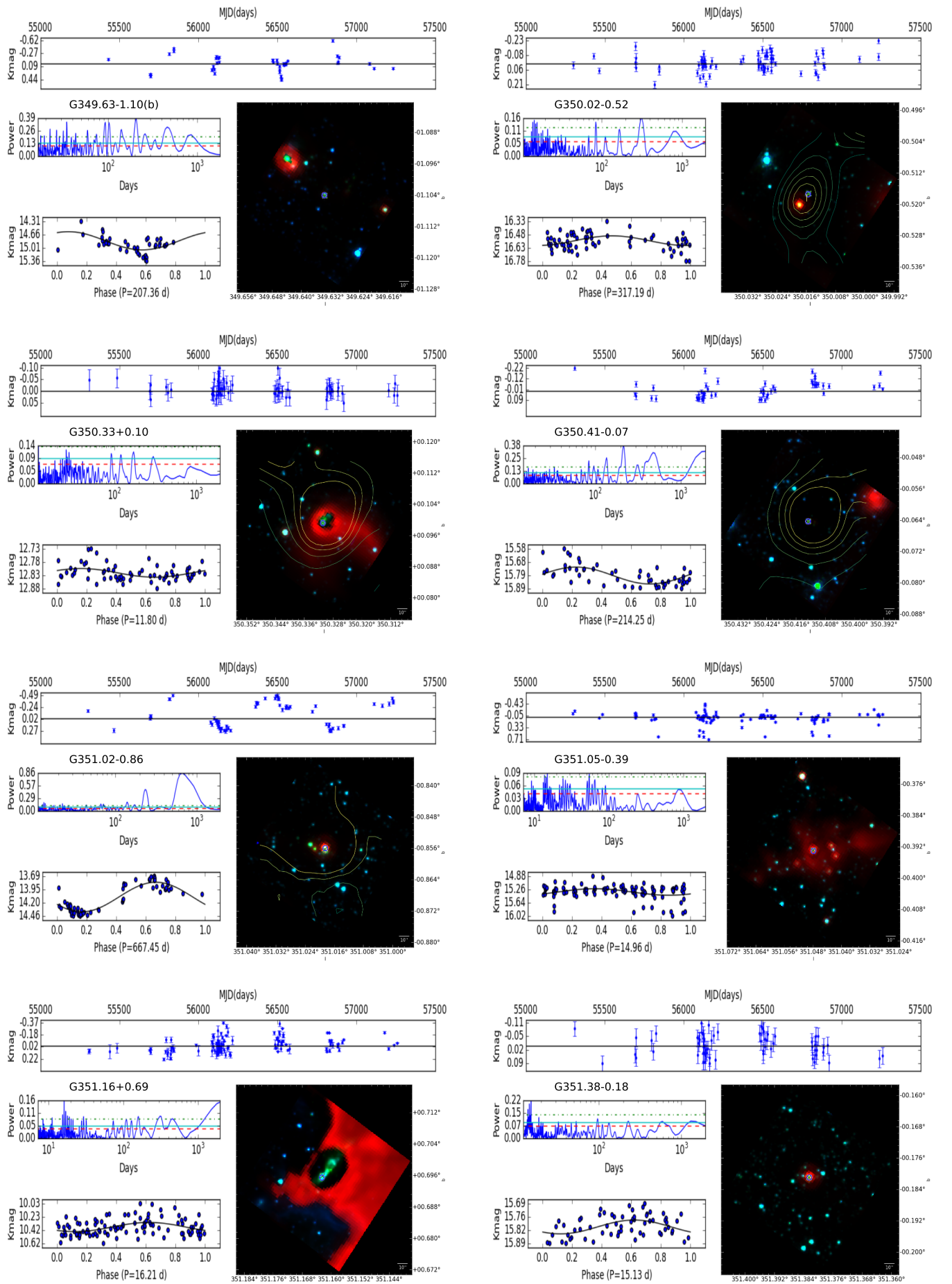


Fig. B.7: Continuation of Fig. B.1.

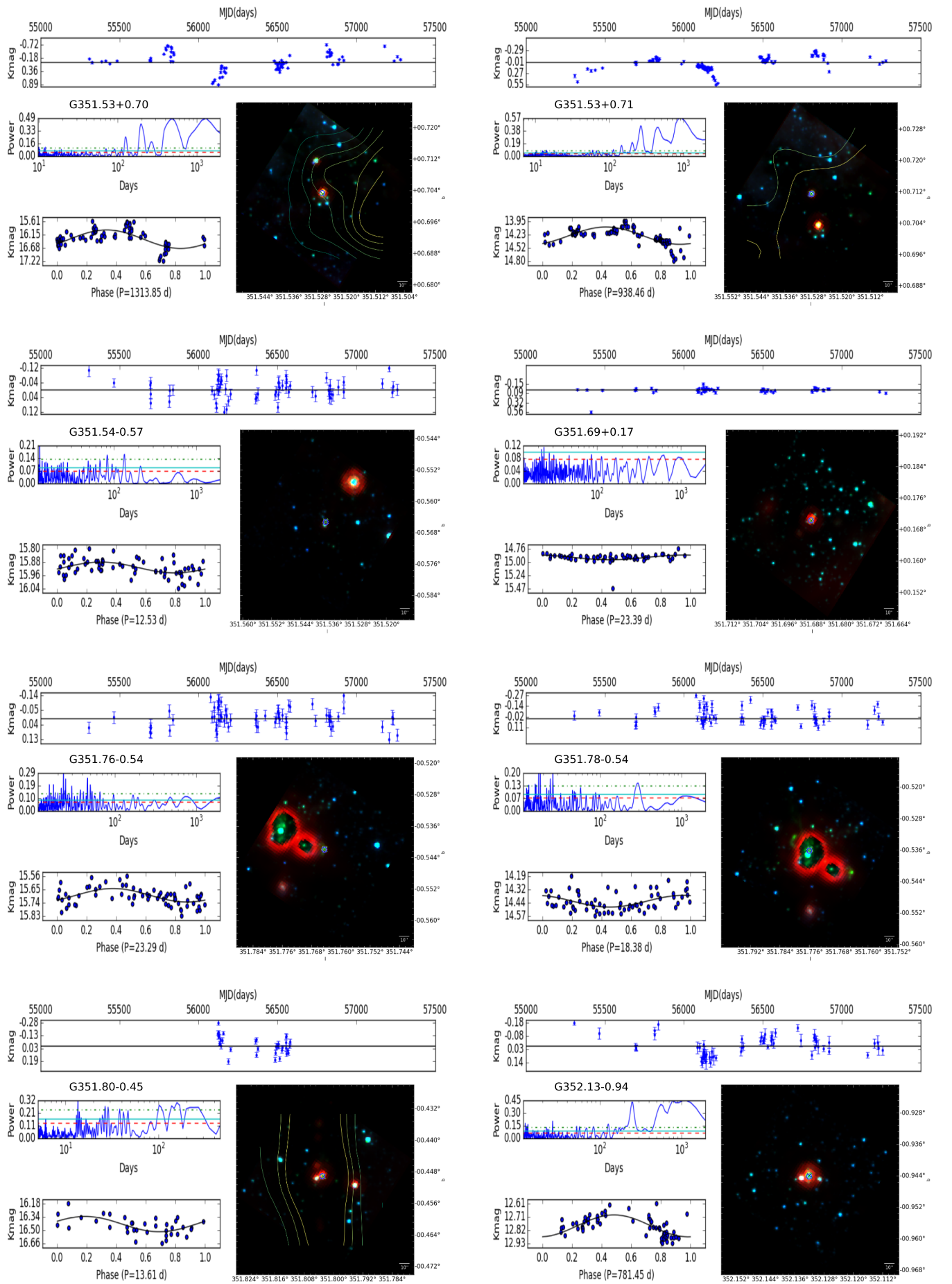


Fig. B.8: Continuation of Fig. B.1.

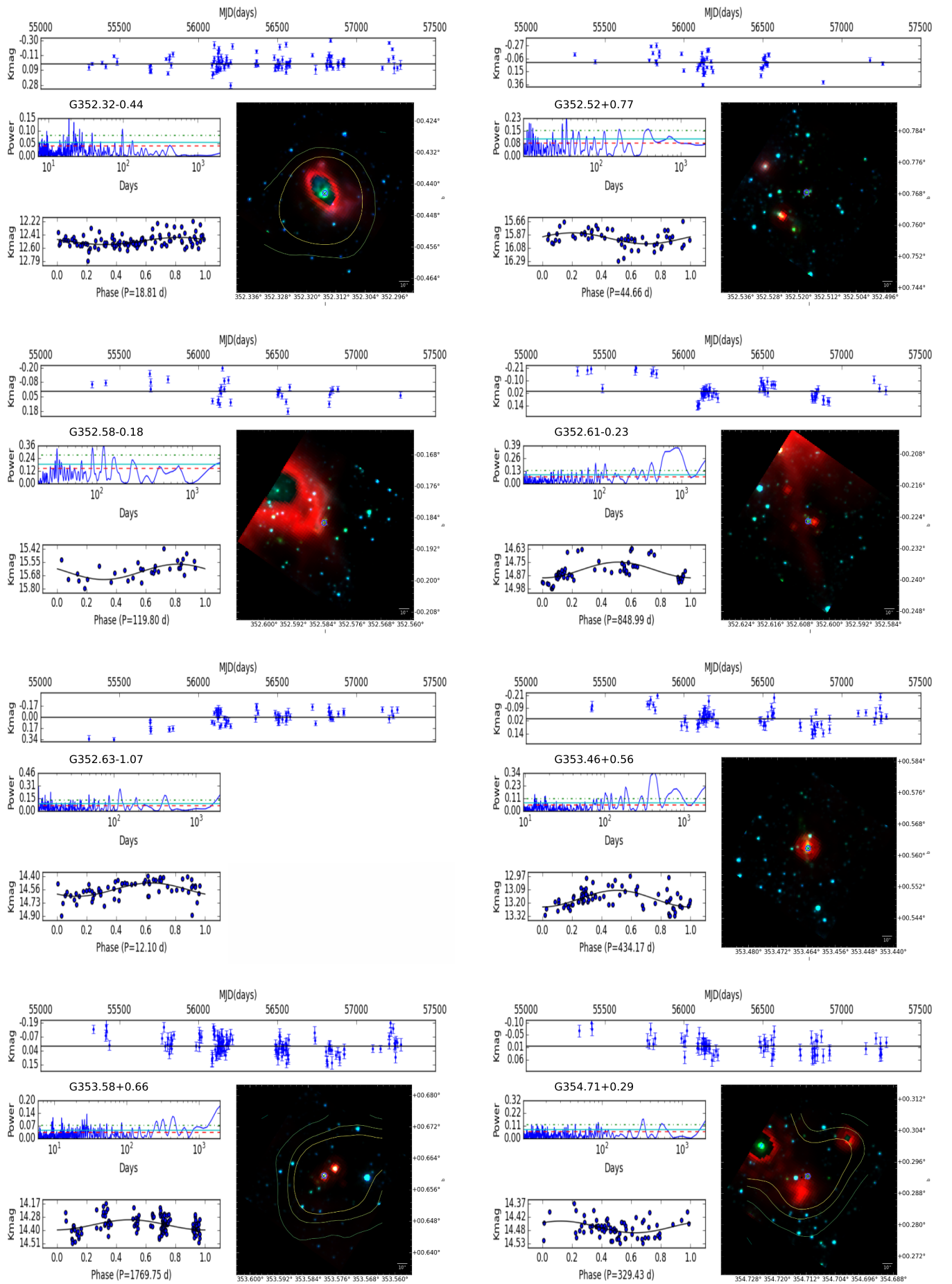


Fig. B.9: Continuation of Fig. B.1.

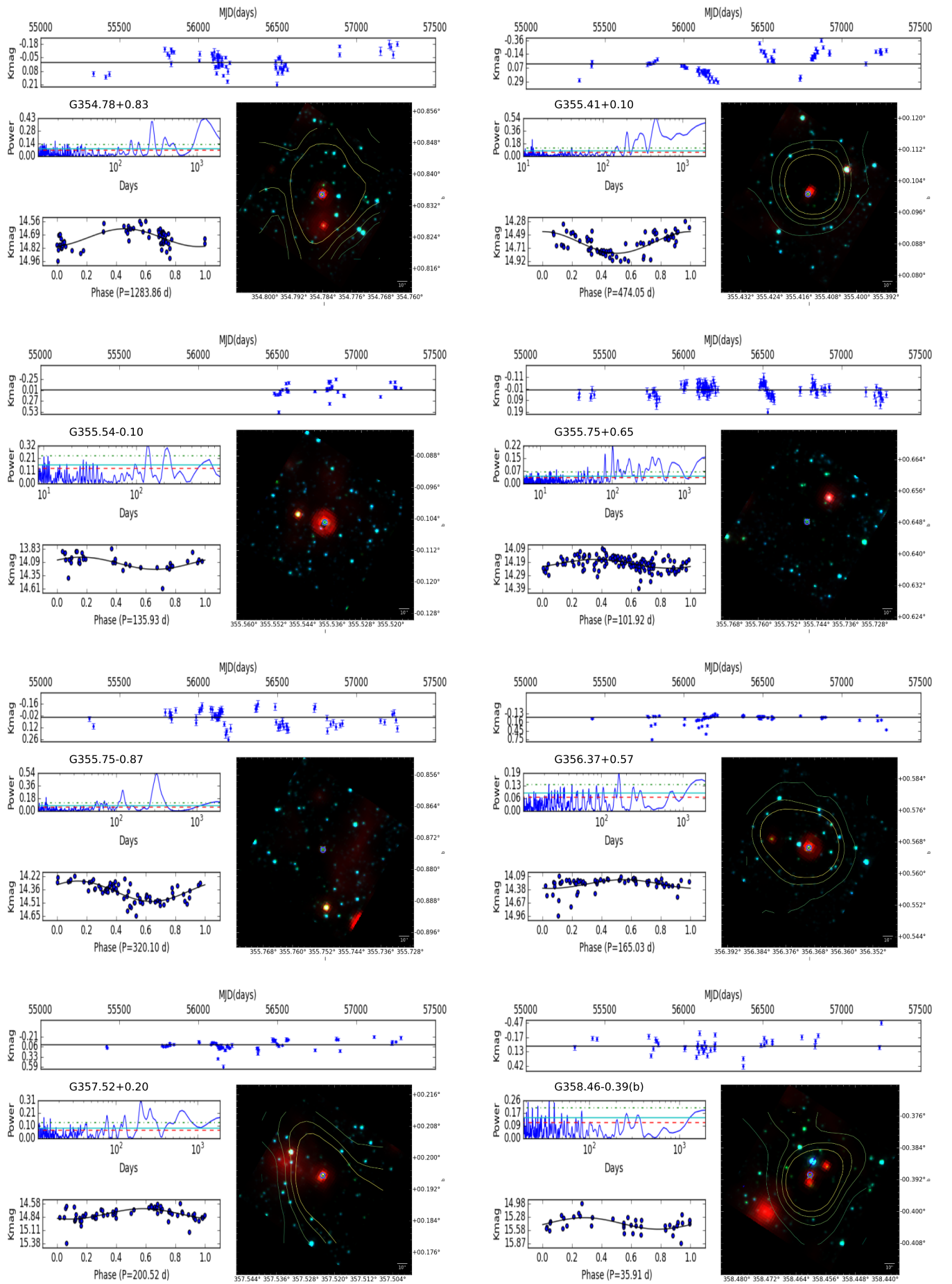


Fig. B.10: Continuation of Fig. B.1.

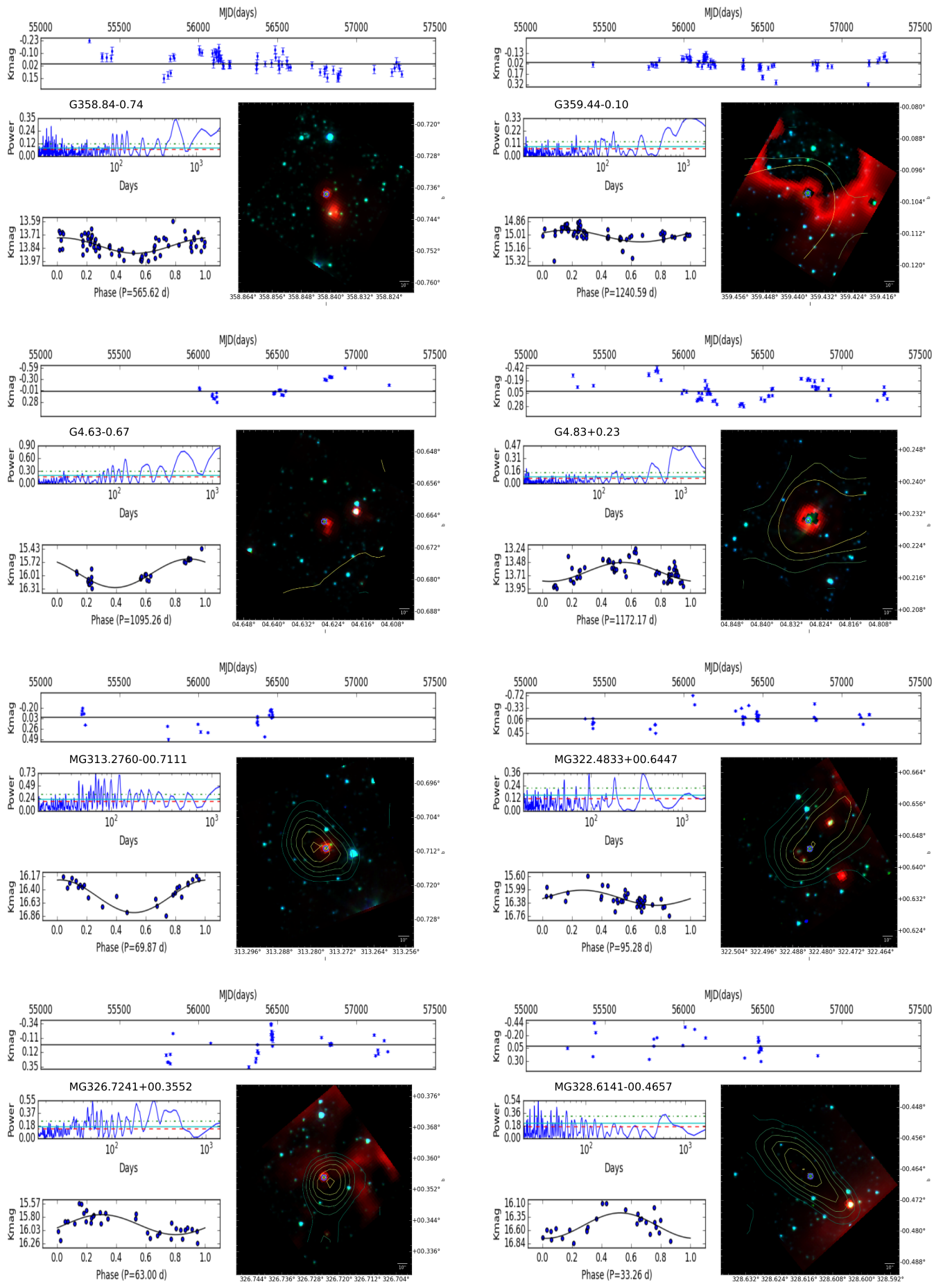


Fig. B.11: Continuation of Fig. B.1.

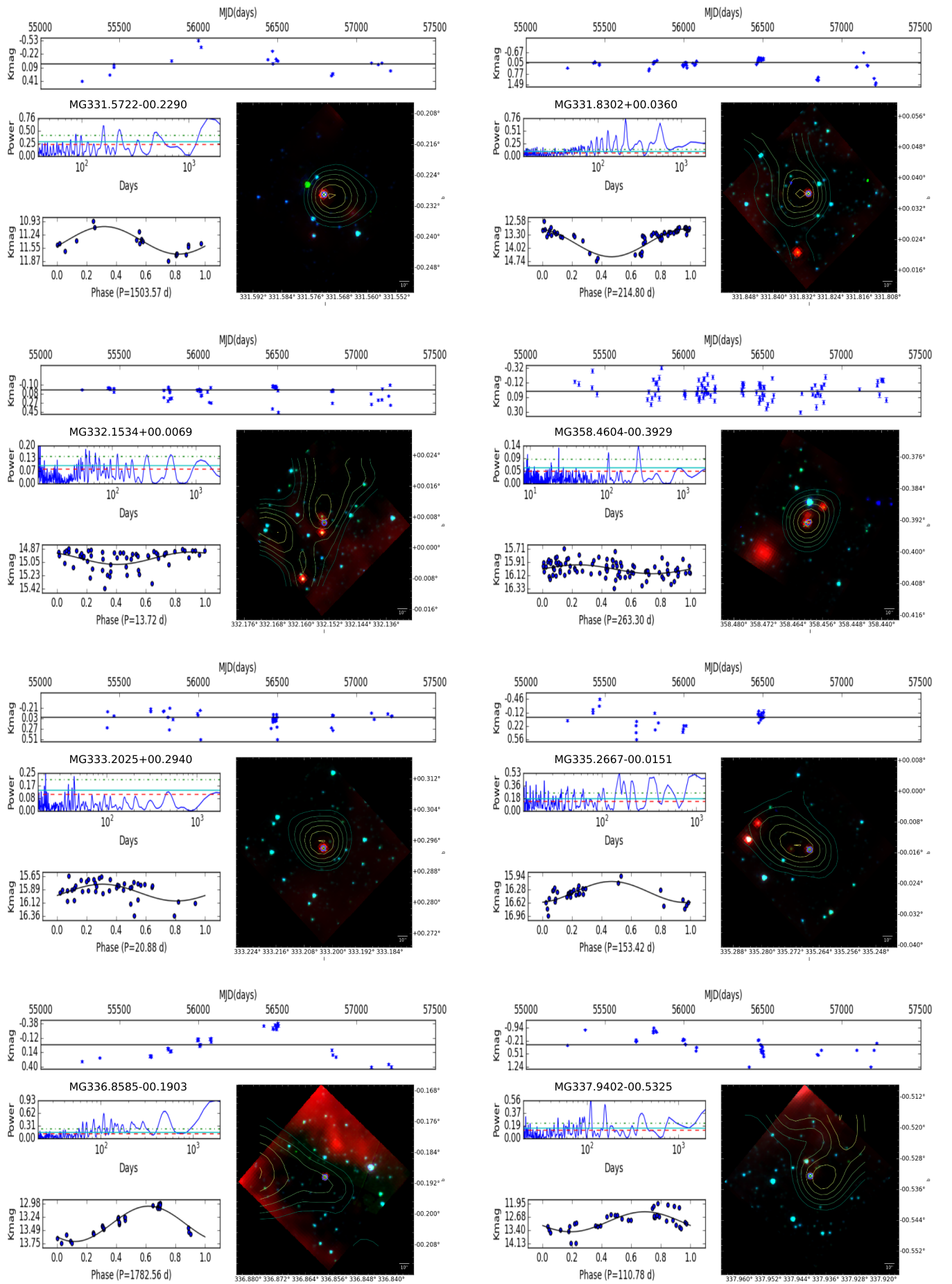


Fig. B.12: Continuation of Fig. B.1.

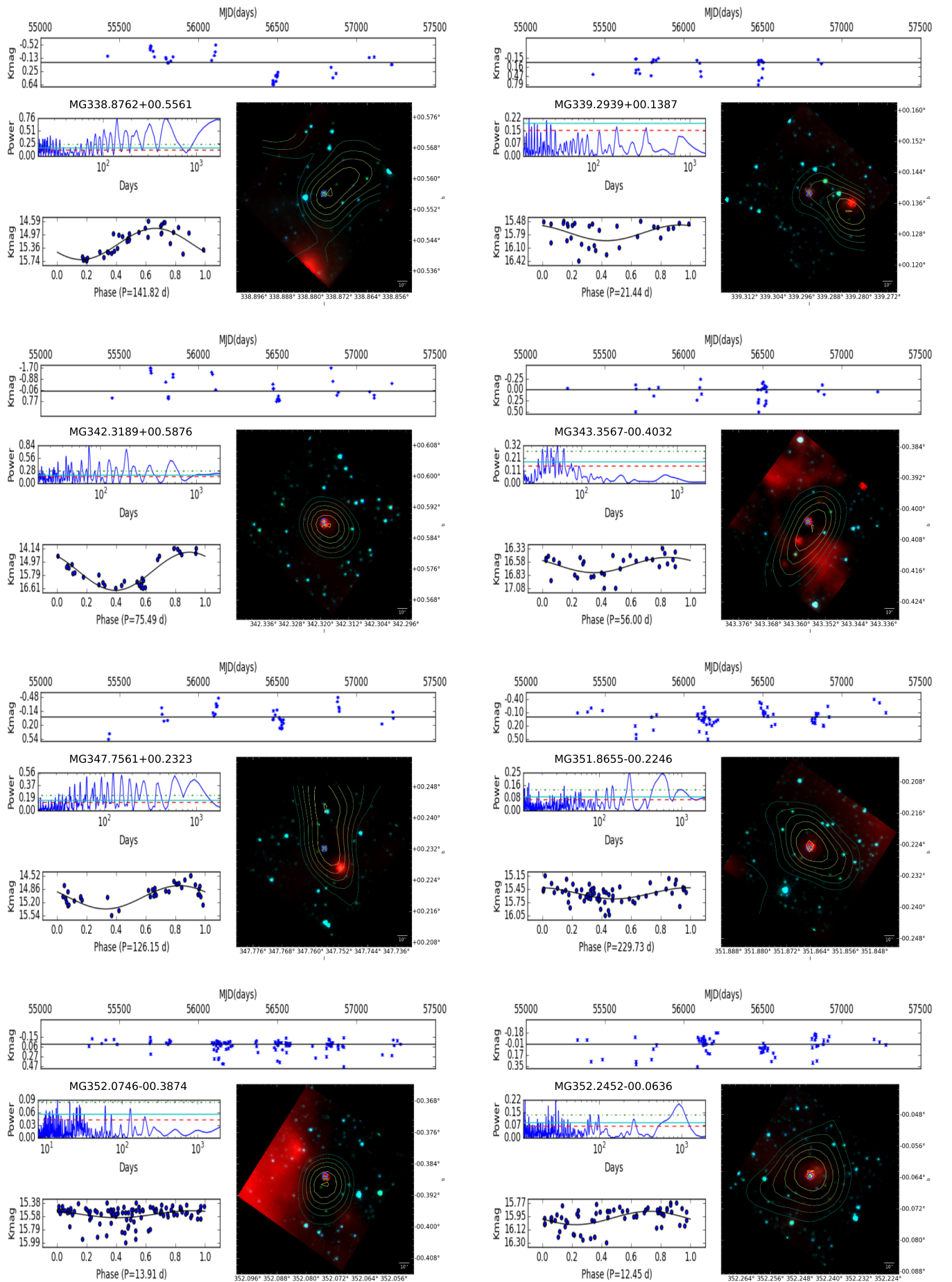


Fig. B.13: Continuation of Fig. B.1.

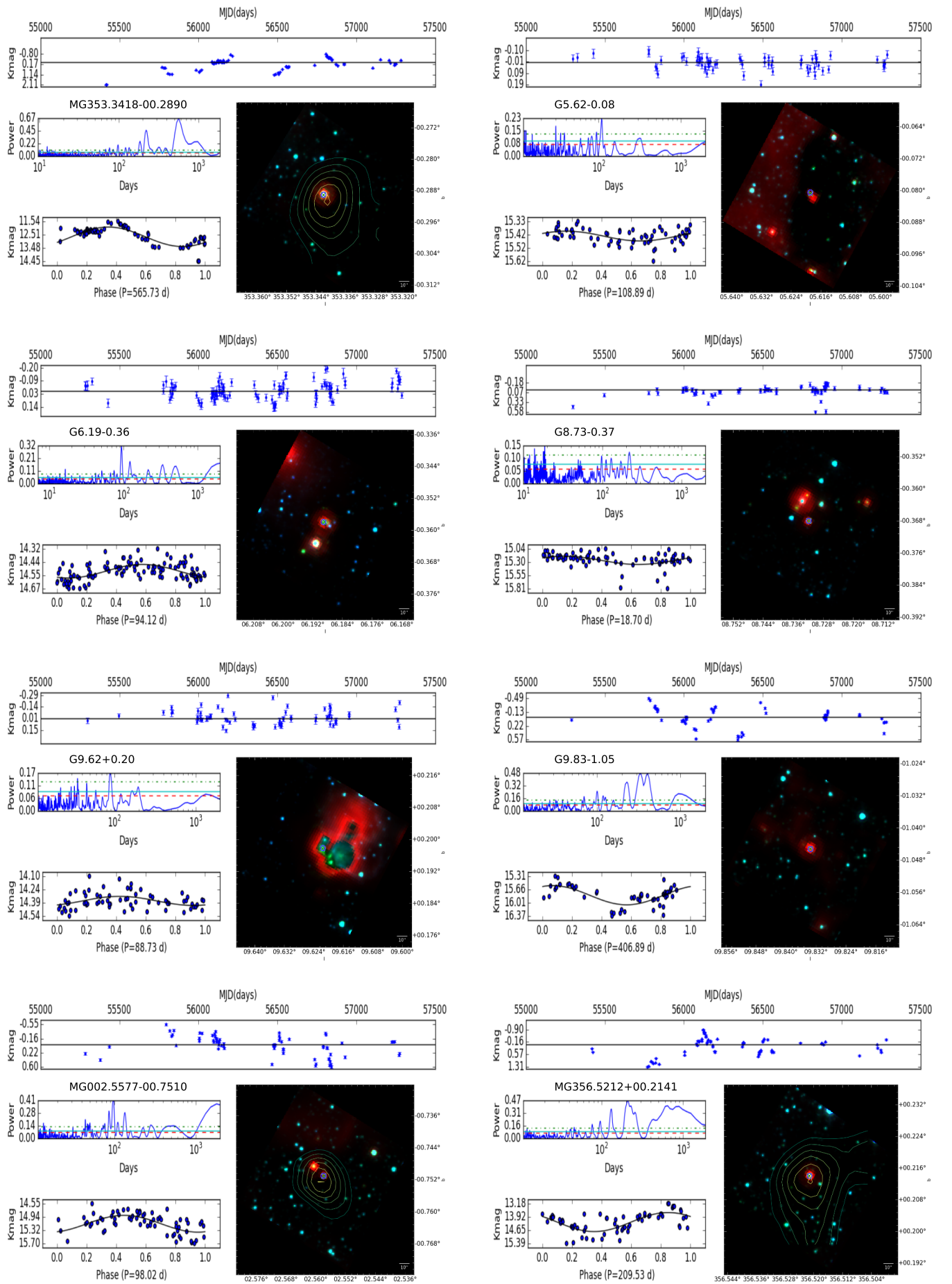


Fig. B.14: Continuation of Fig. B.1.

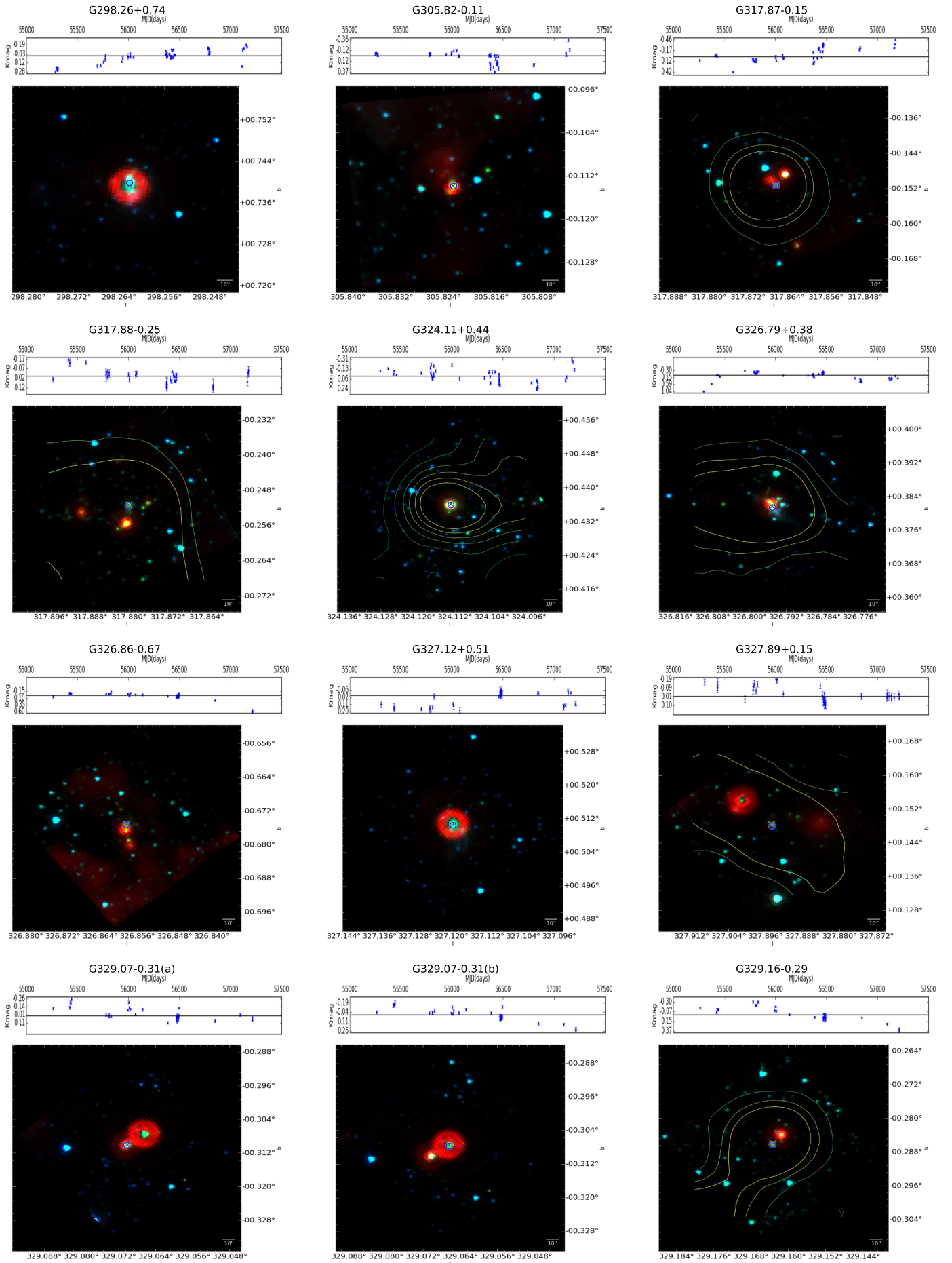


Fig. B.15: Continuation of Fig. B.1.

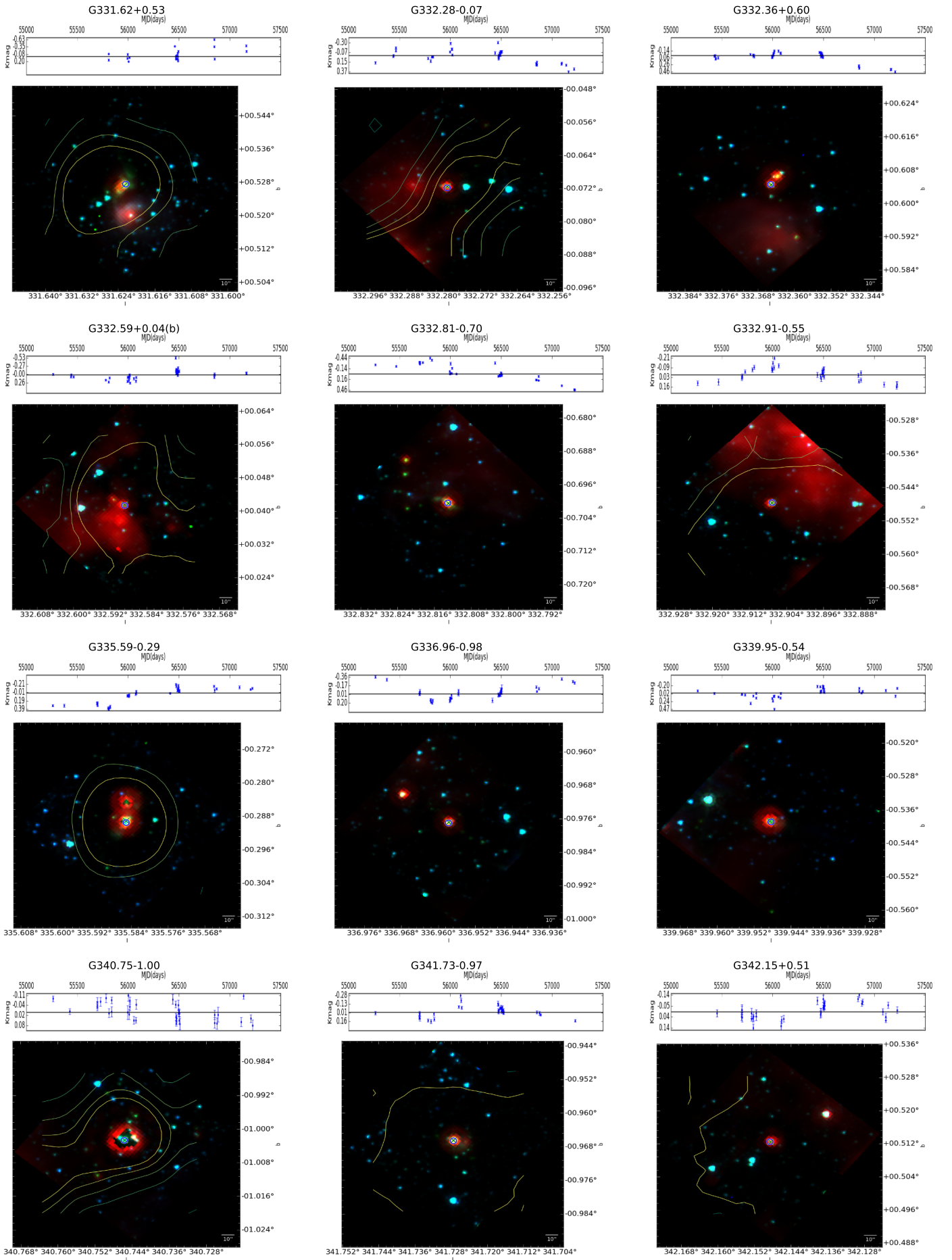


Fig. B.16: Continuation of Fig. B.1.

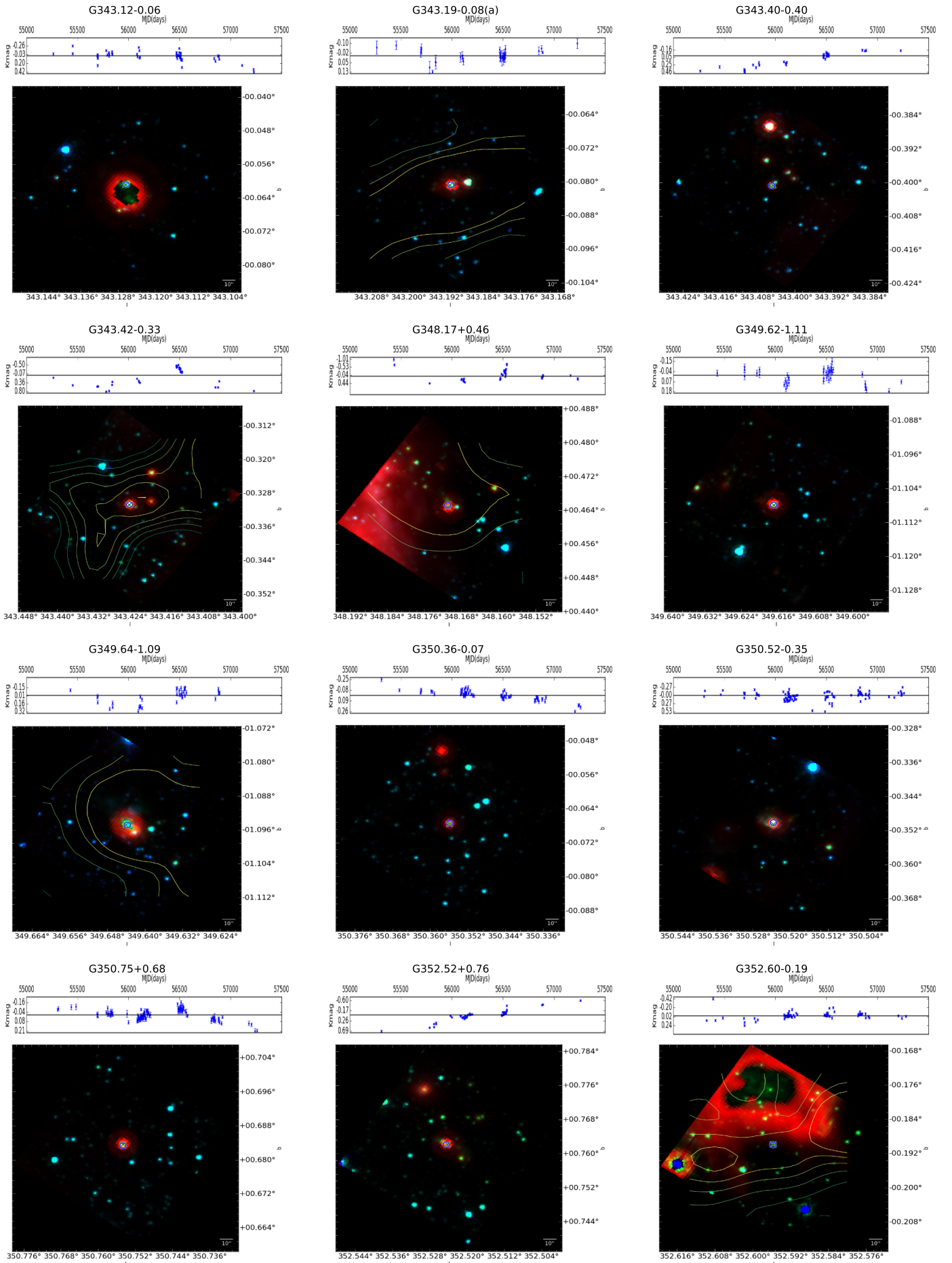


Fig. B.17: Continuation of Fig. B.1.

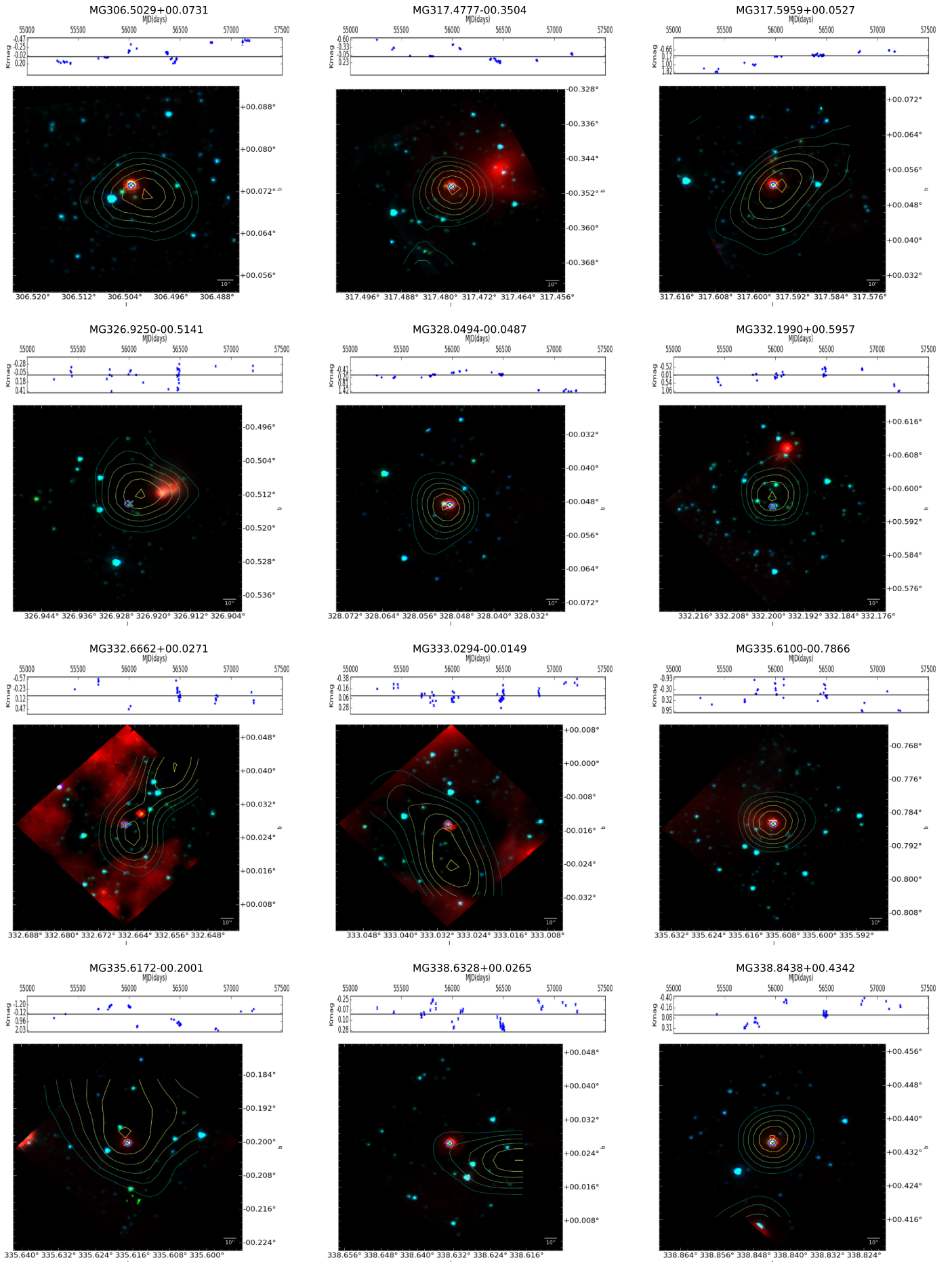


Fig. B.18: Continuation of Fig. B.1.

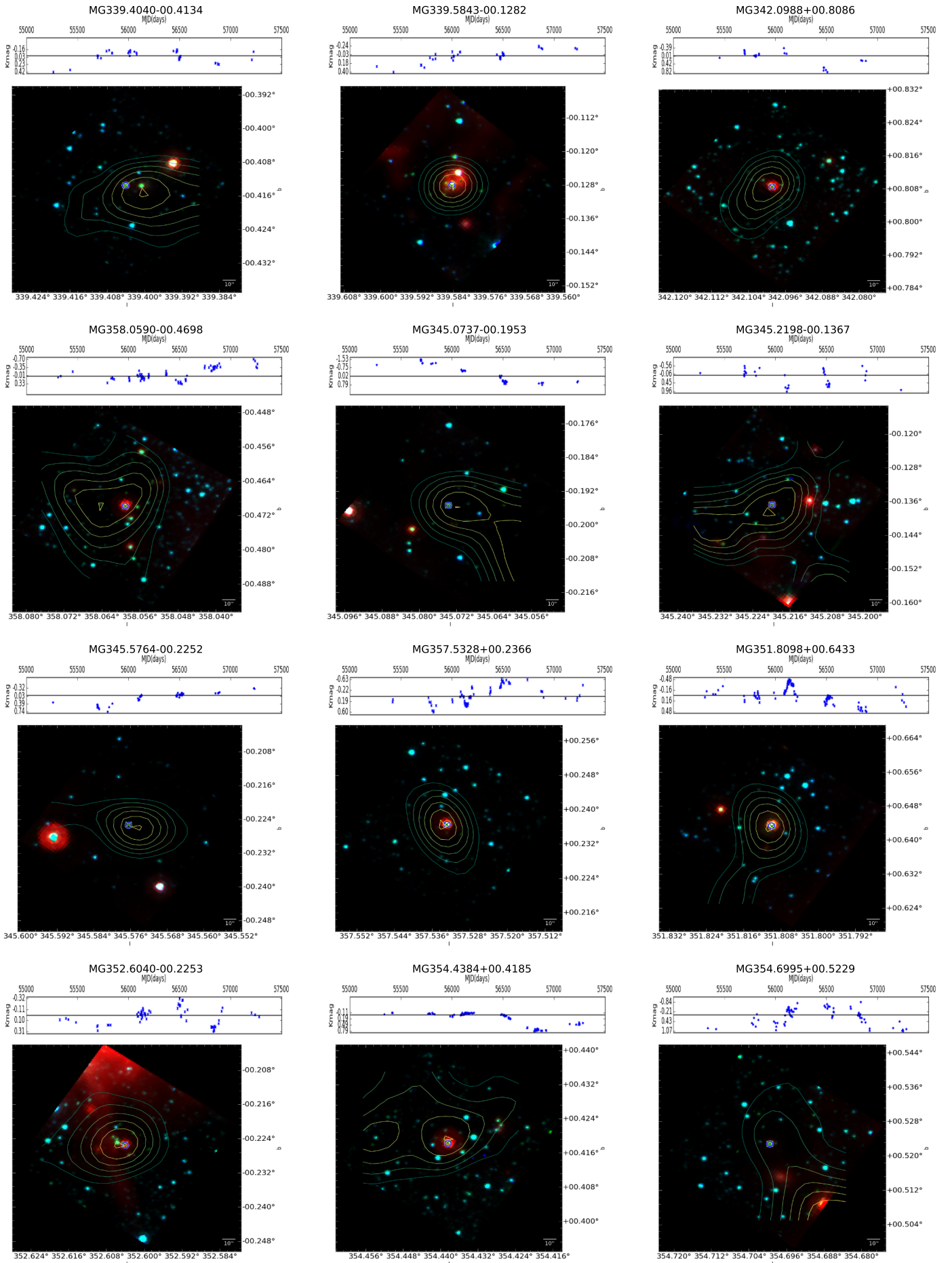


Fig. B.19: Continuation of Fig. B.1.

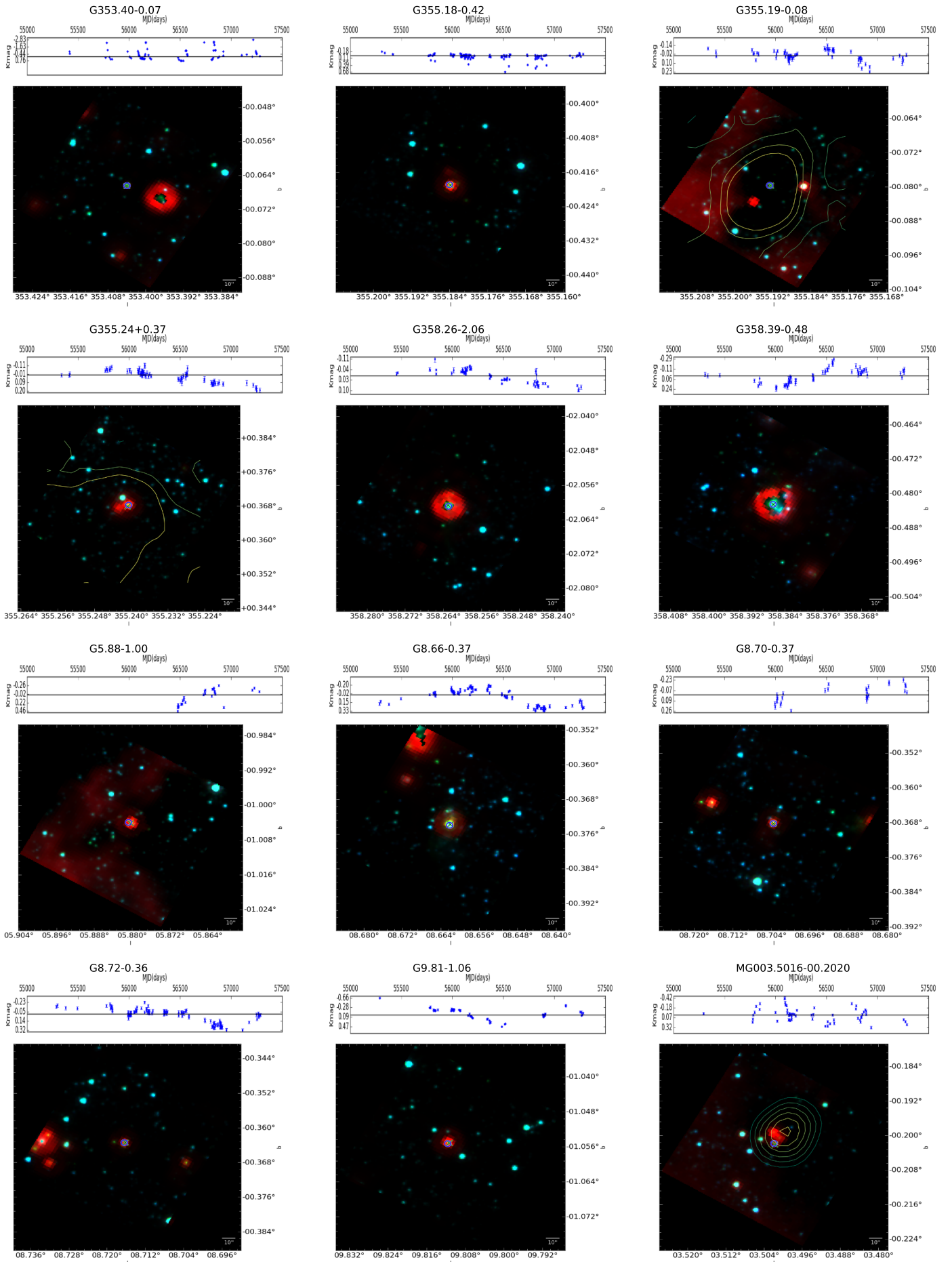


Fig. B.20: Continuation of Fig. B.1.

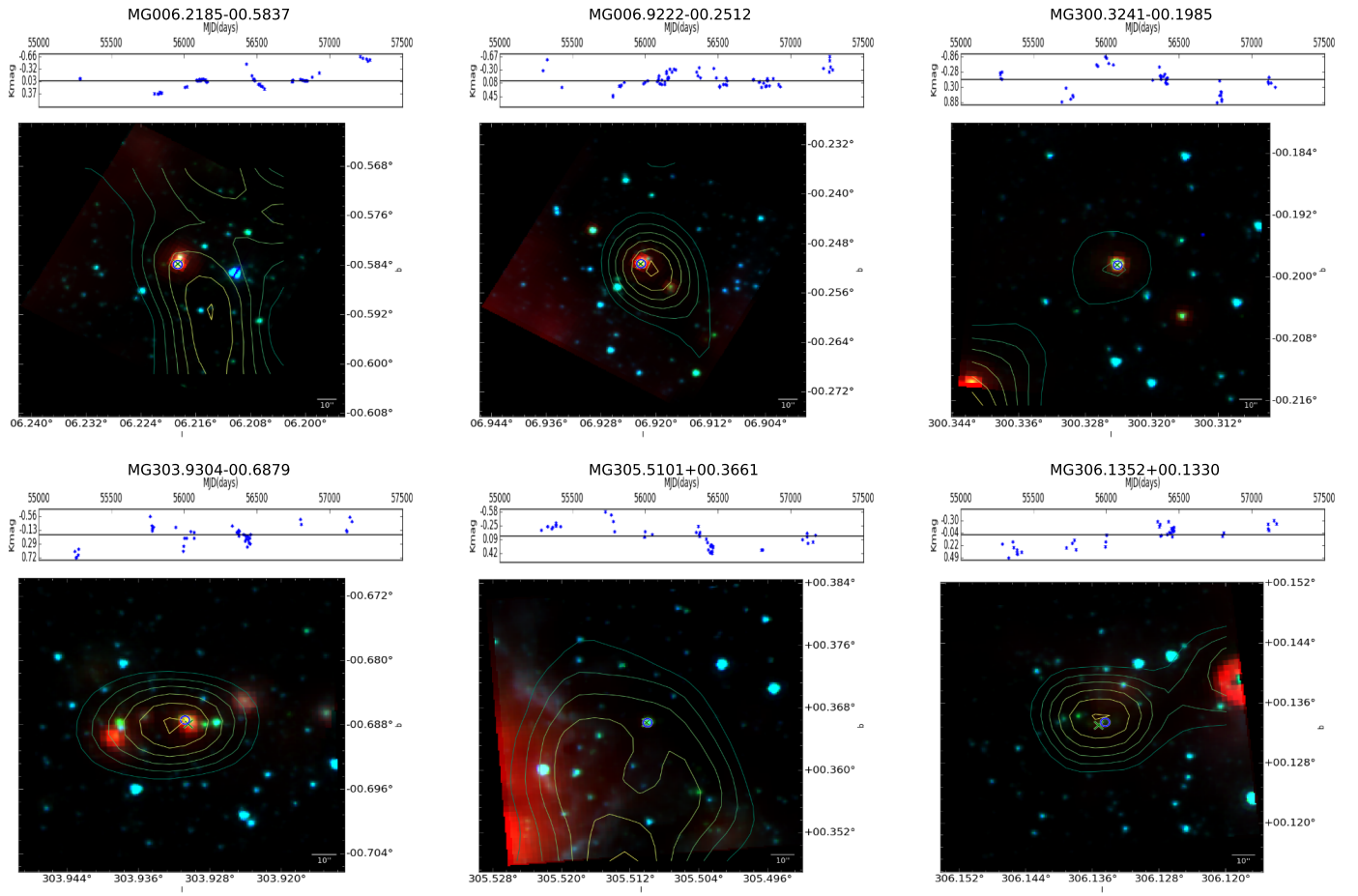


Fig. B.21: Continuation of Fig. B.1.

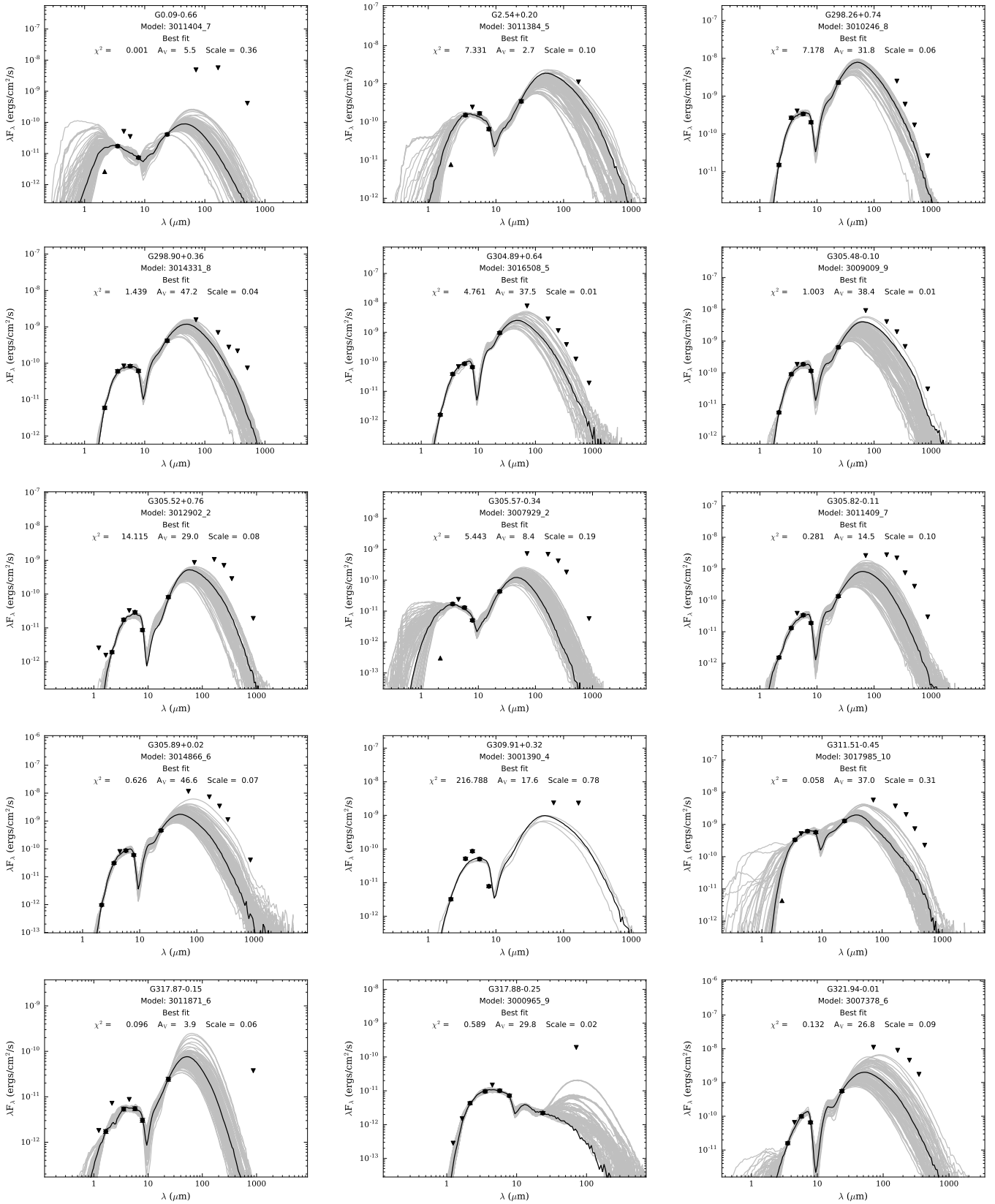


Fig. B.22: The fitted SEDs with the best fit model in the black line, the grey lines are other $\chi^2 - \chi^2_{best} < 3$ models, data points, upper, and lower limits are, respectively, circles, inverted triangles, and triangles.

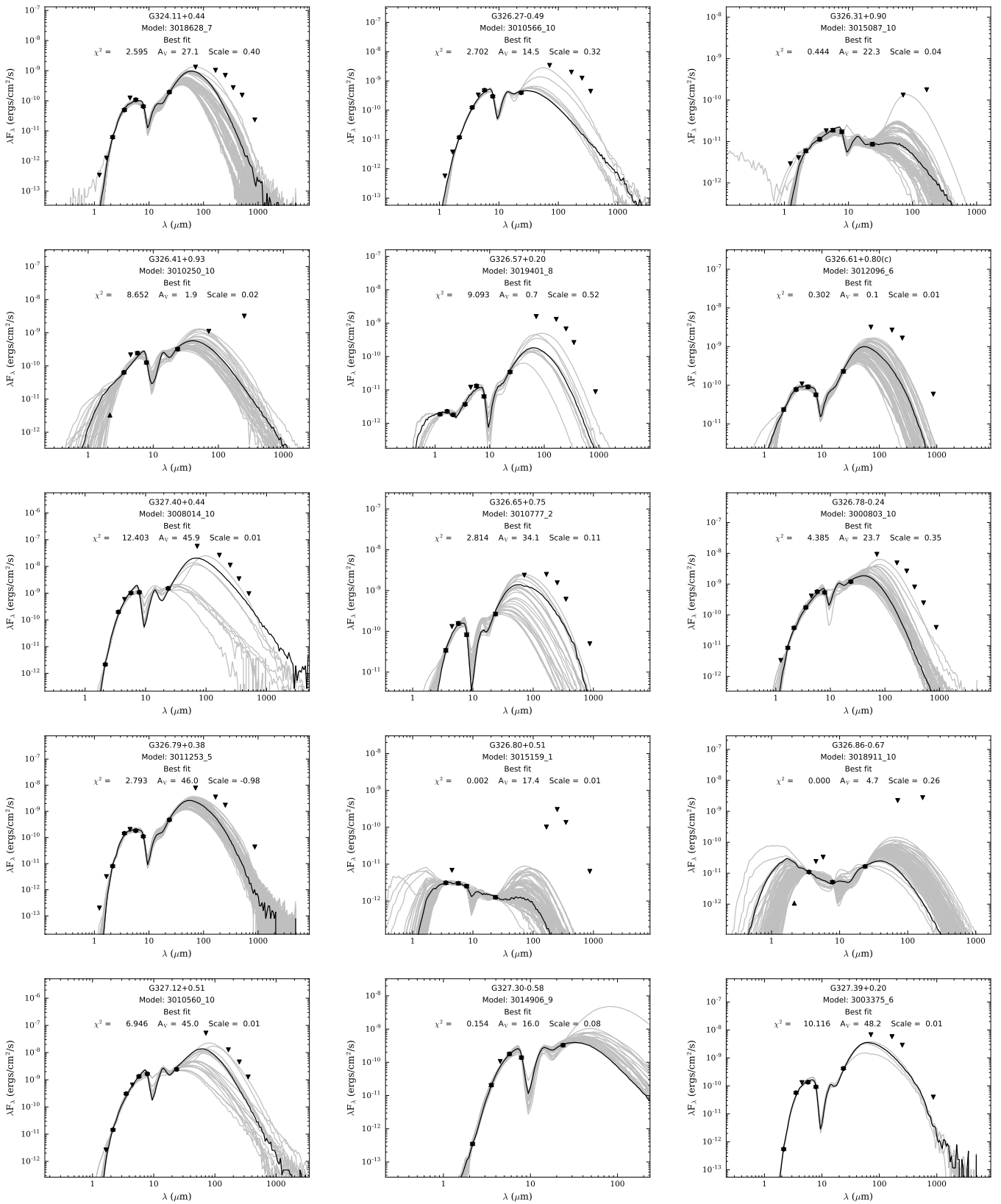


Fig. B.23: Continuation of Fig. B.22.

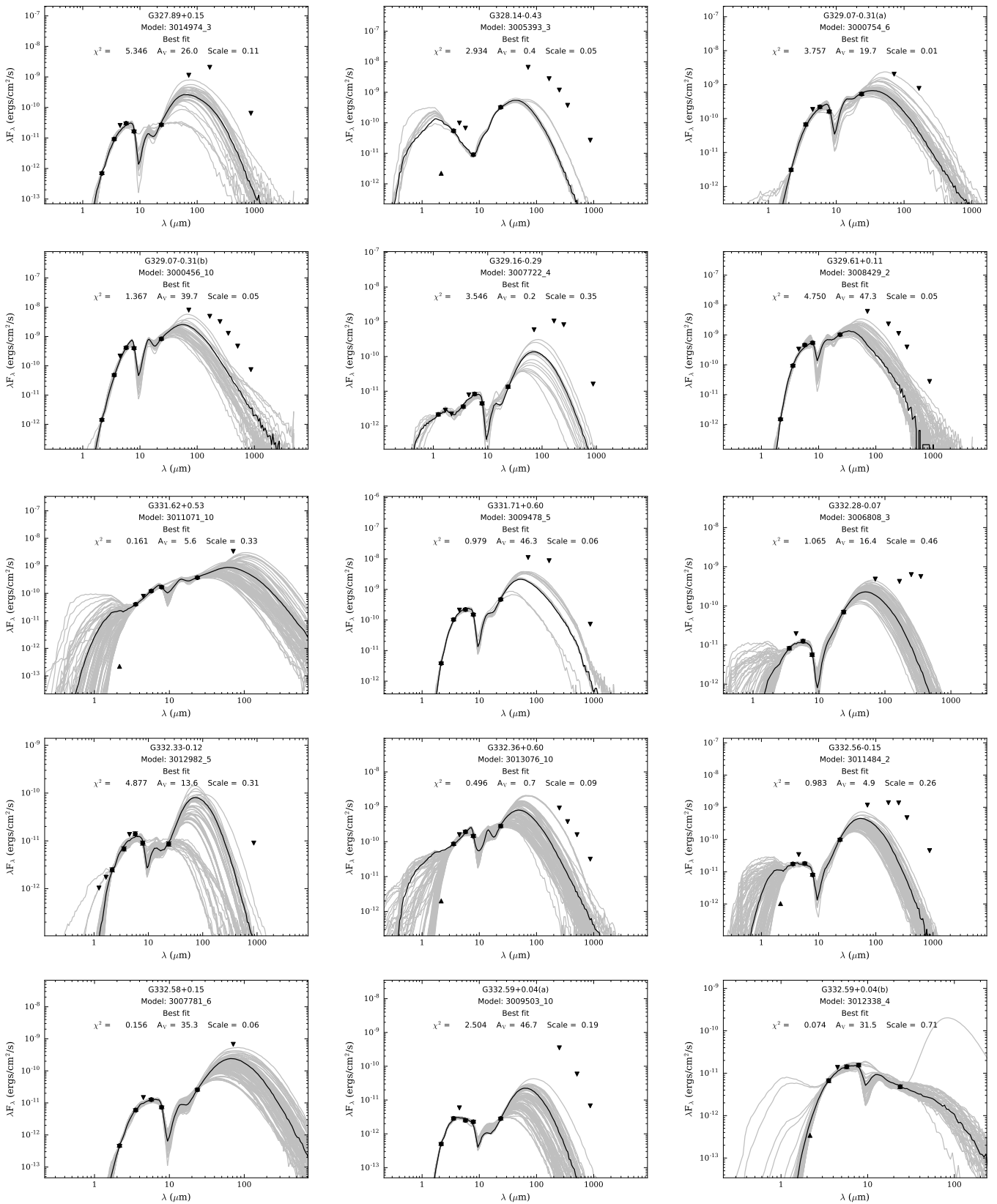


Fig. B.24: Continuation of Fig. B.22.

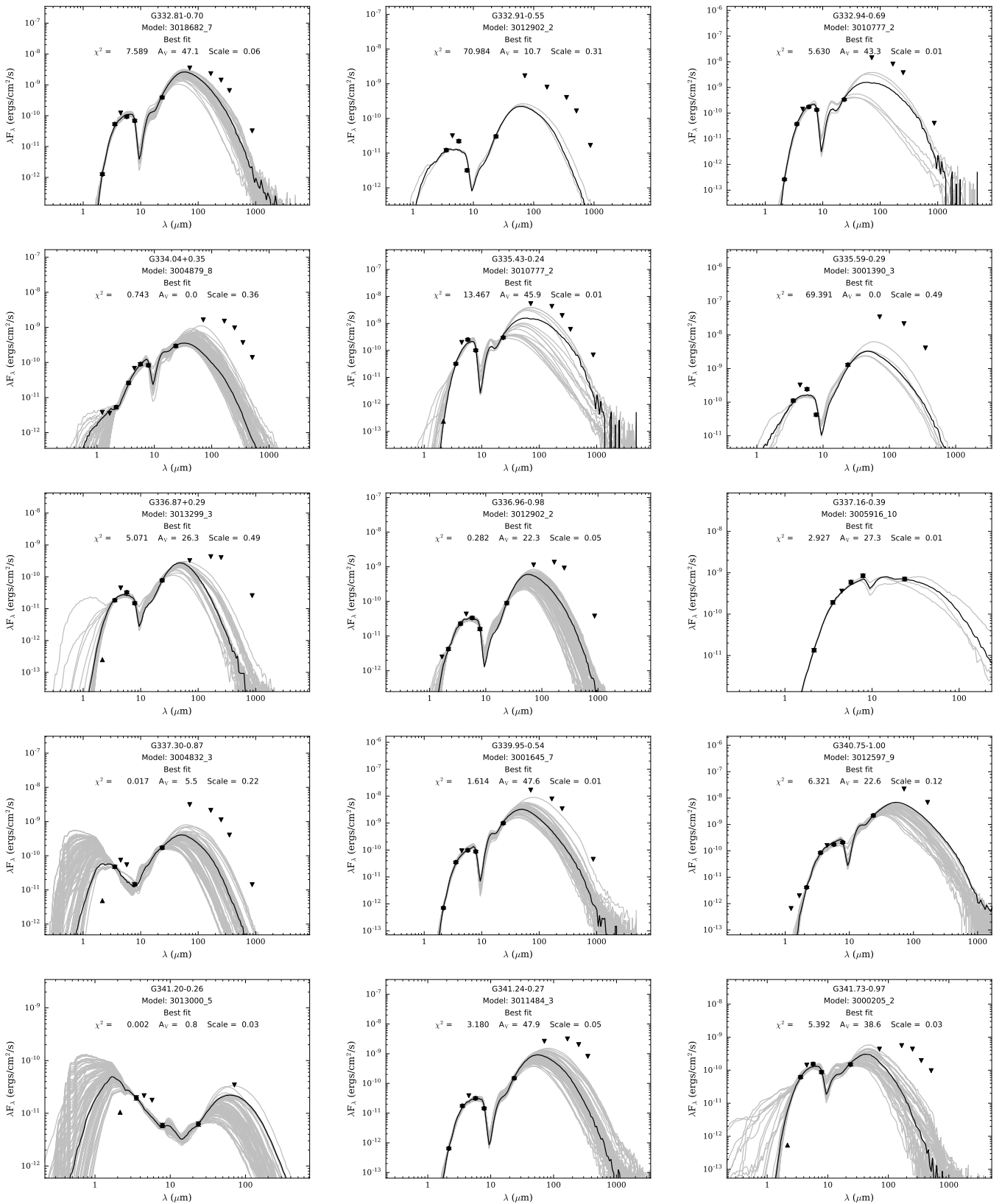


Fig. B.25: Continuation of Fig. B.22.

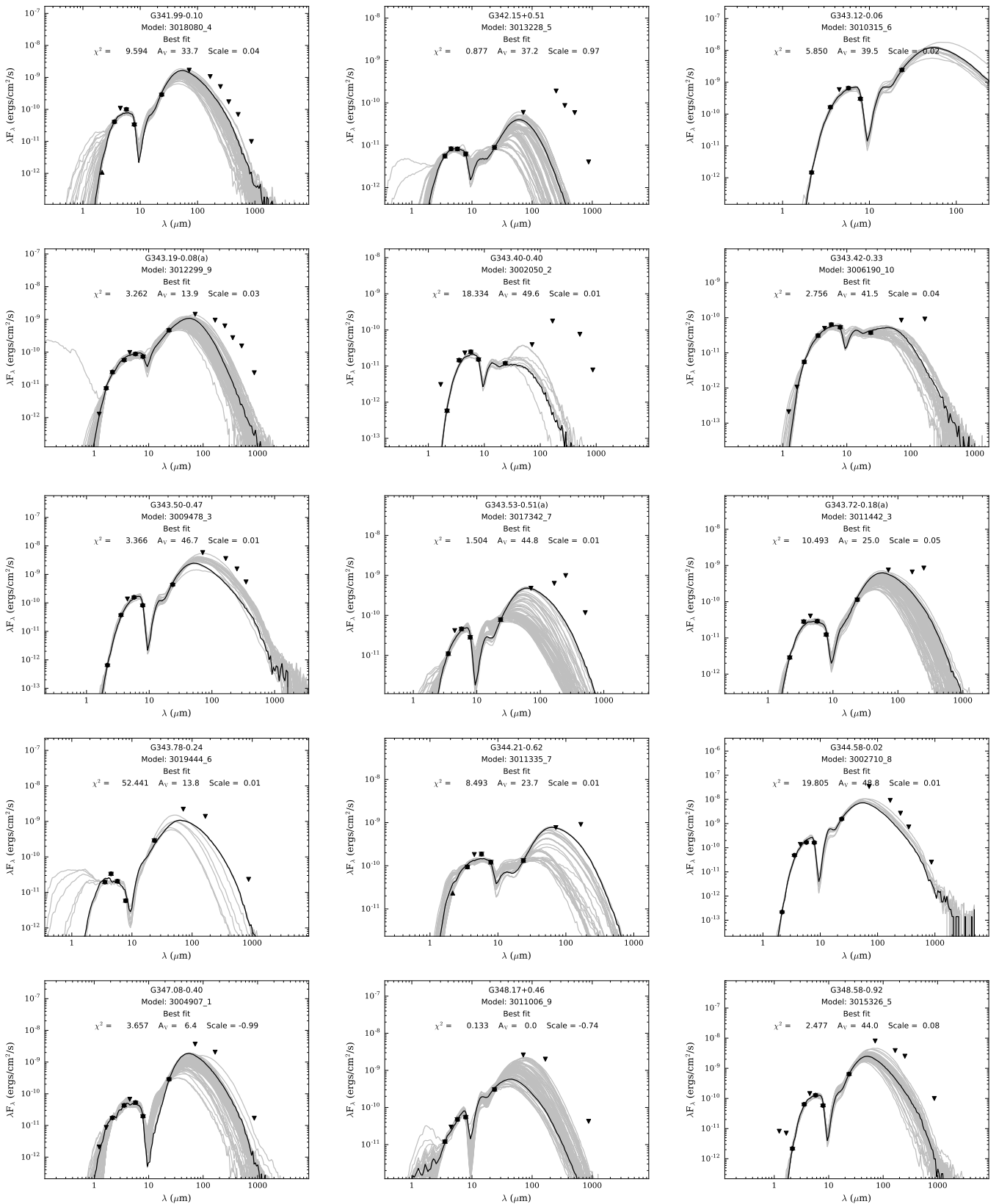


Fig. B.26: Continuation of Fig. B.22.

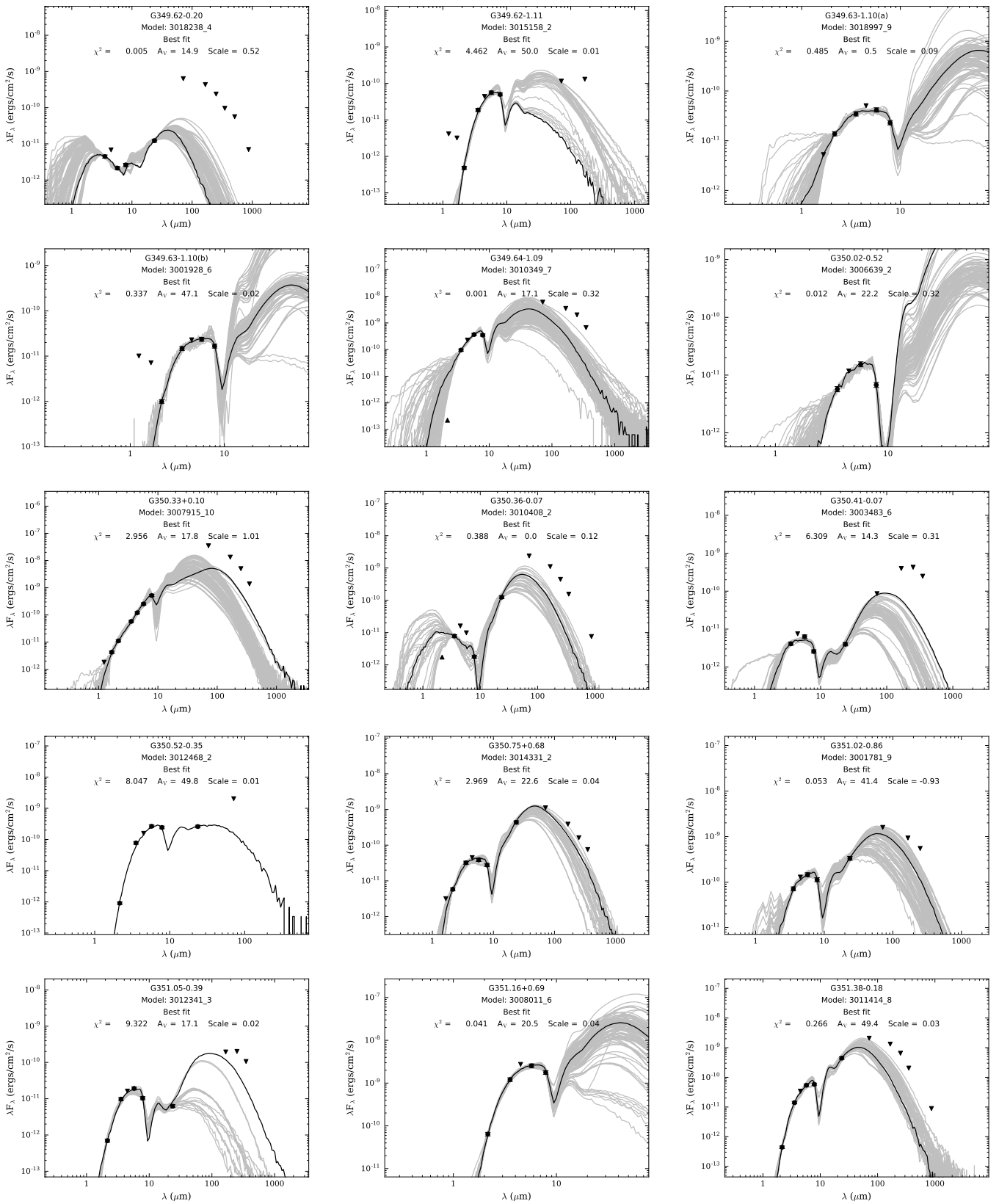


Fig. B.27: Continuation of Fig. B.22.

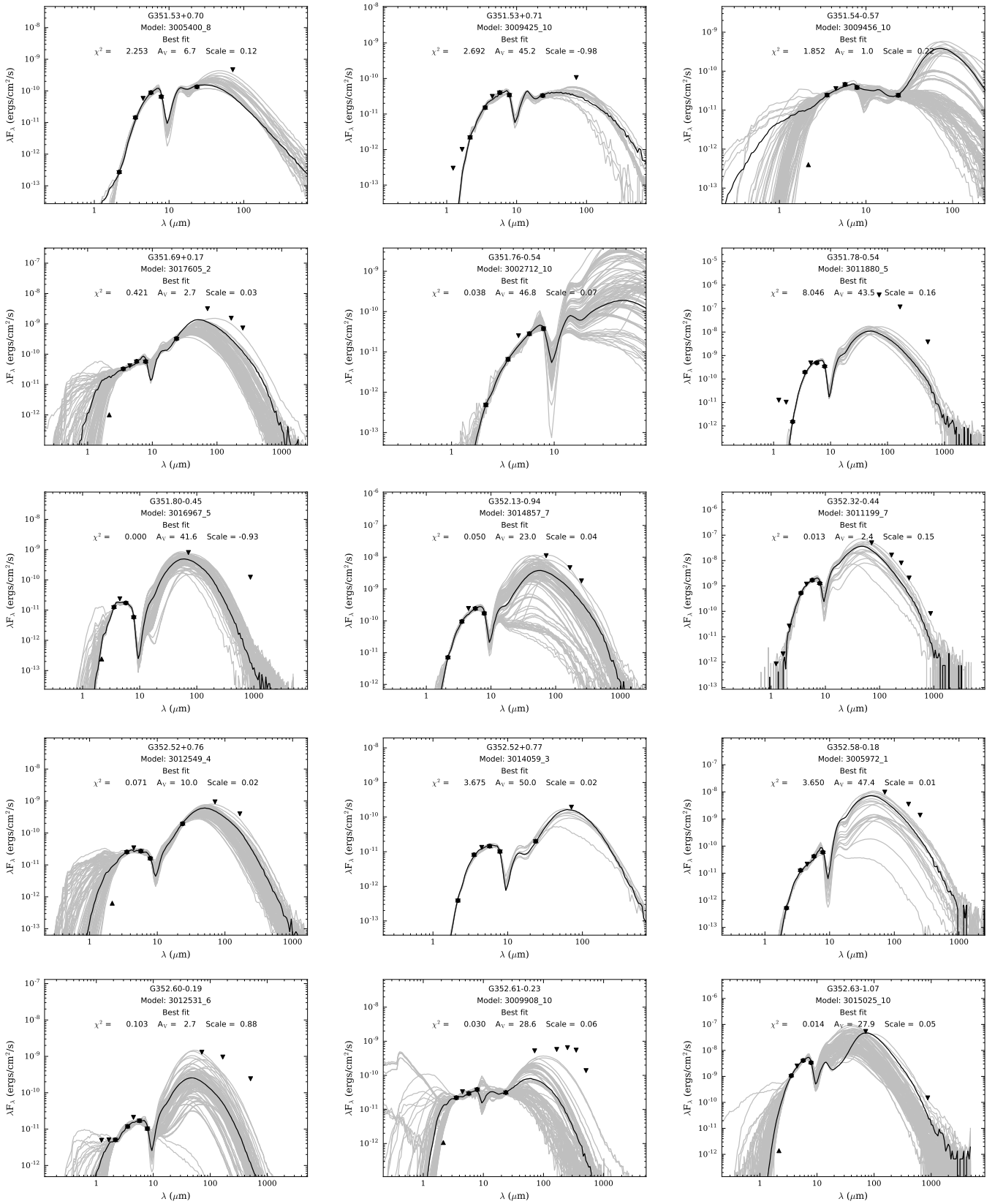


Fig. B.28: Continuation of Fig. B.22.

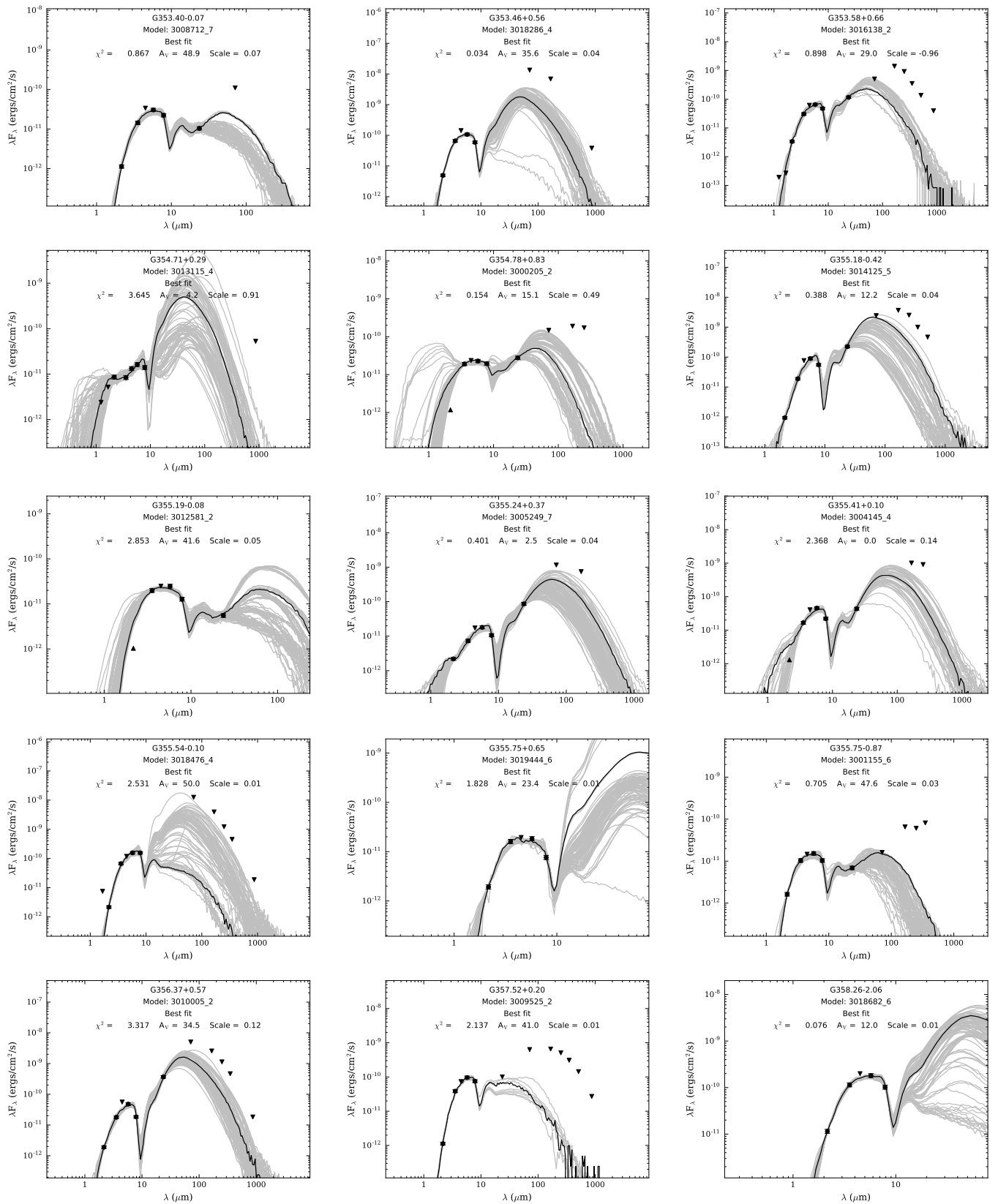


Fig. B.29: Continuation of Fig. B.22.

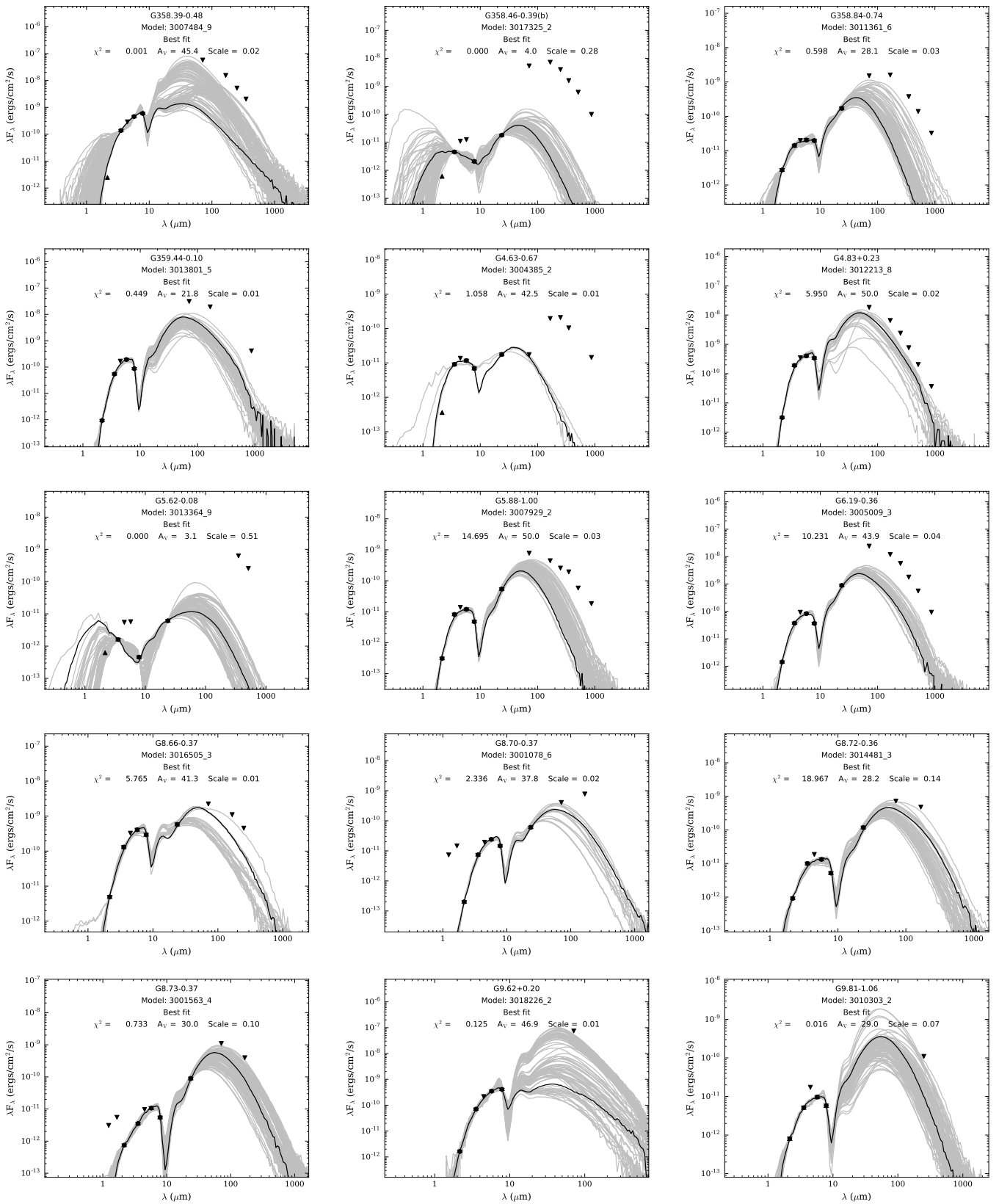


Fig. B.30: Continuation of Fig. B.22.

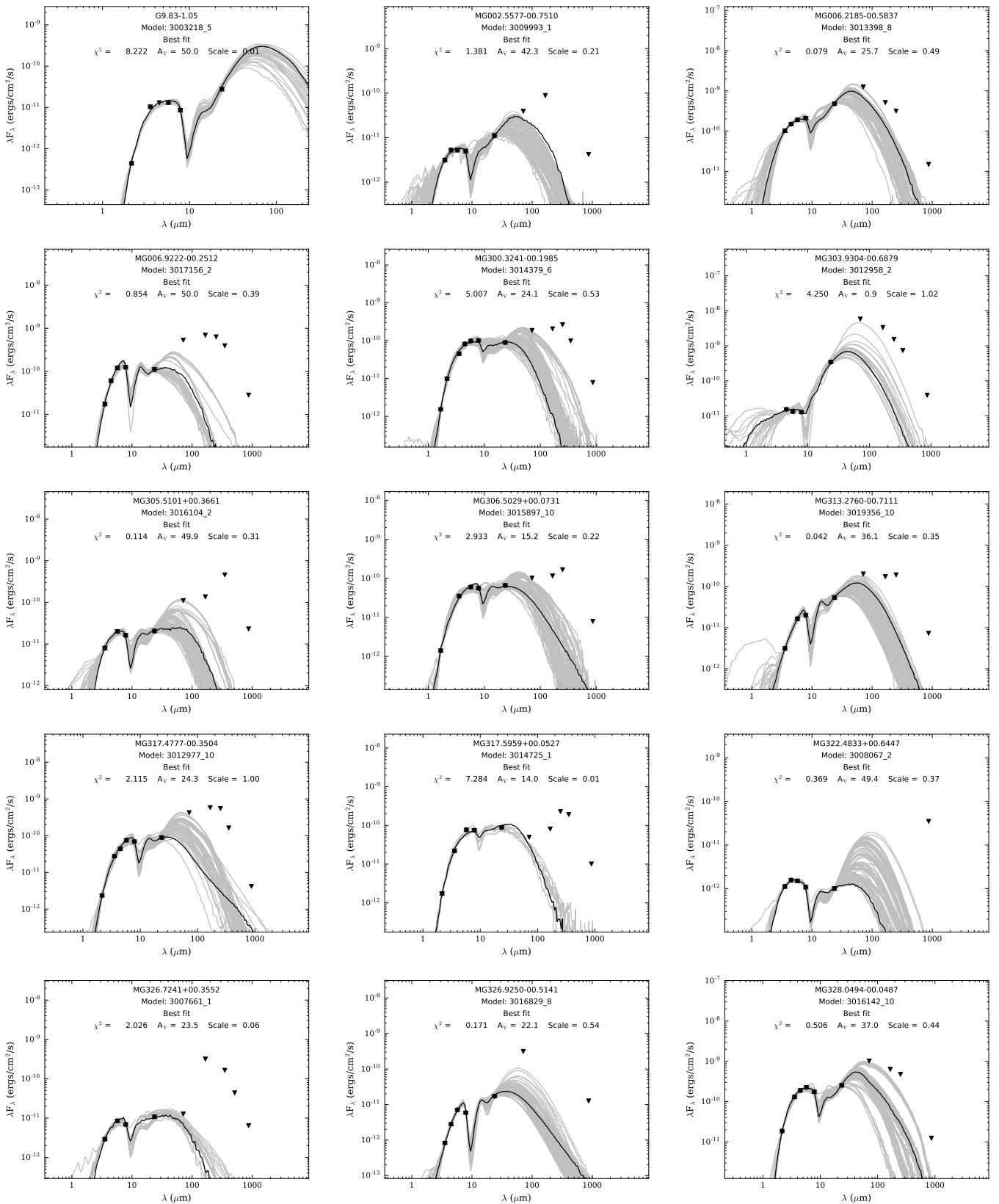


Fig. B.31: Continuation of Fig. B.22.

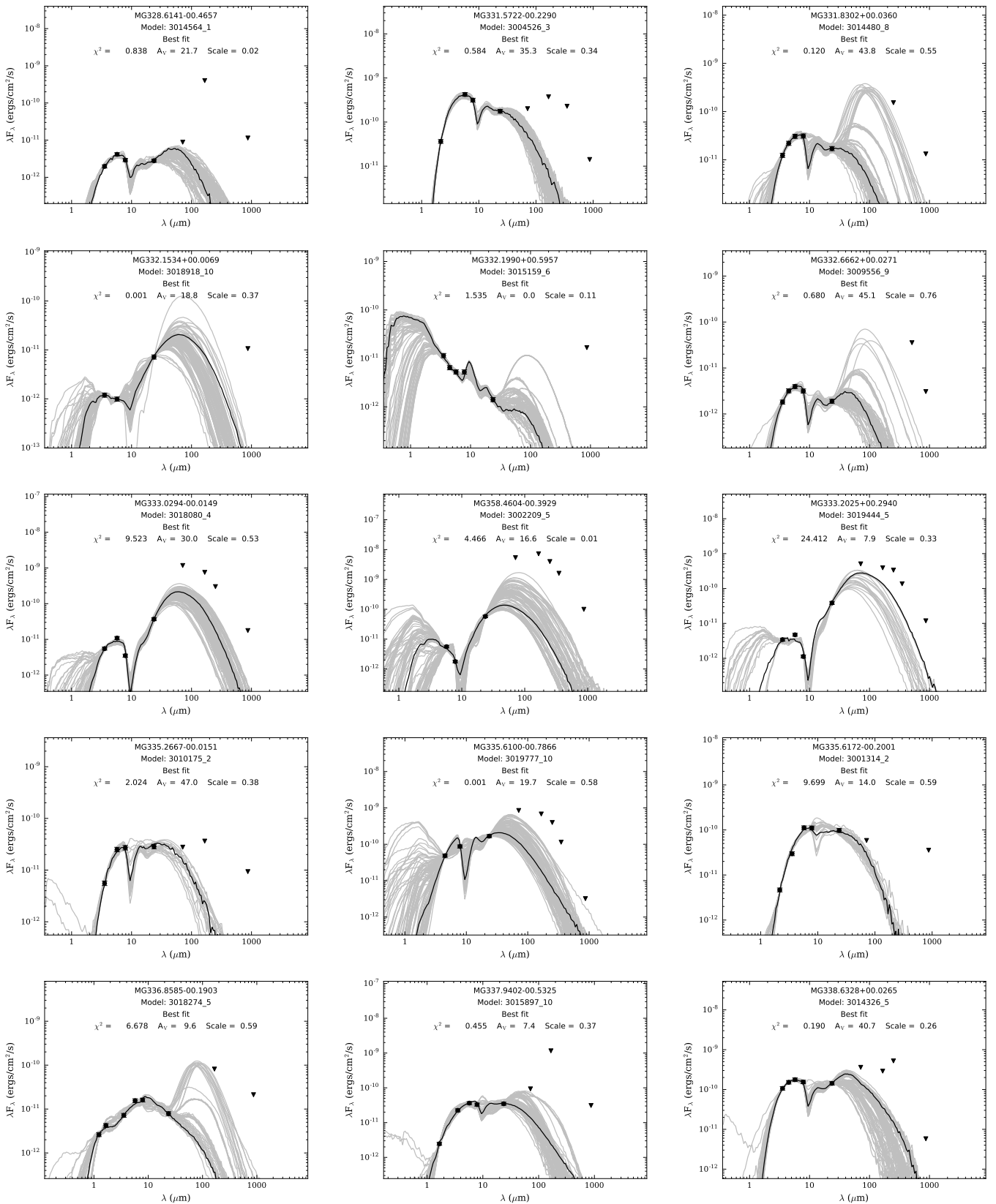


Fig. B.32: Continuation of Fig. B.22.

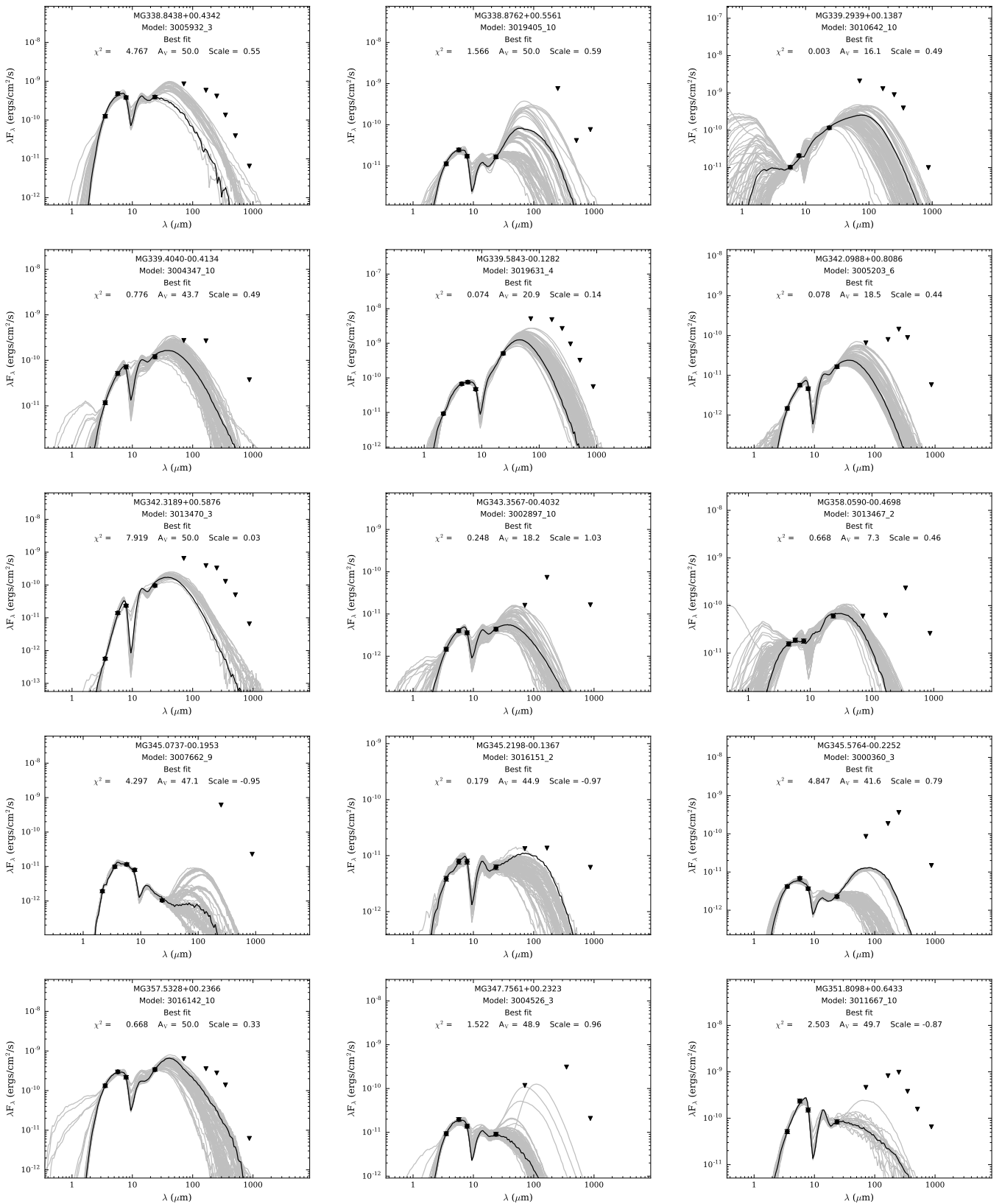


Fig. B.33: Continuation of Fig. B.22.

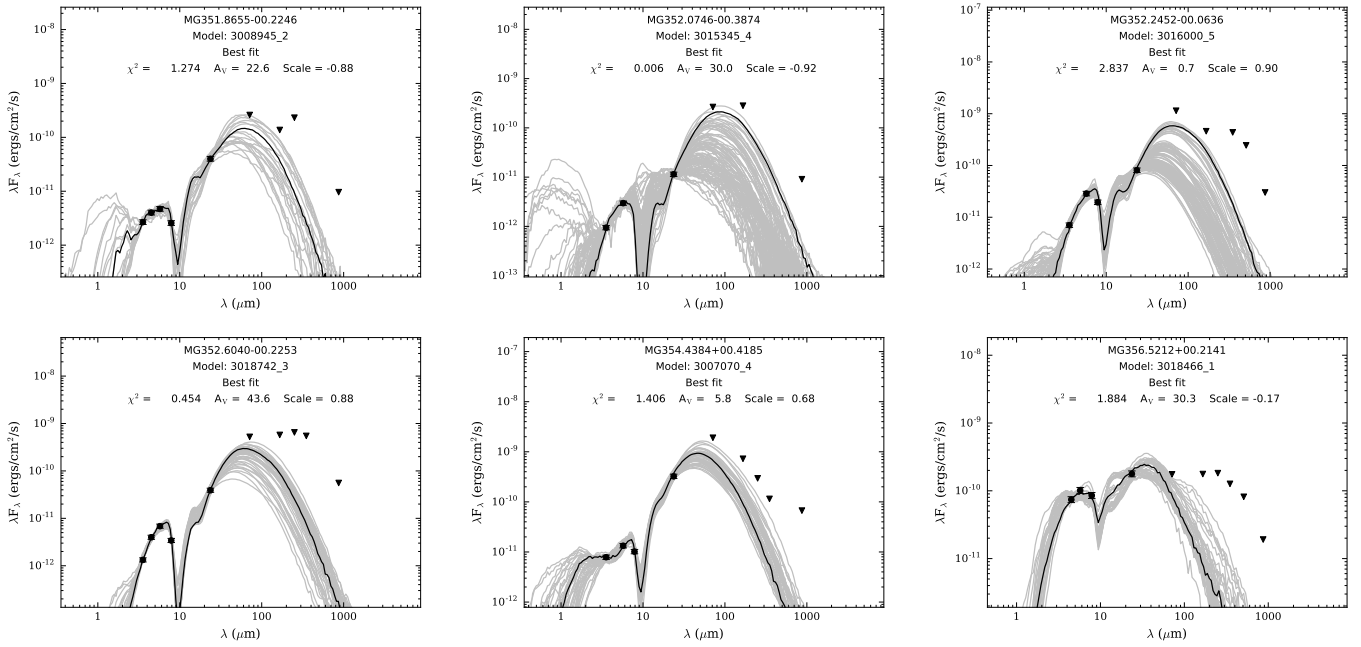


Fig. B.34: Continuation of Fig. B.22.